

Water and Heat Exchanges on the Tibetan Plateau

Observation and Modeling of the Yellow River Source Region

Donghai Zheng



WATER AND HEAT EXCHANGES ON THE TIBETAN PLATEAU

OBSERVATION AND MODELING OF THE YELLOW RIVER
SOURCE REGION

Donghai Zheng

Promotion committee:

Prof. Dr. Ir. A. Veldkamp	University of Twente
Prof. Dr. Ir. V.G. Jetten	University of Twente
Dr. M. Ek	NOAA Center for Weather and Climate Prediction
Prof. Dr. K. Yang	Institute of Tibetan Plateau Research

ISBN 978-90-365-3988-3

DOI: 10.3990/1.9789036539883

URL: <http://dx.doi.org/10.3990/1.9789036539883>

Copyright © 2015 by Donghai Zheng, University of Twente, Enschede, the Netherlands. All rights reserved.

No part of this book may be reproduced, stored in a retrieval system, or transmitted in any form or by any means, without the written permission of the author.

WATER AND HEAT EXCHANGES ON THE TIBETAN PLATEAU

**OBSERVATION AND MODELING OF THE YELLOW RIVER
SOURCE REGION**

DISSERTATION

to obtain
the degree of doctor at the University of Twente,
on the authority of the rector magnificus,
Prof. dr. H. Brinksma,
on account of the decision of the graduation committee,
to be publicly defended
on Thursday 26 November 2015 at 16:45 hrs

by

Donghai Zheng

born on 12 December 1986

in Fujian Province, China

This dissertation has been approved by

Prof. Dr. Ir. A.Y. Hoekstra (Supervisor)

Prof. Dr. Ir. Z. Su (Supervisor)

Dr. Ir. R. Van der Velde (Co-Supervisor)

Table of Contents

Acknowledgements	1
Summary	3
Samenvatting.....	7
Chapter 1 Introduction	11
1.1 Background.....	11
1.2 Land surface modeling	12
1.3 Water and heat exchanges on the Tibetan Plateau.....	14
1.4 Research objective and questions	15
1.5 Thesis outline.....	16
Chapter 2 Study area and in-situ data sets	19
2.1 Source region of the Yellow River	19
2.2 Maqu observational dataset	20
2.2.1 Hydro-meteorological variables.....	20
2.2.2 Soil properties	22
Chapter 3 Noah land surface model.....	25
3.1 Surface energy balance	26
3.1.1 Turbulent sensible and latent heat fluxes.....	26
3.1.2 Ground surface heat flux.....	28
3.1.3 Ground surface temperature.....	28
3.1.4 Soil heat flow	29
3.1.5 Soil thermal parameterization	29
3.1.6 Roughness length parameterization	30
3.2 Surface water budget	31
3.2.1 Soil water flow.....	32
3.2.2 Soil hydraulic parameterization	32
3.2.3 Root water uptake	33
3.2.4 Surface runoff and drainage.....	34
3.3 Freeze-thaw transitions.....	34
3.4 Model parameters	36

Chapter 4 Assessment of roughness length schemes37

4.1 Introduction37

4.2 Materials and methods.....39

 4.2.1 Parameterization of roughness lengths 39

 4.2.2 Estimation of roughness lengths 41

 4.2.3 Specific settings for the assessment..... 42

4.3 Characteristic of roughness lengths.....44

 4.3.1 Momentum roughness length..... 44

 4.3.2 Thermal roughness length or kB^{-1} 46

4.4 Calculation of sensible heat flux based on MOST48

 4.4.1 Assessment of thermal roughness length schemes 48

 4.4.2 Assessment of momentum roughness length schemes 50

4.5 Implementation of Noah LSM.....51

4.6 Discussion.....52

 4.6.1 Ground surface temperature uncertainty and its impact 52

 4.6.2 Energy-balance closure and its impact 54

 4.6.3 Choice of z_{oh} scheme..... 57

4.7 Conclusions58

Chapter 5 Augmentations to the turbulent and soil heat transport simulation61

5.1 Introduction61

5.2 Materials and methods.....63

 5.2.1 Vegetation effect on heat transport through soil..... 63

 5.2.2 C_{zil} parameterization..... 64

 5.2.3 Organic matter effect on soil thermal parameterization..... 65

5.3 Estimation of soil heat conductivity67

5.4 Noah simulations69

 5.4.1 Numerical experiments 69

 5.4.2 Turbulent heat fluxes and soil temperature profiles..... 71

 5.4.3 Assessment via Taylor diagram 74

5.5 Discussion.....77

 5.5.1 Improvement of nighttime surface temperature simulation 77

 5.5.2 Impact of soil moisture simulation 80

 5.5.3 Sensitivity analysis of organic matter parameterization 81

5.6 Conclusions82

Chapter 6 Augmentations to the soil water flow simulation.....85

6.1	Introduction	85
6.2	Materials and methods.....	87
6.2.1	Organic matter effect on soil hydraulic parameterization.....	87
6.2.2	Decrease of K_s with depth.....	89
6.2.3	Root distribution	90
6.2.4	Modified soil water flow scheme implementation.....	91
6.3	Estimation of soil hydraulic properties.....	92
6.3.1	Bulk density and porosity	92
6.3.2	Soil water retention curve	94
6.3.3	Saturated hydraulic conductivity	96
6.4	Simulation of soil moisture with the Noah LSM.....	97
6.4.1	Design of numerical experiments	97
6.4.2	Noah soil moisture simulations.....	99
6.5	Discussion.....	102
6.5.1	Impact on surface energy budget simulations.....	102
6.5.2	Impact on surface water budget simulations.....	105
6.6	Conclusions	106

Chapter 7 Impact of model physics on catchment scale runoff simulation 109

7.1	Introduction	109
7.2	Noah model physics	111
7.2.1	Noah-H.....	111
7.2.2	Noah-W.....	111
7.2.3	Noah-F	112
7.3	Measurements and model implementation	113
7.3.1	Atmospheric forcing	114
7.3.2	Vegetation and soil parameters.....	115
7.3.3	Experimental design	116
7.4	Point-scale assessment.....	117
7.5	Catchment-scale assessment.....	120
7.5.1	Areal average	120
7.5.2	Spatial variation	126
7.5.3	Sensitivity analysis	129
7.6	Summary and conclusions.....	131

Chapter 8 Conclusions and recommendations.....	135
8.1 Conclusions	135
8.2 Recommendations for future work	140
Appendix.....	143
A.1 Estimation of momentum roughness length	143
A.2 Stability functions.....	144
A.3 Soil pedotransfer functions.....	144
List of symbols.....	147
List of abbreviations	153
Bibliography	155

Acknowledgements

The long PhD journey is approaching to the end, which would, however, not be accomplished without the invaluable contributions from many people. To whom, I have now the opportunity to express my gratitude.

First and foremost, I owe my deep and sincere gratitude to my promoter and captain, Prof. Bob Su. I still remember how much effort you had tried to get me on board. I was stimulated with your discussion to tackle the water issue of our mother river as well as to carry out the PhD project on the roof of the world. Your scientific insight, wide knowledge and generous support provide the necessity for the safe landing of my PhD trip. You gave rooms to enable me to fly by myself, and you were always willing to share your rich experience and wisdom. Your modesty and enthusiasm in research set an excellent example for me in the future career.

I express my thanks to Prof. Arjen Hoekstra for offering me the opportunity to pursue the PhD adventure. Thanks for your patience, guidance and kind support. The chapter associated with the runoff simulation may not be completed without your encouragement.

I am deeply grateful to my supervisor and co-pilot, Dr. Rogier Van der Velde. You were involved in each chapter of this dissertation, and your critical reviews have stimulated me to clarify my own thinking and thus contributed to the final landing of my PhD trip. You spent lots of time helping me to figure out the research questions, to revise the manuscript, as well as to dig the hole on the Tibetan Plateau. You are always supportive and available for all kinds of discussions, and I really enjoy the coffee break time with you.

I'd like to express my sincere thanks to Dr. Martijn Booij as the co-supervisor for your continuous effort to help me to address the research questions and revise the manuscript. Thanks for your patience and kindness. I also owe you my apology for not including you in the promotion committee due to the stupid PhD regulation.

I especially thank Prof. Jun Wen and his group in Cold and Arid Regions Environmental and Engineering Research Institute, Chinese Academy of Sciences for their great efforts on assisting me to collect the essential in-situ data sets and guiding the successful of field campaign. I appreciate Prof. Jun Wen for his kindness and unconditional support, and I enjoy the friendship and working with Dr. Xin Wang and Mr. Zuoliang Wang in the field as well. I also

thank Dr. Rong Liu and Dr. Tangtang Zhang for their help to arrange the logistics for my stay in Lanzhou.

My keen appreciation goes to Prof. Kun Yang and his group in Institute of Tibetan Plateau Research, Chinese Academy of Science. From him I learned that publications mean nothing but conveying your opinions and contributions to research community. I'm also grateful to Dr. Yingying Chen to arrange the laboratorial investigation of soil properties. Further, many thanks should go to Prof. Yangwen Jia in China Institute of Water Resources and Hydropower Research and Dr. Mike Ek in Environmental Modeling Center of NCEP for their useful discussion on the modeling and computer codes.

I'd like to thank Mr. Wei Ouyang and Mrs. Xuelei Wang for recommending me to Prof. Bob Su. Thanks for their encouragement and confidence on my PhD work. I would also like to thank Prof. Shengtian Yang in Beijing Normal University for the acceptance and supervision of MSc study, which makes the PhD adventure possible. Moreover, I also owe my thanks to the Chinese Scholarship Council (CSC) for the financial support for my study in the Netherlands.

The PhD experience is of course the good fortune in my personal life and career. I was very lucky to work with so many great and genius colleagues in both groups of Prof. Bob Su and Prof. Arjen Hoekstra. Special thanks should go to all the secretaries, Anke, Tina and Joke for their kind support. Many thanks to Yijian and Liang Rong, Xuelong and Zhangbo, Shaoning, Zhuo La, Cesar and Myri, Chandra and Sujata, Tian Xin, Enrico, Suhyb, Binbin, Cunbo, Maoshan, Xiaolong, Yuan Xu, Huang Ying, Junping, Mireia, Leo, Alain, Laura, Mariela, Mustafa, Tanvir, Haris, Novi, Moiteela, Lichun, Wang Qiang, Peiqi, Wenlong, Maarten, Mesfin and Harm-Jan. I also pay high regards to all other Chinese friends I got familiar in the past five years, thanks for your friendship and support. My PhD life would never be that colorful without the Critters and Chinese Old Boys, I really enjoyed each match I played with all of you.

My heartiest and foremost gratitude must be paid to my parents for their endless support and love. I would also like to thank my parents-in-law to bring my angel to this world. Xiaojing Wu, my sweetheart, I would never accomplish anything without your encouragement and loving support.

Donghai Zheng
Enschede, 6 November 2015

Summary

Climate change is projected to reduce fresh water resources significantly, and this is also the case for Asian water towers that originate from the Tibetan Plateau. At the same time, the Tibetan ecosystem is subject to striking warming and moistening accompanied with permafrost degradation and glacier retreat, exerting further profound impacts on the regional hydrologic cycle and freshwater supply. Understanding the water and heat exchanges across the Tibetan ecosystem is, therefore, of great importance to account for various feedbacks on the regional water cycle within various climate scenarios.

This thesis contributes to a better quantification of the water and heat exchanges at the land-atmosphere interface for a Tibetan alpine meadow ecosystem. The source region of the Yellow River (SRYR) in the northeastern part of the Tibetan Plateau is selected as the case study, because of its great importance to the Yellow River's water resources that supports about 14.9 % of China's population and 17 % of its agricultural area. A comprehensive dataset that includes in-situ micro-meteorological and profile soil moisture/temperature measurements, laboratory soil property measurements of samples, as well as discharge measurements is developed for the selected study domain (see Chapter 2). To understand the processes governing the water and heat exchanges of the alpine meadow ecosystem and predict the measurements, the Noah land surface model (LSM) is utilized as the baseline model (see Chapter 3), because it is widely used by the climate and land surface modeling communities to quantify the exchange of water and heat at the land-atmosphere interface. The main research objective is achieved as presented in four research chapters.

Firstly, Chapter 4 focuses on the assessment of various roughness length schemes recently developed for the Noah LSM on their applicability for the Tibetan circumstances. Monthly variations of momentum roughness length (z_{0m}) and diurnal variations of thermal roughness length (z_{0h}) are derived through application of the Monin-Obukhov similarity theory based on in-situ turbulent heat fluxes and profile measurements of wind and air temperature. These derived z_{0m} and z_{0h} values together with the measured heat fluxes are utilized to assess the performance of various z_{0m} and z_{0h} schemes for three selected periods: a winter (15 December 2009 to 15 January 2010), a spring (8 April to 7 May 2010) and a monsoon period (1 to 30 September 2009). Current z_{0m} schemes can satisfactorily reproduce the observed z_{0m} dynamics that are related to vegetation

dynamics and soil water freeze-thaw state. The heat flux simulations are found to be very sensitive to the diurnal variations of z_{0h} , and all the newly developed z_{0h} schemes capture the observed diurnal variability much better than the original one over the sparsely vegetated surfaces during the winter (frozen) period. It is, however, noted that not all newly developed schemes perform consistently better than the original one over the densely vegetated surfaces during the spring (thawed) and monsoon periods. The z_{0h} scheme defining Zilitinkevich's empirical coefficient (C_{zil}) as function of canopy height via z_{0m} is finally recommended for global application due to its suitability for a wide range of land cover and climate regimes.

Secondly (Chapter 5), the Noah model physics associated with the description of turbulent heat fluxes and heat transport through the soil column is investigated through comparisons against turbulent heat fluxes and soil temperature profile measurements taken during the monsoon season (8 June to 30 September 2010). Noah with its default model physics constrained by soil moisture profile measurements significantly overestimates the daytime turbulent heat fluxes, underestimates the surface temperature, and systematically underestimates the soil temperature profiles. Four augmentations are studied for mitigating above deficiencies via i) the removal of the vegetation muting on the heat conductivity (κ_h) for soil heat transport from the first layer towards the second layer, ii) the calculation of the exponential decay factor (β_{veg}) imposed on κ_h using the ratio of the leaf area index (*LAI*) over the green vegetation fraction (*GVF*), iii) the computation of the Zilitinkevich's empirical coefficient (C_{zil}) for the turbulent heat transport as function of the momentum roughness length (z_{0m}) as recommended in Chapter 4, and iv) the consideration of the impact of organic matter in the parameterization of the thermal heat properties. The removal of the muting effect of vegetation on κ_h and the parameterization of β_{veg} greatly enhance the soil temperature profile simulations, whereas turbulent heat flux and surface temperature computations mostly benefit from the modified C_{zil} formulation. Although usage of organic matter for calculating κ_h improves the correspondence between the estimates and laboratory measurements of heat conductivities, it is shown to have a relatively small impact on the Noah LSM performance even for large organic matter contents. Further, the nighttime surface temperature overestimation is resolved from a coupled land-atmosphere perspective.

The third research chapter (Chapter 6) deals with Noah model physics associated with the description of soil water flow through comparison with laboratory measurements of the soil water retention curve and in-situ saturated

hydraulic conductivity (K_s) and soil moisture profile measurements during the monsoon season. The default Noah LSM underestimates the soil moisture content of the top layer under wet conditions and overestimates it during dry-down episodes, whereas the moisture contents in the deeper soil layers are systematically underestimated. Four augmentations are investigated to remediate above deficiencies by i) including the effect of organic matter on soil hydraulic parameterization via the additivity hypothesis, ii) implementing the K_s as an exponentially decaying function with soil depth, iii) modifying the vertical root distribution to represent the Tibetan alpine grassland conditions characterized by an abundance of roots in the topsoil and iv) modifying the diffusivity form of Richards' equation to allow for the simulation of soil water flow across soil layers with different hydraulic properties. Usage of organic matter for calculating the porosity and soil suction improves the agreement between the estimates and laboratory measurements, and the exponential function together with the Kozeny-Carman equation best describes the in situ K_s . Through implementation of the modified hydraulic parameterization alone, the soil moisture underestimation in the upper soil layer under wet conditions is resolved, while the soil moisture profile dynamics are better captured when also the modified root water uptake function (i.e., asymptotic vertical root distribution) is included.

Noah model physics' options evaluated in Chapters 4, 5 and 6 are implemented in Chapter 7 to further investigate their ability in reproducing runoff at catchment scale, i.e., the SRYR for the period of 2001-2010. Three sets of augmentations are implemented affecting the model physics associated with the i) turbulent and soil heat transport (Noah-H), ii) soil water flow (Noah-W) and iii) frozen ground processes (Noah-F). Five numerical experiments are designed with the three augmented versions, a control run with default model physics and a run with all augmentations (Noah-A). Each experiment adopts vegetation and soil parameters from the Weather Research and Forecasting dataset, is driven by 0.1° atmospheric forcing data from ITPCAS (Institute of Tibetan Plateau Research, Chinese Academy of Sciences) and is initialized using a single-year recurrent spin-up to achieve the equilibrium model states. In addition, soil organic matter content from the China Soil Database is utilized for the updated soil thermal and hydraulic schemes. In-situ heat flux, soil temperature (T_s) and moisture (θ) profile measurements are available for point-scale assessment, whereas monthly streamflow is utilized for the catchment-scale evaluation. The augmentations invoked with Noah-H resolve issues with the heat flux and T_s simulation (as presented in Chapter 5) and Noah-W

mitigates deficiencies in the θ simulation (as presented in Chapter 6), while Noah-A yields improvements for both simulated surface energy and water budgets. Also at the catchment scale the best model performance is found for Noah-A with the combination of the augmentations leading to a baseflow dominated runoff regime, whereby the surface runoff contribution remains significant.

The research presented in this thesis highlights the need for a complete description of the predominantly vertical water and heat exchange processes to correctly simulate the water and heat fluxes in the seasonally frozen and high altitude SRYR on the Tibetan Plateau. Additional research is still needed to address other processes such as freeze-thaw transitions, groundwater dynamics and river routing. Improved simulation of water and heat fluxes is of paramount importance to project the impact of climate variability on the regional water cycle and to support management of the water resources in the Asian water towers.

Samenvatting

Het is de verwachting dat als gevolg van klimaatverandering de zoetwatervoorraden wereldwijd drastisch zullen verminderen en dit geldt ook voor het Tibetaans Plateau dat bekend staat als de Aziatische Watertorens. Recent onderzoek heeft namelijk aangetoond dat het Tibetaanse ecosysteem blootgesteld staat aan een opvallend sterke opwarming die gepaard gaat met een vernatting van het landoppervlak, permafrostdegradatie en het krimpen van gletsjers. Deze veranderingen in de regionale hydrologie hebben ingrijpende gevolgen voor de zoetwatervoorziening in de stroomgebieden van de grote Aziatische rivieren, zoals de Gele Rivier, Jangtse, Mekong, Ganges, Brahmapoetra en Indus. Het verkrijgen van een beter inzicht in de uitwisseling van water en warmte aan het landoppervlak van het Tibetaanse Plateau is daarom van groot belang om betrouwbare voorspellingen te kunnen maken over de gevolgen van de opwarming van de aarde voor de Aziatische Watertorens.

Dit proefschrift draagt bij aan een verbeterd begrip van de processen die ten grondslag liggen aan de water- en warmte-uitwisseling tussen het landoppervlak en de atmosfeer over de Tibetaanse alpenweiden. Voor dit onderzoek is het Brongebied van de Gele Rivier (BGR) in het noordoostelijke deel van het Tibetaans Plateau geselecteerd, omdat 35 % van de afvoer van de Gele Rivier in dit gebied gegenereerd wordt. Er is een uitgebreide dataset voor het gekozen studiegebied verzameld, bestaande uit afvoermetingen van de Gele Rivier, in situ micro-meteorologische en bodemvocht- en temperatuurprofielmetingen en metingen van bodemeigenschappen verricht in het laboratorium (zie hoofdstuk 2). Om de gemeten water- en warmte-uitwisselingsprocessen in het alpenweide ecosysteem beter te begrijpen is het Noah Land Oppervlakte model (LOM) gebruikt (zie hoofdstuk 3). Het Noah LOM wordt in de Verenigde Staten gebruikt door het NCEP (National Centers for Environmental Prediction) als de landcomponent van klimaat- en weersvoorspelmodellen. De doelstelling wordt bereikt zoals gepresenteerd in vier hoofdstukken.

Hoofdstuk 4 richt zich op het testen van diverse recent ontwikkelde methoden voor het bepalen van de ruwheidslengte voor momentum- en warmte transport op hun toepasbaarheid voor de Tibetaanse omstandigheden. Maandelijks variaties van momentum ruwheidslengte (z_{0m}) en de dagelijkse variaties van thermische ruwheidslengte (z_{0h}) zijn afgeleid door toepassing van de Monin-Obukhov similarity theory op basis van in situ turbulente warmtefluxen en wind- en luchttemperatuurprofiel metingen. Zowel de z_{0m} en

z_{0h} waarden bepaald op basis van metingen als de gemeten warmtefluxen zijn gebruikt om de geschiktheid van de ruwheidslengte methoden voor de Tibetaanse omstandigheden te evalueren voordrie geselecteerde periodes: een winter- (15 december 2009 tot 15 januari 2010), een lente- (8 april tot 7 mei 2010) en een moessonperiode (1 tot 30 september 2009). De huidige z_{0m} waarden reproduceren de waargenomen dynamiek gerelateerd aan vegetatiegroei bevriezen/dooien van bodemwater naar tevredenheid. De warmteflux simulaties blijken echter zeer gevoelig voor de dagelijkse z_{0h} variaties te zijn, en alle nieuw ontwikkelde z_{0h} methoden reproduceren de waargenomen dagelijkse variabiliteit veel beter dan de originele methode. Er dient echter opgemerkt te worden dat niet alle nieuw ontwikkelde methoden consistent beter presteren dan de oorspronkelijke methoden over de dicht begroeide oppervlakken tijdens de lente- (ontdooide) en moessonperiodes. De z_{0h} methoden die de Zilitinkevichcoëfficiënt (C_{zil}) definiëren als functie van de gewashoogte via z_{0m} zijn hetmeestgeschikt bevonden voor wereldwijde toepassing.

In Hoofdstuk 5 wordt de Noah modelfysica aangaande de turbulente warmtefluxen en het warmtetransport door de bodemkolom bestudeerd door het analyseren van de turbulente warmtefluxen en bodemtemperatuur profielmetingen tijdens hetmoessonseizoen (8 juni - 30 september 2010). Noah met zijn standaard modelfysica overschat turbulente warmtefluxen overdag aanzienlijk, onderschat de oppervlaktetemperatuur en systematisch onderschat de bodemtemperatuur profielen. Er zijn vier aanpassingen bestudeerd om de bovengenoemde tekortkomingen te verhelpen; ten eerste is de demping als gevolg van vegetatie van de warmtegeleidbaarheid (κ_h) van de eerste naar de tweede bodemlaag verwijderd; ten tweede is een exponentiële vervalfactor (β_{veg}) opgelegd aan κ_h op basis van de ratio 'Leaf Area Index' (LAI) ten opzichte van de 'Green Vegetation Fraction' (GVF); ten derde is de methode voor de berekening van de Zilitinkevichcoëfficiënt (C_{zil}) geïmplementeerd zoals aanbevolen in Hoofdstuk 4, en ten vierde is het effect van organische stof ingebouwd in de methode gebruikt voor de bepaling van thermische grondeigenschappen. De verwijdering van het dempende effect van vegetatie op κ_h en het introduceren van β_{veg} resulteren in een sterke verbetering van de temperatuursimulaties in het bodemprofiel, terwijl de simulaties van de turbulente warmteflux en oppervlaktetemperatuur vooral profiteren van de gewijzigde C_{zil} formulering. Hoewel het gebruik van organisch materiaal de berekening van κ_h verbetert, is op basis van laboratoriummetingen aangetoond

dat de impact op de Noah simulaties relatief klein is, zelfs als het organisch stofgehalte groot is.

Hoofdstuk 6 focust zich ophetverbeteren van de Noah modelfysica diede verticale stroming van water door de bodem beschrijft door een vergelijking met in situ gemeten bodemvochtprofielen en het gebruik van gemeten bodemfysische eigenschappen. De standaard Noah LOM onderschat het bodemvochtgehalte van de bovenste laag onder natte omstandigheden en overschat het indroge condities, terwijl het vochtgehalte in de diepere bodemlagen systematisch wordt onderschat. Er zijn vier aanpassingenonderzocht om bovengenoemde tekortkomingen te verhelpen namelijk door i) het effect van organische stof op vochtretentie in de bodem in beschouwing te nemen via de additiviteitshypothese, ii) de verzadigde doorlatendheid (K_s) te implementeren als een exponentieel afnemende functie met bodemdpte, iii) het aanpassen van de verticale wortelverdeling om de hoge worteldichtheid nabij het landoppervlak beter te kunnen reproduceren die karakteristiek is voor de Tibetaanse weiden, iv) het wijzigen van de diffusiviteitsvorm van de Richards-vergelijking om een betrouwbare simulatie van vochttransport tussen lagen met verschillende bodemfysische eigenschappen mogelijk te maken. Het gebruik van organisch materiaal voor de bepaling van de porositeit en de bodemretentievergrootde overeenkomsten tussen de schattingen en meting die in situ en in het laboratorium verricht zijn. Door de gewijzigde bodemfysische parameterisatie wordt de onderschatting van het bodemvocht in de bovenste bodemlaag onder natte omstandigheden grotendeels verholpen. De simulatie van de vochtdynamiek in het bodemprofiel verbetert wanneer ook de gewijzigde wortelopnamefunctie is geïmplementeerd in de modelstructuur.

De componenten van de Noah modelfysica die geëvalueerd zijn in Hoofdstukken 4, 5 en 6 worden in Hoofdstuk 7 toegepast op de schaal van het BGR om de afvoer voor de periode 2001-2010 te reproduceren. Er zijn simulaties uitgevoerd met drie sets van verbeteringen ten aanzien van de modelfysica op het gebied van i) turbulente en bodemwarmtetransport (Noah-H), ii) bodemvocht transport (Noah-W) en iii) processen in bevroren bodems (Noah-F). Er zijn vijf numerieke experimenten ontworpen bestaande uit drie runs met verbeteringen, een controle-run met de standaard modelfysica en een run met alle aanpassingen (Noah-A). Voor elk experiment zijn de vegetatie- en bodemparameters van de Weather Research and Forecasting dataset gebruikt en er wordt gebruik gemaakt van atmosferische gegevens met een ruimtelijke resolutie van 0.1° ontwikkeld door ITPCAS (Instituut for Tibetan Plateau

Research of the Chinese Academy of Sciences). Iedere simulatie is geïnitieerd door Noah een volledig jaar herhaaldelijk te draaien totdat de modeltoestandvariabelen een evenwichtssituatie bereiken. De resulterende simulaties zijn vergeleken met warmteflux-, bodemtemperatuur- (T_s) en vocht (θ) profielmetingen verricht op een specifieke locatie. Daarnaast is de maandelijkse gemeten afvoer van de Gele Rivier gebruikt om de betrouwbaarheid van de Noah modelsimulaties op de schaal van het stroomgebied te bepalen. De Noah-Haanpassingen verhelpen de problemen met de simulatie van turbulente en bodemwarmte transport (Hoofdstuk 5) en de Noah-W aanpassingen verhelpen de tekortkomingen in de θ simulatie (Hoofdstuk 6), terwijl de Noah-A implementatie verbeteringen oplevert voor zowel de gesimuleerde energiebudgetten als waterbudgetten. Ook de maandelijkse afvoer wordt het best gereproduceerd door het Noah-A experiment, waarbij de afvoer gedomineerd wordt door de basisafvoer component maar ook de oppervlakte-afvoer niet te verwaarlozen is.

Het onderzoek dat in dit proefschrift gepresenteerd is benadrukt de noodzaak van een volledige beschrijving van de voornamelijk verticale water en warmte uitwisselingsprocessen om betrouwbare simulaties van de water- en energiebalans te kunnen produceren voor het BGR hooggelegen op het Tibetaans Plateau. Aanvullend onderzoek is echter nodig om andere processen, zoals vries-dooi transities, grondwateruitwisselingen en rivierafvoer adequaat mee te kunnen nemen in klimaatprojecties van de regionale hydrologie. Een verbeterde simulatie van water- en energiebalansen is van het grootste belang om de impact van de opwarming van de aarde op de regionale watercyclus in te kunnen schatten en dit kan het beheer van de watervoorraden in de Aziatische Watertorens verder ondersteunen.

Chapter 1 Introduction

1.1 Background

Climate change is projected to reduce fresh water resources significantly and water scarcity is expected to be a major challenge globally (Jiménez et al. 2014). The Asian water towers, originating from the Himalayas and adjacent Tibetan Plateau, are threatened by a projected decline in the water availability as a result of climate change (Immerzeel et al. 2010). At the same time, various studies have warned for the climate vulnerability of the Tibetan ecosystem via striking warming and moistening (Salama et al. 2012; van der Velde et al. 2014; Wu et al. 2013), solar dimming and wind stilling (Yang et al. 2014) accompanied with permafrost degradation (Guo and Wang 2013; Wu and Zhang 2010) and glacier retreat (Yao et al. 2012), which inevitably exert a profound impact on the regional hydrologic cycle and freshwater supply (Jin et al. 2009; Lutz et al. 2014; Wang et al. 2012).

The dependence of several billions of people on the freshwater supply from the Great Asian Rivers, e.g., Ganges, Brahmaputra, Mekong, Yangtze, and Yellow River, underlines the importance of preserving the high altitude Asian ecosystem on the Tibetan Plateau. Moreover, the Plateau plays a critical role in the onset, intensity, and evolution of the East-Asian Monsoon (Wu et al. 2012). Exchange of water and heat at the Tibetan land-atmosphere interface modulates the atmospheric circulation in the Northern Hemisphere at a continental scale (Zhou et al. 2009). Understanding the water and heat exchanges across the Tibetan ecosystem is, therefore, of great importance to account for the various feedbacks on the regional water and energy budgets within various climate scenarios.

Located in the northeastern part of the Tibetan Plateau, the source region of the Yellow River (SRYR) has also been subject to a significant warming and widespread decrease of precipitation in the wet season, resulting in a pronounced decrease of water resources in this region (Hu et al. 2012; Hu et al. 2011). As the “water tower” that contributes to more than 35 % of the total streamflow for the whole Yellow River basin (Zhou and Huang 2012), the decreasing water resources in the SRYR inevitably influences water supply for the downstream areas. Since about 14.9 % of China’s population and 17 % of its agricultural area depend on the water supply from the Yellow River (D. Yang et al. 2004), a thorough understanding of water and heat dynamics across

the SRYR is thus imperative for management of the Yellow River's water resources and projection of its water availability.

1.2 Land surface modeling

Land surface models (LSMs) are often employed in atmospheric general circulation models (AGCMs) to provide the lower boundary conditions in the form of water and heat exchanges at the land-atmosphere interface. Climatic studies (Koster et al. 2004; Seneviratne et al. 2006) have demonstrated that an accurate quantification of these exchanges is crucial for reliable weather forecasts across various time scales. In order to make reliable weather and climate predictions, LSMs have evolved from a simple bucket model (Manabe 1969) to more sophisticated soil-vegetation-atmosphere transfer (SVAT) schemes to better represent the interplay of the water, energy and nutrient cycles (Dai et al. 2003; Ek et al. 2003; Niu et al. 2011; Oleson et al. 2013; Sellers et al. 1986).

Many of the physical and physiological processes occurring in the atmosphere-snow-vegetation-soil-aquifer system are incorporated in the contemporary LSM structures. For instance, model physics for the freeze-thaw and snow processes are now generally included in LSMs (Cherkauer and Lettenmaier 1999; Dankers et al. 2011; Ek et al. 2003; Niu and Yang 2006) and snow sub-models have evolved from simple bulk-layer to multilayer structures (Niu et al. 2011). Vegetation dynamics have been introduced in several LSMs to explicitly represent plant photosynthesis, respiration, and the related nutrient cycles (Clark et al. 2011; Oleson et al. 2013). Studies have also focused on describing the fully-closed water cycle consisting of soil-aquifer interaction (Fan et al. 2007; Maxwell and Miller 2005), alternative runoff schemes (Niu et al. 2011; Oleson et al. 2013), river rooting (Balsamo et al. 2011) as well as anthropologic effects such as irrigation (Leng et al. 2013). Consequently, there are increasing interests in using LSMs for hydrologic modeling purposes (Finney et al. 2012; Slater et al. 2007). Wood et al. (2011) proposed the development of hyper-resolution LSMs (1 km globally, 100 m continentally) for monitoring the terrestrial water, energy, and biogeochemical cycles as the "Grand Challenge" for the hydrological and land surface modeling community. In response, Beven and Cloke (2012) argued that better model predictions are not only achieved by adopting a higher spatial resolution due to remaining issues such as the lack of fundamental knowledge on model forcing and parameter values, boundary conditions and representation of processes.

As any model, the reliability of LSM simulations is always affected by uncertainties in applied parameterizations, initial and boundary conditions and atmospheric forcing. Moreover, any parameterization of a complex process is an approximation that is always constrained by our incomplete understanding of the reality that is hampered by limited data (Niu et al. 2011). In addition, many parameterizations exist for a particular process, and the appropriateness of a parameterization may depend on the type of ecosystem (Li et al. 2011). For instance, various vertical root distribution functions (Chen et al. 1996; Vrugt et al. 2001; Zeng 2001) are employed by LSMs to simulate the root water uptake and the extraction of soil water for transpiration from specific layers (Feddes et al. 1978). Diversity is also found among the parameterizations used to describe the soil hydraulic properties by means of different functions using various parameter databases (Decharme et al. 2011; Shao and Irannejad 1999). In many cases, no clear reason exists for preferring one parameterization over the other (Gayler et al. 2014), and the selection of a parameterization in the LSMs is often based on its numerical efficiency (de Rosnay et al. 2000; Ek et al. 2003).

Dirmeyer et al. (2006), Jiménez et al. (2011) and Xia et al. (2014) have also reported that large discrepancies exist between the model outputs of water and heat fluxes generated by various LSMs even when driven with the same meteorological forcing, due to different model physics, model structures and parameter choices. In general, thorough evaluation against a ‘ground truth’ can identify the impact of these different sources of uncertainty and do justice to the physical reality. A comprehensive set of in-situ measurements of water and heat fluxes as well as atmospheric forcing is thus regarded as the foundation for assessing and improving the LSM performances. In addition, runoff data can provide further insight into the model performance for regional scale applications (Balsamo et al. 2011; Decharme 2007; Xia et al. 2012b). As such, the major challenge for the hydrologic and land surface modeling community remains to find ways to further reduce predictive uncertainties and strive for consistency between model results and observational data sets (Decker et al. 2011; Dirmeyer et al. 2006; Jiménez et al. 2011; Xia et al. 2012a).

The community Noah LSM has gone through a similar evolution via a long history of multi-institutional collaboration (e.g., Chen et al. 1996; Ek et al. 2003; Koren et al. 1999; Livneh et al. 2010; Mahrt and Ek 1984). It has undergone extensive testing and has been proven to reproduce the observed water and energy budgets effectively and comparably as other contemporary LSMs such as Community Land Model (CLM; Oleson et al. 2013), Variable Infiltration Capacity (VIC; Cherkauer et al. 2003) and Hydrology of the Tiled ECMWF

Scheme for Surface Exchanges over Land (HTESSEL; Balsamo et al. 2009) through participating in various LSM comparison experiments (e.g., Dirmeyer et al. 2006; Koster et al. 2010; Luo et al. 2003; Rodell et al. 2004; Xia et al. 2012c). The Noah LSM has been coupled to the AGCMs of National Centers for Environmental Prediction (NCEP) as well as the Weather Research and Forecasting (WRF) model of National Center for Atmospheric Research (NCAR) and is widely used. It is also the LSM for which NASA makes the most extensive set of simulations available as part of the Land Data Assimilation Systems (LDAS; Mitchell et al. 2004; Rodell et al. 2004; Xia et al. 2012c). Moreover, the development efforts have recently resulted in the improvement of the default model physics of Noah LSM through enhancing the conceptual realism of biophysical and hydrological processes as well as providing the multiple parameterization options for various processes (Noah-MP; Niu et al. 2011). In particular, the single source model structure of the default Noah LSM is replaced with a dual source model structure in the Noah-MP LSM to explicitly account for the effect of vegetation canopy on the radiation transfer and surface energy budget computations. Nevertheless, further augmentation of the Noah LSM and/or its updated version (i.e., Noah-MP) and validation against observations remains imperative (Clark et al. 2015; Gayler et al. 2014; Xia et al. 2014; Xia et al. 2012a).

1.3 Water and heat exchanges on the Tibetan Plateau

Since the 1990s, various field campaigns have been conducted [e.g., GEWEX Asian Monsoon Experiment-Tibet (GAME-Tibet; Koike et al. 1999) and CEOP Asia-Australia Monsoon Project in Tibet (CAMP-Tibet; Koike 2004)] and monitoring programs are ongoing [e.g., Tibetan Observation and Research Platform (TORP); Ma et al. 2008] on the Tibetan Plateau. Moreover, several regional scale soil moisture and soil temperature monitoring networks have recently been developed (Su et al. 2011; Yang et al. 2013). All these activities and resulting data sets have advanced and will undoubtedly continue to advance our understanding of the prevailing hydro-meteorological processes linked to water, energy and nutrient cycles in this high-altitude alpine region, also known as the Third Pole Environment (Ma et al. 2009; Piao et al. 2012; Yang et al. 2014).

One of the achievements is the improvement of modeling the water and heat exchanges between the Tibetan land and atmosphere as well as transport through the soil column via analyses of existing data sets in combination with usage of LSMs (Chen et al. 2011; van der Velde et al. 2009; K. Yang et al.

2009). For instance, a newly developed single source LSM has been validated to have identical performance and fewer parameters in comparison to the dual source LSM (i.e. SiB2) for describing the water and heat exchanges across the Tibetan ecosystem (K. Yang et al. 2009; K. Yang et al. 2004). Besides, the diurnally varying roughness length for heat transfer (z_{oh}) has been widely recognized as imperative for reliable daytime land surface temperature (T_{sfc}) and turbulent heat simulation (Chen et al. 2011; Zeng et al. 2012). Chen et al. (2011) showed that the underestimation of T_{sfc} and overestimation of sensible heat flux (H) by the Noah LSM can be resolved by implementing the z_{oh} scheme developed specifically for the Tibetan Plateau by Yang et al. (2008).

In addition, the necessity of vertical soil heterogeneity caused by organic matter and root systems for accurate soil water and heat flow calculations has also been recognized (Y. Chen et al. 2013; Xue et al. 2013; Yang et al. 2005). Yang et al. (2005) and van der Velde et al. (2009) showed that the simulation of turbulent heat fluxes and soil heat/water flow can be improved by making a distinction between the soil thermal/hydraulic properties of the upper and deep soil layers and by calibrating the soil and vegetation parameters. However, van der Velde et al. (2009) arrived at unrealistically high values for the volumetric quartz fraction for the soil matrix to increase the heat conductance through the soil column, which is inconsistent with the findings of Yang et al. (2005) that the existence of dense vegetation roots and abundance of organic matter in the topsoil may significantly reduces the thermal conductivity. Further improvement of the parameterization for the vertical soil heterogeneity is thus still needed.

Moreover, Chen et al. (2011) reported on the imperfect performance of the z_{oh} scheme of Yang et al. (2008) for densely vegetated surfaces (e.g., forest and shrub land), and how this scheme can be used over grid cells with different green vegetation fractions remains unknown (Zeng et al. 2012). Furthermore, regional scale assessment of the aforementioned parameterizations validated at point scale for their ability to reproduce the runoff production at catchment scale has not been investigated. Therefore, further improvement of the model physics and validation against existing observations remains imperative to obtain a better understanding of water and heat exchanges on the Tibetan Plateau and their response to climate change.

1.4 Research objective and questions

The main objective of this thesis is to arrive at a better quantification of the water and heat exchanges at the land-atmosphere interface for a Tibetan alpine

meadow ecosystem. The source region of the Yellow River (SRYR) in the northeastern part of the Tibetan Plateau is selected as the case study due to its great importance to the Yellow River's water resources (see Section 1.1). A comprehensive observational dataset including in-situ micro-meteorological and profile soil moisture/temperature measurements, laboratory soil property measurements of samples, as well as discharge measurements is collected. To understand the processes governing the water and heat exchanges of the alpine meadow ecosystem and predict the observational data sets, the Noah land surface model (LSM) is utilized as the baseline model because it is widely used by the climate and land surface modeling communities to quantify the exchange of water and heat at the land-atmosphere interface (see Section 1.2). Besides, the reliability of Noah LSM for the Tibetan Plateau was previously confirmed (see Section 1.3, e.g., Chen et al. 2010; van der Velde et al. 2009; Zeng et al. 2012).

The following research questions are formulated to achieve the objective:

Q1. What is the adequate scheme of the roughness lengths for momentum and heat transfers to predict turbulent heat fluxes for the Tibetan alpine meadow?

Q2. How does the soil organic matter, thermal roughness length and vegetation canopy affect the turbulent and soil heat transport?

Q3. What is the effect of the vertical soil heterogeneity on water and heat exchanges and how can this be included in the model structure of Noah LSM?

Q4. How does the model physics of vertical water and heat exchange processes impact the runoff production at catchment scale?

1.5 Thesis outline

The four research questions are addressed in Chapters 4, 5, 6 and 7 of this thesis respectively. The thesis is structured as follows:

Chapter 2 provides a brief introduction of the study area and the observational data sets;

Chapter 3 introduces the baseline Noah model structure and model physics;

In **Chapter 4** the performance of several newly developed momentum and thermal roughness length schemes for the Noah land surface model (LSM) are evaluated on their ability to reproduce observed variations of roughness lengths, turbulent heat fluxes and surface temperature for three selected periods: a winter (15 December 2009 to 15 January 2010), a spring (8 April to 7 May 2010) and a monsoon period (1 to 30 September 2009);

Chapter 5 presents the augmentations made to Noah model physics associated with the thermal roughness length (based on Chapter 4), vegetation canopy and organic matter effects and the investigation of their impacts on the simulated turbulent and soil heat transport for the majority of the monsoon season (8 June to 30 September 2010);

Chapter 6 describes the augmentations made to Noah model physics associated with the vertical soil heterogeneity including the root water uptake and the soil organic matter effect on the hydraulic properties, and its performance in simulating soil water flow as well as partitioning of turbulent heat fluxes for the majority of the monsoon season;

In **Chapter 7** the modified Noah model physics of vertical water and heat exchange processes presented in Chapters 4, 5 and 6 is applied to investigate its impact on the runoff production at catchment scale, i.e., the source region of the Yellow River (SRYR) for the period of 2001-2010;

Chapter 8 synthesizes the main findings of Chapters 4, 5, 6 and 7 with respect to the four research questions and directions for further research are presented as well.

The logic of the thesis structure is shown in Figure 1.1. The observational data sets (Chapter 2) and the Noah LSM (Chapter 3) form the basis for this study. Chapters 4, 5, and 6 present the investigation of the water and heat exchanges at the land-atmosphere interface, and water and heat transport in the soil column at the point scale. Particularly, the appropriate roughness length scheme recommended in Chapter 4 is further investigated in Chapter 5, and the coupled heat (Chapter 5) and water (Chapter 6) dynamics is implemented in both Chapters 5 and 6, whereas the modified model physics is implemented in Chapter 7 to further investigate its ability in reproducing runoff at the catchment scale. Subsequently, the findings are summarized in Chapter 8.

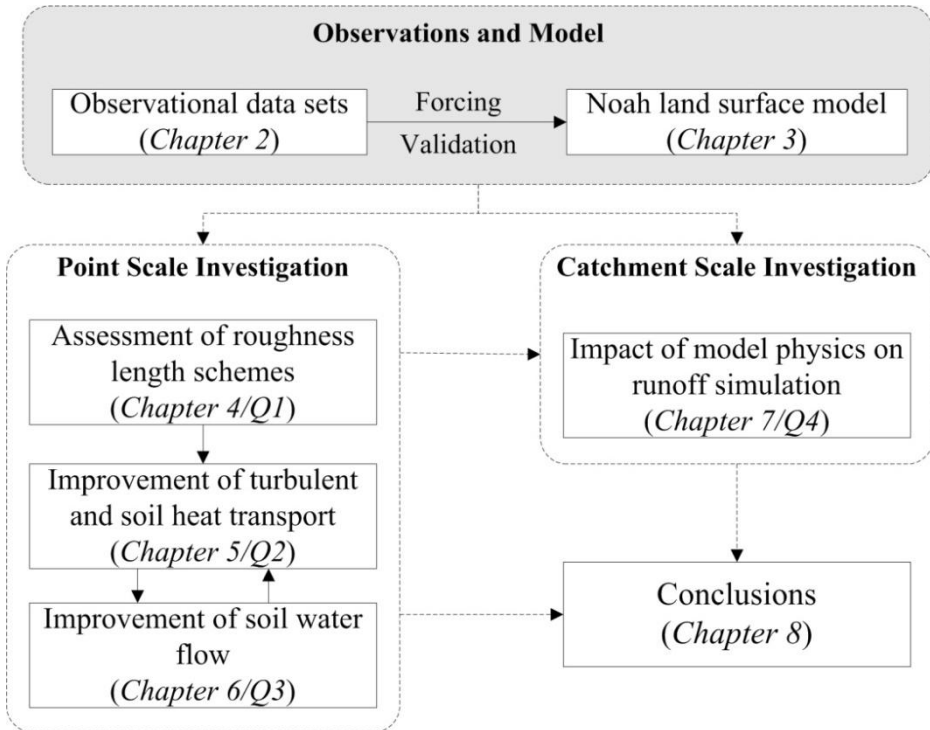


Figure 1.1: Diagram and logic of the thesis structure. Four research questions (Q1-Q4) are answered in Chapters 4-7.

Chapter 2 Study area and in-situ data sets

The source region of the Yellow River (SRYR) in the northeastern part of the Tibetan Plateau is selected as the study area for this thesis, and a comprehensive observational dataset of hydro-meteorological variables and soil properties is collected in Maqu station that located in the southeastern part of the SRYR for the assessment and improvement of Noah land surface model (LSM). This Chapter introduces the study area (i.e., SRYR) and the discharge measurements (Section 2.1), as well as the Maqu observational dataset (Section 2.2).

2.1 Source region of the Yellow River

The source region of the Yellow River (SRYR, Figure 2.1) is located in a transition zone from seasonally frozen ground to discontinuous and continuous permafrost in the northeastern part of the Tibetan Plateau (Jin et al. 2009). The discharge measured at the catchment outlet, Tangnag station, is produced in an area of around 122,000 km² that comprises 16.2 % of Yellow River basin in size, while it contributes to more than 35 % of the total streamflow (Zhou and Huang 2012). Hence, the SRYR is widely regarded as the “water tower” of the Yellow River, but is experiencing a disturbing decline in the streamflow in the past decades (Hu et al. 2011; Zheng et al. 2007; Zhou and Huang 2012).

The elevation in the SRYR varies from 2000 m in the east up to 6300 m in the west with several steeples around the Anyemqen Mountains in the central part. Cold dry winters and rainy summers are characteristic for its climate with annual average daily temperatures ranging from -4 °C to 2 °C decreasing from east to west. The temperature generally remains below 0 °C during the cold season from October to April. The mean annual precipitation varies from 800 mm in the southeast to 200 mm in the northwest with 75 % - 90 % falling during the monsoon season from June till September (Hu et al. 2011; Zheng et al. 2007). Alpine grassland and loamy soils dominate the land cover in the region.

Four discharge stations are operated by the Yellow River Conservancy Commission (YRCC) at Huangheyuan, Jimai, Maqu and Tangnag. For this study, only the monthly streamflow data from the Tangnag station are available for the period of 2002-2009, and these are utilized to investigate the performance of Noah LSM in simulating runoff at catchment scale in Chapter 7. Streamflow dynamics at Tangnag station are mainly forced by a natural drivers and are not

affected by large dams, irrigation diversions or any other major anthropogenic influences (Cuo et al. 2013).

2.2 Maqu observational dataset

Maqu Climatic and Environmental Observation station (Figure 2.1) is located in the southeastern part of the SRYR, with elevations varying from 3200 to 4200 m above sea level (a.s.l.). The landscape in this region is dominated by alpine meadows (e.g., *Cyperaceae* and *Gramineae*) with a height of 15 cm during summers and about 5 cm during winters. The climate is characterized by cold dry winters and rainy summers, with a mean annual air temperature of 1.2 °C, and the mean air temperatures of the coldest month (January) and warmest month (July) are -10 °C and 11.7 °C respectively. The soil starts freezing around the beginning of November, while the frozen ground is fully thawed around the beginning of May. The precipitation is around 500-600 mm annually, with more than 70 % falling during the monsoon season from June till September. The groundwater level in this area is situated at 8.5-10.0 m below the ground.

2.2.1 Hydro-meteorological variables

Maqu station is equipped with a micro-meteorological observing system and a regional scale soil moisture and soil temperature (SMST) monitoring network (Figure 2.1). The micro-meteorological observing system consists of a 20 m Planetary Boundary Layer (PBL) tower providing wind speed and direction, air humidity and temperature measurements at five levels (i.e., 18.15, 10.13, 7.17, 4.2 and 2.35 m), and an eddy-covariance (EC) system installed at a height of 3.2 m for measuring the turbulent sensible and latent heat fluxes. Instrumentations for measuring four radiation components (i.e., upward and downward shortwave and longwave radiations), air pressure and precipitation are also mounted on the PBL tower.

The network of 20 SMST monitoring sites covering an area of 40 km by 80 km centered on the micro-meteorological observing system has been setup as a part of the Tibetan Plateau Observatory (Tibet-Obs) primarily for the calibration/validation of satellite based soil moisture products (Dente et al. 2012; Su et al. 2011), as well as to improve our understanding of land surface processes on the Plateau (Su et al. 2013). Table 2.1 summarizes the equipment deployed and the hydro-meteorological variables measured at Maqu station.

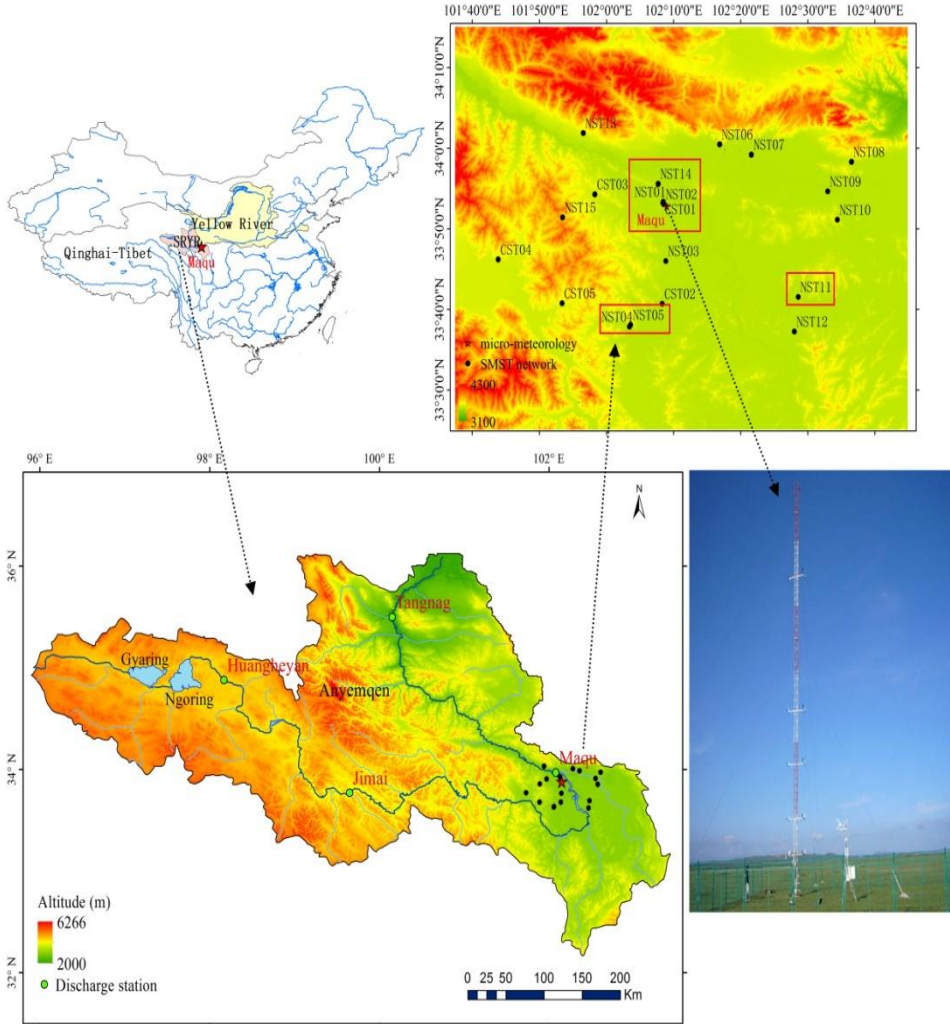


Figure 2.1: Location of the source region of the Yellow River (SRYR) and the Maqu station showed on top of the SRTM-90 digital elevation model.

All the measurements are processed to values for every 30-min interval, whereby the ground surface temperature is computed from measured upward and downward longwave radiations using the Stefan-Boltzmann equation:

$$\varepsilon\sigma T_{sfc}^4 = L^{\uparrow} - (1 - \varepsilon)L^{\downarrow} \quad (2.1)$$

where T_{sfc} is the ground surface temperature (K), L^{\uparrow} and L^{\downarrow} are the upward and downward longwave radiation ($W m^{-2}$) respectively, ε is the surface emissivity (-), and σ is the Stefan-Boltzmann constant (taken as $5.67 \times 10^{-8} W m^{-2} K^{-4}$).

² K⁴). In this study, the surface emissivity is taken as 0.95 for bare ground (November to April) and 0.98 for grassland (May to October, Brutsaert 1982). Additional details for the measurements and data-processing can be found in Dente et al. (2012) and Zheng et al. (2014).

Table 2.1: Equipment deployed and the hydro-meteorological variables measured at Maqu station

System	Items	Level (m)	Sensor
PBL Tower	Wind speed and wind direction	2.35, 4.2, 7.17,	Gill WindSonic 2D
	Air temperature	10.13, 18.15	Vaisala HMP45C
	Humidity		
Eddy- covariance System	Air pressure	2.0	Vaisala CS105
	Radiation flux		Kipp & Zonen CNR1
	Precipitation	1.5	Young 52202 tipping bucket raingauge
SMST	Wind fluctuation		CSAT3 3D sonic anemometer
	Sensible heat flux	3.2	Campbell LI-COR 7500
	Latent heat flux		
	Soil moisture and soil temperature	-0.05, -0.1, -0.2, -0.4, -0.8	EC-TM ECH ₂ O probe

2.2.2 Soil properties

Soil samples are collected at two SMST sites (CST01 and NST01) near the micro-meteorological observing system, as well as two sites (NST04 and NST11) located in a wetland environment (see Figure 2.1) for quantifying the soil texture and hydraulic/thermal properties through laboratory analyses. Two or three soil profiles are obtained from each site, whereby samples are taken at depths of 0.1, 0.3, and 0.6 m. Duplicates of undisturbed soil samples are collected by soil cutting ring augers, whereby the hydraulic characterization is complemented by field measurement of the saturated hydraulic conductivity (K_s) with the Guelph Permeameter manufactured by Soilmoisture Equipment Corp.

Table 2.2: Averaged feature of soil properties measured by field and laboratory experiments in this study

Site	Depth (cm)	Sand (%)	Clay (%)	Texture	m_{soc} (%)	ρ_b (g cm ⁻³)	θ_s (m ³ m ⁻³)	K_s (10 ⁻⁶ m s ⁻¹)
CST01	5-15	34.78	9.38	Silt Loam	2.78	1.05	0.55	1.18
	20-40a	39.49	9.01	Silt Loam	2.18	1.21	0.51	
	20-40b	65.56	5.45	Sandy Loam	0.46	1.59	0.41	0.21
	55-70	57.92	6.65	Sandy Loam	0.51	1.56	0.42	0.04
NST01	5-15	36.07	7.42	Silt Loam	1.57	1.38	0.52	1.19
	20-40	52.33	6.65	Sandy Loam	1.57	1.32	0.45	0.39
	55-70	61.24	5.92	Sandy Loam	0.53	1.42	0.42	0.33
NST04	5-15	36.57	7.10	Organic Soil	18.25	0.50	0.76	2.15
	20-40	27.29	8.94	Organic Soil	12.78	0.55	0.73	0.56
	55-70	18.24	9.42	Silt Loam	6.28	0.97	0.64	0.19
NST11	5-15	18.56	9.01	Organic Soil	14.92	0.49	0.72	2.11
	20-40	30.17	11.01	Silt Loam	3.45	1.05	0.59	0.41
	55-70a	29.16	11.22	Silt Loam	1.75	1.24	0.54	
	55-70b	48.05	6.01	Sandy Loam	2.22	1.29	0.54	0.17

The soil samples are transported to the laboratory for precise measurement of the soil texture (sand, clay and silt), organic carbon mass content (m_{soc}), bulk density (ρ_b), porosity (θ_s), soil water retention curve and soil heat conductivity (κ_h). Soil texture is measured with a Malvern Mastersizer 2000 particle size analyzer, and organic carbon mass content is measured with a Total Organic

Carbon Analyzer (SHIMADZU-TOC-VCPH). Soil porosity is calculated from the difference of the saturated and dry soil weight of the cutting ring with known volume (100 cm³) and weight, and bulk density is calculated from the dry soil weight. Soil water contents associated with 11 pressure heads from 0 up to 15 bars are performed with the Soilmoisture Equipment Corp. Pressure Membrane Instrument. Thermal conductivities for 12 soil moisture contents varying from saturation to dry are measured with the KD2 Thermal Properties Analyzer of Decagon Devices Inc. Additional information on the procedures adopted for the soil sampling and laboratory experiments can be found in Chen et al. (2012).

Table 2.2 lists the mean values for the soil texture, m_{soc} , ρ_b , θ_s and K_s found across the soil profile at the four SMST sites. The measurements demonstrate that the soils in the Maqu region are stratified, whereby in the upper layer a higher m_{soc} is found, the percentage sand typically increases with depth and a substantial organic soil layer is found for the wetland ecosystems. This soil stratification can be associated with higher θ_s and K_s , while the ρ_b is lower.

Chapter 3 Noah land surface model

The Noah land surface model (LSM) originates from the Oregon State University (OSU) LSM and has a long history of development through multi-institutional collaboration (Chen et al. 1997; Chen et al. 1996; Ek et al. 2003; Koren et al. 1999; Livneh et al. 2010; Mahrt and Ek 1984; Mahrt and Pan 1984; Pan and Mahrt 1987; Schaake et al. 1996). The Noah LSM is originally designed for moderate complexity and good computational efficiency without considering the sub-grid spatial variability, and it is widely used by the climate modeling community (e.g., the WRF model community) to quantify the exchange of water and heat at the land-atmosphere interface, and is one of the LSMs deployed for NASA's Land Data Assimilation Systems (Mitchell et al. 2004; Rodell et al. 2004; Xia et al. 2012c).

The model structure consists of a modestly complex canopy resistance scheme (Chen et al. 1996) linked to the diurnal Penman approach (Mahrt and Ek 1984) for simulating the latent heat flux and a surface energy balance approach whereby the entire soil-snow-vegetation system is represented as a single heat/water vapor source. A four-layer soil scheme is implemented with the thermal diffusion equation for simulating heat transport and the diffusivity form of Richards' equation for water flow (Mahrt and Pan 1984; Pan and Mahrt 1987). A simple water balance approach (Schaake et al. 1996) is adopted to simulate the surface runoff and the cold season physics are implemented as described in Koren et al. (1999). A schematization of the model structure is given in Figure 3.1 (<http://www.ral.ucar.edu/research/land/technology/lsm.php>).

The Noah LSM is selected as the baseline model for the research presented in this thesis, and this Chapter presents the model physics by default implemented for Version 3.4.1 relevant for this thesis, and additional information can be also found in existing literature (e.g., Ek et al. 2003; Niu et al. 2011; van der Velde et al. 2009). Section 3.1 and Section 3.2 present respectively the model physics associated with the warm season surface energy and water budgets. The freeze-thaw processes are introduced in Section 3.3, and Section 3.4 provides the default vegetation, soil and topographic parameterizations. Model physics associated with snow processes is referred to existing literature (Barlage et al. 2010; Koren et al. 1999; Livneh et al. 2010).

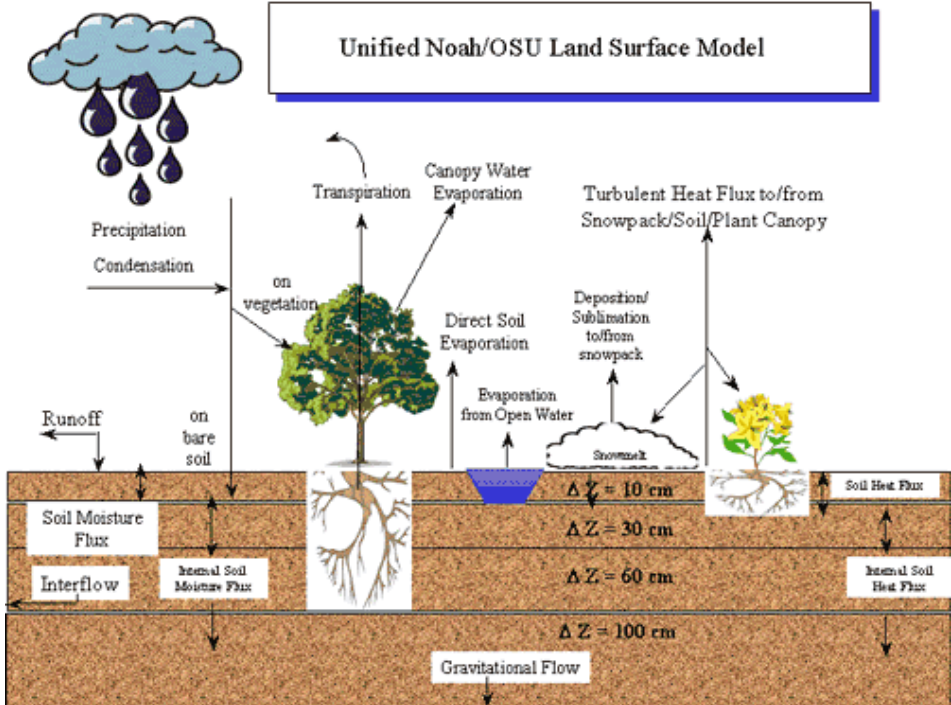


Figure 3.1: Schematization of the Noah model structure.

3.1 Surface energy balance

The surface energy balance equation solved by the Noah LSM can be written as:

$$S^{\downarrow} - S^{\uparrow} + \varepsilon(L^{\downarrow} - \sigma T_{sfc}^4) = H + LE + G_0 \quad (3.1)$$

where S^{\downarrow} and S^{\uparrow} are the downward and upward shortwave radiations (W m^{-2}) respectively, L^{\downarrow} is the downward longwave radiation (W m^{-2}), T_{sfc} is the ground surface temperature (K), ε is the surface emissivity (-), σ is the Stefan-Boltzmann constant (taken as $5.67 \times 10^{-8} \text{ W m}^{-2} \text{ K}^{-4}$), H is the sensible heat flux (W m^{-2}), LE is the latent heat flux (W m^{-2}), and G_0 is the ground surface heat flux (W m^{-2}).

3.1.1 Turbulent sensible and latent heat fluxes

The sensible heat flux is computed using the bulk transfer equations based on the Monin-Obukhov similarity theory (MOST; i.e., Chen et al. 1997):

$$H = \rho c_p C_h u (\theta_{sfc} - \theta_a) \quad (3.2)$$

$$C_h = \frac{k^2}{\left[\ln\left(\frac{z_h}{z_{0m}}\right) - \Psi_m\left(\frac{z_h}{L}\right) + \Psi_m\left(\frac{z_{0m}}{L}\right) \right] \left[\ln\left(\frac{z_h}{z_{0h}}\right) - \Psi_h\left(\frac{z_h}{L}\right) + \Psi_h\left(\frac{z_{0h}}{L}\right) \right]} \quad (3.3)$$

$$L = -\frac{\rho c_p u_*^3 \theta_a}{kgH} \quad (3.4)$$

$$u_*^2 = C_m \cdot u^2 \quad (3.5)$$

$$C_m = \frac{k^2}{\left[\ln\left(\frac{z_h}{z_{0m}}\right) - \Psi_m\left(\frac{z_h}{L}\right) + \Psi_m\left(\frac{z_{0m}}{L}\right) \right]^2} \quad (3.6)$$

where ρ is the density of air (kg m^{-3}), c_p is the specific heat of air ($\text{J kg}^{-1} \text{K}^{-1}$), C_h is the surface exchange coefficient for heat transfer (-), u is the mean wind speed (m s^{-1}), θ_{sf} is the potential temperature at the surface (K), θ_a is the potential air temperature (K), k is the von Karman constant (taken as 0.4), z_h is the observation height of air temperature and/or wind speed (m), z_{0m} is the roughness length for momentum transfer (m), z_{0h} is the roughness length for heat transfer (m), L is the Obukhov length (m), u_* is the friction velocity (m s^{-1}), g is the gravity acceleration (m s^{-2}), C_m is the surface exchange coefficient for momentum transfer (-), Ψ_m and Ψ_h are the stability correction functions for momentum and sensible heat transfer respectively (-), and the stability functions proposed by Paulson (1970) are adopted in current Noah LSM as (Chen et al. 1997; Sun and Mahrt 1995):

$$\Psi_m = \begin{cases} -5\zeta & 0 < \zeta < 1 \\ 2 \ln((1+x)/2) + \ln((1+x^2)/2) - 2 \tan^{-1}(x) + \pi/2 & -5 < \zeta < 0 \end{cases} \quad (3.7)$$

$$\Psi_h = \begin{cases} -5\zeta & 0 < \zeta < 1 \\ 2 \ln((1+x^2)/2) & -5 < \zeta < 0 \end{cases} \quad (3.8)$$

$$\zeta = z_h / L \quad (3.9)$$

$$x = (1 - 16\zeta)^{1/4} \quad (3.10)$$

The potential evapotranspiration (LE_p) is calculated diurnally using a Penman-based approach (Chen et al. 1996; Mahrt and Ek 1984):

$$LE_p = \frac{\Delta(R_n - G_0) + \rho\lambda C_h u(q_s - q)}{1 + \Delta} \quad (3.11)$$

$$R_n = S^\downarrow - S^\uparrow + \varepsilon(L^\downarrow - \sigma T_{sfc}^4) \quad (3.12)$$

where Δ is the slope of the relation between the saturated vapor pressure and the temperature (kPa K^{-1}), R_n is the net radiation (W m^{-2}), λ is the latent heat of vaporization (J kg^{-1}), q_s and q are the saturated and actual specific humidity (kg kg^{-1}). Note that herein the surface exchange coefficient for water vapor transport is assumed to be equivalent to that of heat transfer. The estimation of actual evapotranspiration (LE) is performed by applying a Jarvis-type surface resistance scheme to impose soil and atmospheric constraints (Chen et al. 1996).

3.1.2 Ground surface heat flux

The ground surface heat flux is calculated following Fourier's law using the temperature gradient between the surface and the mid-point of the first soil layer:

$$G_0 = \kappa_{h0} \frac{T_{sfc} - T_{s1}}{\Delta z_1} \quad (3.13)$$

where κ_{h0} is the thermal heat conductivity of the surface layer ($\text{W m}^{-1} \text{K}^{-1}$), T_{s1} is the temperature of the first soil layer (K), and Δz_1 is the depth between the surface and the mid-point of the first soil layer (m).

3.1.3 Ground surface temperature

For the estimation of the ground surface temperature the following linearization based on a first-order Taylor series expansion is utilized (van der Velde et al. 2009):

$$T_{sfc}^4 \approx T_a^4 \left[1 + 4 \left(\frac{T_{sfc} - T_a}{T_a} \right) \right] \quad (3.14)$$

Substitution of eq. (3.14) into the surface energy balance equation (eq. (3.1)) yields the following expression for the ground surface temperature:

$$T_{sfc} = T_a + \frac{S^\downarrow - S^\uparrow + \varepsilon L^\downarrow - H - LE - G_0}{4\varepsilon\sigma T_a^3} - \frac{1}{4} T_a \quad (3.15)$$

where T_a is the air temperature (K). Additional information on the numerical implementation of the surface energy balance equations (eqs. (3.1)-(3.15)) can be found in Ek and Mahrt (1991).

3.1.4 Soil heat flow

The transport of heat through the soil column is governed by the thermal diffusion equation:

$$C_s \frac{\partial T}{\partial t} = \frac{\partial}{\partial z} \left(\kappa_h \frac{\partial T}{\partial z} \right) \quad (3.16)$$

where κ_h is the thermal heat conductivity ($\text{W m}^{-1} \text{K}^{-1}$), and C_s is the thermal heat capacity ($\text{J m}^{-3} \text{K}^{-1}$).

The solution to eq. (3.16) is achieved using the fully implicit Crank-Nicholson scheme. The temperature at the bottom boundary (at a depth of 8 m below the ground surface) is generally taken as the annual mean near-surface air temperature, whereas the top boundary is confined by the ground surface temperature (see Section 3.1.3).

3.1.5 Soil thermal parameterization

The heat flow through the soil column is parameterized by the thermal heat conductivity, κ_h , and capacity, C_s , which depend on constituents of the soil matrix. The thermal heat capacity is calculated using the following equation:

$$C_s = \theta C_w + (1 - \theta_s) C_{soil} + (\theta_s - \theta) C_{air} \quad (3.17)$$

where θ is the soil moisture content ($\text{m}^3 \text{m}^{-3}$), θ_s is the porosity ($\text{m}^3 \text{m}^{-3}$), C represents the heat capacity ($\text{J m}^{-3} \text{K}^{-1}$), and the subscripts ‘w’, ‘soil’, and ‘air’ refer to water, solid soil, and air. In the Noah LSM, C_w , C_{soil} and C_{air} are taken as 4.2×10^6 , 2.0×10^6 and $1005 \text{ J m}^{-3} \text{K}^{-1}$, respectively.

The thermal heat conductivity is calculated as a combination of the saturated (κ_{sat}) and dry (κ_{dry}) thermal heat conductivity weighed proportional to the degree of saturation (Johansen 1975):

$$\kappa_h(\theta) = K_e (\kappa_{sat} - \kappa_{dry}) + \kappa_{dry} \quad (3.18)$$

where K_e is the Kersten (1949) number representing the degree of saturation and is defined by:

$$K_e = \begin{cases} \log_{10}(\theta/\theta_s) + 1.0, & \text{for } \theta/\theta_s > 0.1 \\ 0.0, & \text{for } \theta/\theta_s \leq 0.1 \end{cases} \quad (3.19)$$

The κ_{dry} is calculated using a semi-empirical equation:

$$\kappa_{dry} = \frac{0.135 \rho_b + 64.7}{2700 - 0.947 \rho_b} \quad (3.20)$$

$$\rho_b = (1 - \theta_s) \cdot 2700 \quad (3.21)$$

where ρ_b is the bulk density of dry soil (kg m^{-3}).

The κ_{sat} is calculated as the geometric mean of the heat conductivities of the materials present within the soil matrix:

$$\kappa_{sat} = \kappa_{soil}^{1-\theta_s} \kappa_w^{\theta_s} \quad (3.22)$$

where κ_w is the heat conductivity of water (taken as $0.57 \text{ W m}^{-1} \text{ K}^{-1}$), and κ_{soil} is the heat conductivity of solid soil that is estimated as a function of the volumetric quartz fraction (qtz):

$$\kappa_{soil} = \kappa_{qtz}^{qtz} \kappa_o^{1-qtz} \quad (3.23)$$

where κ_{qtz} and κ_o are the heat conductivities of quartz and other soil particles, which are taken as 7.7 and $2.0 \text{ W m}^{-1} \text{ K}^{-1}$, respectively. The volumetric quartz fraction, qtz , is taken equivalent to the fractional sand (Peters-Lidard et al. 1998).

The Noah LSM has a single heat source model structure; viz. the vegetation and soil surface are represented by a single layer. Because the two media have clearly different thermal properties and dynamics, κ_{h0} is the conductivity defining the heat transport from the surface to the mid-point of the upper soil layer reduced as function of the green canopy according to:

$$\kappa_{h0} = \kappa_h(\theta_1) \cdot \exp(-\beta_{veg} GVF) \quad (3.24)$$

where GVF is the green vegetation fraction (-), β_{veg} is the constant muting factor taken as 2.0 , and θ_1 is the soil moisture content of the first soil layer ($\text{m}^3 \text{ m}^{-3}$).

Exponential decay of the green canopy is also imposed on the heat conductivity of the first soil layer (κ_{h1}), while the heat conductivities of other soil layers only depend on the constituents of the soil matrix, which are calculated as follows:

$$\kappa_{hi} = \begin{cases} \kappa_h(\theta_i) \cdot \exp(-\beta_{veg} GVF), & \text{for } i = 1 \\ \kappa_h(\theta_i), & \text{for } i > 1 \end{cases} \quad (3.25)$$

where i is the soil layer, κ_{hi} is the heat conductivity of each soil layer adopted by eq. (3.16), and $\kappa_h(\theta_i)$ is calculated using eqs. (3.18)-(3.23).

3.1.6 Roughness length parameterization

The surface exchange coefficient for heat (C_h , eq. (3.3)) is of importance for a reliable calculation of the H (eq. (3.2)) and LE_p (eq. (3.11)), which depends on parameterization of roughness lengths for momentum (z_{0m}) and heat (z_{0h})

transfer. The roughness length for momentum transport is calculated as a function of the time-varying GVF :

$$z_{0m} = (1 - GVF_{norm}) \cdot z_{0m,min} + GVF_{norm} \cdot z_{0m,max} \quad (3.26)$$

$$GVF_{norm} = \frac{GVF - GVF_{min}}{GVF_{max} - GVF_{min}} \quad (3.27)$$

where $z_{0m,min}$ and $z_{0m,max}$ are prescribed based on land cover type.

The Reynolds number (Re_*) dependent formulation of the kB^{-1} ($=\ln(z_{0m}/z_{0h})$) concept proposed by Zilitinkevich (1995) is utilized to calculate the thermal roughness length (Chen et al. 1997) as follows:

$$z_{0h} = z_{0m} \cdot \exp\left(-kC_{zil}\sqrt{Re_*}\right) \quad (3.28)$$

$$Re_* = u_* \cdot z_{0m} / \nu \quad (3.29)$$

where ν is the kinematic molecular viscosity (taken as $1.5 \times 10^{-5} \text{ m}^2 \text{ s}^{-1}$), and C_{zil} is an empirical constant specified as 0.1 analogous to values derived from measurements over grassland (Chen et al. 1997).

3.2 Surface water budget

The surface water budget in the Noah LSM is calculated as follows for each time-step:

$$\frac{\partial W}{\partial t} = \begin{cases} P - ET_a - R, & ET_p > 0 \\ P - ET_p - R, & ET_p \leq 0 \end{cases} \quad (3.30)$$

where dW/dt is the change in water storage (m), P is the total precipitation (m), ET_a is the actual evapotranspiration (m), ET_p is the potential evapotranspiration (m), and R is the total runoff (m) all within a model time step. The second case in above equation (i.e., $ET_p \leq 0$) represents the condition when the dew forms.

For the bare soil, ET_a and dW/dt represent the direct evaporation from the top shallow soil layer and change of water storage in the soil column, respectively. Over vegetated areas, ET_a is the sum of soil evaporation (E_s), evaporation of precipitation intercepted by the canopy (E_c) and transpiration via canopy and roots (E_r), and dW/dt represents both the changes in canopy intercepted water (W_c) and soil water storage (W_s). The calculations of soil water flow (i.e., soil water storage change) and runoff are provided below, while the estimations of ET_a and ET_p are given in Section 3.1.1. Additional information about the

computations of canopy intercepted water, ET_a , as well as soil and canopy resistances can be found in Chen et al. (1996).

3.2.1 Soil water flow

The diffusivity form of Richards' equation is utilized by the Noah LSM for the simulation of soil water flow, which can be formulated as:

$$\frac{\partial \theta}{\partial t} = \frac{\partial}{\partial z} \left(D(\theta) \frac{\partial \theta}{\partial z} \right) + \frac{\partial K(\theta)}{\partial z} + S(\theta) \quad (3.31)$$

where θ is the soil moisture content ($\text{m}^3 \text{m}^{-3}$), t is the time (s), D is the soil water diffusivity ($\text{m}^2 \text{s}^{-1}$), K is the hydraulic conductivity (m s^{-1}), z is the soil depth (m), S represents sources and sinks (i.e., precipitation and evapotranspiration, m s^{-1}). The first term on the right-hand side of eq. (3.31) defines the diffusive flow component driven by the vertical soil water potential (ψ) gradient. The second term characterizes the convective flow mechanism forced by gravity. Through the gravity induced convective flow, water is transported downwards, whereas the diffusive flow mechanism may also transport water downwards or upwards depending on the direction of the ψ gradient induced by the soil moisture profile. The latter ensures the ability to simulate capillary rise. The Noah soil model consists by default of a 2 m homogeneous soil column with four layers of 0.1, 0.3, 0.6 and 1.0 m with increasing thickness towards the bottom (see Figure 3.1).

Time integration of eq. (3.31) is obtained via the implicit Crank-Nicolson finite difference scheme expressed for Richards' equation as:

$$\Delta z_i \frac{\theta_i^{n+1} - \theta_i^n}{\Delta t} = D_i^{n+1} \frac{\theta_{i+1}^{n+1} - \theta_i^{n+1}}{z_{i+1} - z_i} - D_{i-1}^{n+1} \frac{\theta_i^{n+1} - \theta_{i-1}^{n+1}}{z_i - z_{i-1}} - (K_i^{n+1} - K_{i-1}^{n+1}) + \Delta z_i \cdot S_i \quad (3.32)$$

where n and i represent the time and spatial step separately, Δz represents the depth of the soil layer (m), and z represents the position of the mid-point of the soil layer (m). Within Noah the implicit Crank-Nicolson finite difference scheme is solved using the tri-diagonal matrix algorithm.

3.2.2 Soil hydraulic parameterization

Both convective and diffusive flow mechanisms described in eq. (3.31) are parameterized by the transport coefficients, K and D , which depend both on the soil texture and soil moisture content. The ψ - θ , K - θ and D - θ relationships are parameterized as functions of soil texture by an empirical soil hydraulic scheme proposed by Campbell (1974):

$$\psi(\theta) = \psi_s (\theta/\theta_s)^{-b} \quad (3.33)$$

$$K(\theta) = K_s (\theta/\theta_s)^{2b+3} \quad (3.34)$$

$$D(\theta) = D_s (\theta/\theta_s)^{b+2} \quad (3.35)$$

$$D_s = b \cdot K_s (\psi_s / \theta_s) \quad (3.36)$$

where ψ_s is the soil water potential at air-entry (m), K_s is the saturated hydraulic conductivity (m s^{-1}), θ_s is the porosity ($\text{m}^3 \text{m}^{-3}$), and b is an empirical parameter (-) related to the pore-size distribution of the soil matrix. The soil type specific hydraulic parameters (i.e., K_s , θ_s , ψ_s and b) are obtained in Noah from the class pedotransfer function (PTF) provided in Cosby et al. (1984).

3.2.3 Root water uptake

Root water uptake for evapotranspiration is the main sink term (S) of eq. (3.31) responsible for the redistribution of water across the soil column. Total transpiration (E_t) is allocated to each soil layer according to an effective root fraction ($r_{e,i}$):

$$E_{t,i} = E_t \cdot r_{e,i} \quad (3.37)$$

$$r_{e,i} = \frac{f_{sw,i} \cdot f_{root,i}}{\sum_{i=1}^{nroot} f_{sw,i} \cdot f_{root,i}} \quad (3.38)$$

$$f_{root,i} = f_{root,i} + f_{sw,i} - \sum_{i=1}^{nroot} f_{sw,i} / nroot \quad (3.39)$$

$$f_{sw,i} = \frac{\theta_i - \theta_w}{\theta_c - \theta_w} \quad (3.40)$$

$$f_{root,i} = \frac{\Delta z_i}{\sum_{i=1}^{nroot} \Delta z_i} \quad (3.41)$$

where Δz_i is the depth of the i th soil layer (m), $nroot$ is the total number of root layers (-), θ_w is the soil moisture content at wilting point ($\text{m}^3 \text{m}^{-3}$), θ_c is the critical soil moisture content ($\text{m}^3 \text{m}^{-3}$) below which the simulated transpiration is reduced due to water stress, $f_{sw,i}$ and $f_{root,i}$ are the soil water stress and root fractions for the i th soil layer. Note that the root distribution is assumed to be vertically uniform with the depth as weighing factor (eq. (3.41)). Moreover, the root fraction is modified ($f_{root,i}$) to represent the water stress compensation mechanism (eq. (3.39)), which implicates that water stress in one part of the

root zone can be compensated by enhanced water uptake from other more moist parts (Li et al. 2001). In Noah, θ_c is defined at a drainage flux of 0.5 mm d⁻¹ and wilting point θ_w is taken at $\psi = -200$ m.

3.2.4 Surface runoff and drainage

The surface runoff (R_s , in m) is generated when the effective precipitation (P_x , in m) exceeds the infiltration capacity of soil column (I_{max} , in m) as in Schaake et al. (1996):

$$R_s = P_x - I_{max} \quad (3.42)$$

$$I_{max} = \frac{P_x \cdot W_d [1 - \exp(-K_{dt} \Delta t)]}{P_x + W_d [1 - \exp(-K_{dt} \Delta t)]} \quad (3.43)$$

where W_d is the total soil moisture deficit in the soil column (m), K_{dt} is an empirical constant and taken as 3.0 day⁻¹, Δt is the model time step (s). For the bare soil, the effective precipitation is equal to the total precipitation (P), while it represents the excess precipitation after canopy interception over vegetated areas.

Gravitational free drainage (R_b , in m) from the model bottom is formulated as:

$$R_b = slope \cdot K(\theta_d) \cdot \Delta t \quad (3.44)$$

where *slope* is a slope index between 0 and 1 that depending on the grid slope derived from the digital elevation model, and $K(\theta_d)$ is the hydraulic conductivity of the bottom soil layer (m s⁻¹) that can be estimated by eq. (3.34).

3.3 Freeze-thaw transitions

To account for soil moisture phase change during freeze-thaw transitions, a source/sink term is added to the thermal diffusion equation (eq. (3.16)) as in Koren et al. (1999):

$$C_s(\theta, \theta_{ice}) \frac{\partial T}{\partial t} = \frac{\partial}{\partial z} \left(\kappa_h(\theta, \theta_{ice}) \frac{\partial T}{\partial z} \right) + \rho_{ice} L_f \frac{\partial \theta_{ice}}{\partial t} \quad (3.45)$$

where ρ_{ice} is the density of ice (kg m⁻³), L_f is the latent heat of fusion (J kg⁻¹), θ is the total soil water content (m³ m⁻³), θ_{ice} is the soil ice content (m³ m⁻³). The heat source/sink term is determined by the soil water phase equilibrium estimated using the water potential-freezing point depression equation as well as the available heat (Koren et al. 1999). The thermal parameterization (see Section 3.1.5) is modified to consider the effect of ice content as in Peters-Lidard et al. (1998).

With the assumption that liquid water flow in the frozen soil is analogous to that in unfrozen soil, the diffusivity form of Richards' equation (eq. (3.31)) can be also adopted to estimate unfrozen or liquid soil water movement:

$$\frac{\partial \theta_{liq}}{\partial t} = \frac{\partial}{\partial z} \left(D(\theta_{liq}) \frac{\partial \theta_{liq}}{\partial z} \right) + \frac{\partial K(\theta_{liq})}{\partial z} + S(\theta) \quad (3.46)$$

where θ_{liq} is the unfrozen/liquid soil water content ($\text{m}^3 \text{m}^{-3}$).

The soil hydraulic scheme (see Section 3.2.2) is also modified for the frozen soil condition as:

$$K(\theta_{liq}) = K_s \left(\theta_{liq} / \theta_s \right)^{2b+3} \quad (3.47)$$

$$D(\theta_{liq}) = f_{un} \cdot D_s \left(\theta_{liq} / \theta_s \right)^{b+2} + (1 - f_{un}) \cdot D_s \left(\min(\theta_{liq}, 0.05) / \theta_s \right)^{b+2} \quad (3.48)$$

$$f_{un} = 1 / \left[1 + \left(500 \cdot \max \left(\sum_{i=1}^4 \theta_{ice,i} \right) \right)^3 \right] \quad (3.49)$$

where f_{un} is an empirical factor to avoid that the numerical truncation error affects the estimation of unfrozen water movement.

The surface runoff over frozen soil includes the direct runoff from the impermeable frozen area (f_{imp} , -) and the infiltration-excess runoff from the rest of the model grid (i.e., eqs. (3.42)-(3.43)) as:

$$R_s = f_{imp} P_x + (1 - f_{imp}) \frac{P_x^2}{P_x + W_d [1 - \exp(-K_{dt} \Delta t)]} \quad (3.50)$$

The fraction of impermeable frozen area is approximated by a gamma distribution of soil ice content (W_{ice} , m):

$$f_{imp} = e^{-v} \sum_{i=1}^{\alpha} \frac{v^{\alpha-i}}{\Gamma(\alpha - i + 1)} \quad (3.51)$$

$$v = \alpha \frac{W_{cr}}{W_{ice}} \quad (3.52)$$

$$W_{ice} = \sum_{i=1}^4 \theta_{ice,i} \cdot \Delta z_i \quad (3.53)$$

where α is a shape parameter of the gamma distribution and taken as 3 (-), and W_{cr} is the critical ice content above which the frozen ground is impermeable and is taken as 0.15 m.

Gravitational free drainage (eq. (3.44)) is modified as:

$$R_b = slope \cdot K(\theta_{liq,4}) \cdot \Delta t \quad (3.54)$$

where $K(\theta_{liq,4})$ is estimated by eq. (3.47) that considers only the unfrozen water.

3.4 Model parameters

Tables 3.1 and 3.2 lists respectively the soil specific hydraulic and thermal parameters (Sections 3.1.4 and 3.2.2) and predefined vegetation parameters (Sections 3.1.6 and 3.2.3) in Noah LSM that are relevant for soil and vegetation types adopted in this thesis. In addition, Table 3.3 lists the slope index for drainage calculation as in Sections 3.2.4 and 3.3.

Table 3.1: Soil hydraulic and thermal parameters predefined in Noah LSM

Class	θ_s ($\text{m}^3 \text{m}^{-3}$)	K_s (10^{-6}m s^{-1})	ψ_s (m)	b (-)	qtz (-)
Silt Loam	0.476	2.81	-0.759	5.33	0.25
Sandy Loam	0.434	5.23	-0.141	4.74	0.60
Loam	0.439	3.38	-0.355	5.25	0.40

Table 3.2: Vegetation parameters predefined in Noah LSM

Vegetation type	$nroot$ (-)	$z_{0m,min}$ (m)	$z_{0m,max}$ (m)
Grassland	3	0.10	0.12
Open Shrubland	3	0.01	0.06
Cropland	3	0.05	0.15
Bare land	1	0.01	0.01

Table 3.3: Topographic parameters predefined in Noah LSM

Slope Class	1	2	3	4	5	6	7
Percent Slope (%)	0-8	8-30	> 30	0-30	0-8 & >30	≥ 8	≥ 0
Slope Index (-)	0.1	0.5	1.0	0.35	0.55	0.8	0.63

Chapter 4 Assessment of roughness length schemes*

4.1 Introduction

Models of turbulent heat flux transfer between the land surface and atmosphere usually employ the bulk formulations based on the Monin-Obukhov similarity theory (MOST; Brutsaert 1998; Garratt 1994; Su et al. 2001). The MOST relates the turbulent sensible heat flux (H) to the gradient of the ground surface temperature (T_{sfc}) and the temperature in the atmospheric surface layer. To accurately calculate H by means of similarity theory, the roughness lengths for momentum (z_{0m}) and heat (z_{0h}) transfer must be determined (Su et al. 2001). Both parameters cannot be measured directly. Their values are ideally determined using the bulk transfer equations from wind and temperature profile measurements (Ma et al. 2002; Schaudt 1998; Sun 1999; Yang et al. 2003), and/or from single-level sonic anemometer measurements (Yaoming Ma et al. 2008; Martano 2000; Sun 1999). The lack of profile and sonic anemometer data in many regions makes it, however, difficult to determine both parameters on a global scale.

Many studies have been conducted to relate the momentum roughness length z_{0m} to simple geometric characteristics of the surface, such as canopy height (Brutsaert 1982), leaf area index (LAI ; Su 2002), normalized difference vegetation index ($NDVI$; Bastiaanssen et al. 1998), land cover (Wiernga 1993) and green vegetation fraction (GVF ; Zheng et al. 2012). Meanwhile, the thermal roughness length z_{0h} is usually converted from z_{0m} by the factor kB^{-1} ($kB^{-1} = \ln(z_{0m}/z_{0h})$). The parameterization of kB^{-1} has stimulated numerous theoretical and experimental investigations over past decades. See, for example, Brutsaert (1982), Su et al. (2001) and Yang et al. (2008) for detailed reviews on kB^{-1} . Brutsaert (1982) showed that kB^{-1} can be parameterized by a combination of roughness Reynolds number (Re_*) and vegetation parameters, such as LAI and canopy structure. Sun (1999) also found that kB^{-1} may vary diurnally over homogeneous grassland, and these diurnal variations are not uniquely related to Re_* . Yang et al. (2008) further pointed out that kB^{-1} may be related to the type

*This chapter is based on the paper: Zheng, D., R. van der Velde, Z. Su, M. J. Booij, A. Y. Hoekstra, and J. Wen, 2014: Assessment of Roughness Length Schemes Implemented within the Noah Land Surface Model for High-Altitude Regions. *Journal of Hydrometeorology*, **15**, 921-937.

of flow and the diurnal variations can be more realistically parameterized by a combination of friction velocity (u_*) and friction temperature (θ_*).

Even stronger diurnal patterns in kB^{-1} have been observed over the Tibetan Plateau. Since 1998, intensive field experiments and comprehensive observational networks have been and are being developed on the Tibetan Plateau (Koike 2004; Y. Ma et al. 2008; Xu et al. 2008), which have advanced our understanding on the diurnal kB^{-1} behavior over this high-altitude alpine area (Ma et al. 2002, 2008b; Wang and Ma 2011; Yang et al. 2003, 2008). Even though these studies have resulted in numerous improvements in the parameterization of kB^{-1} , Chen et al. (2010) have recently shown that current land surface models (e.g., Noah LSM) still have difficulties with producing reliable daytime H and T_{sfc} simulations over arid and semiarid regions, such as the Tibetan Plateau. A successful modeling of the diurnal kB^{-1} variations is the key for improving the simulations of H and T_{sfc} as well as the overall model performance.

The potential of improving the daytime H and T_{sfc} simulations over arid regions through a revision of the kB^{-1} scheme has previously been investigated by Zeng et al. (2012) for the Noah and Community Land Model (CLM). The performance of Noah's kB^{-1} scheme was enhanced by only modifying the empirical coefficient of the original scheme by Zilitinkevich (1995). Similar modifications to the original kB^{-1} scheme of Noah were proposed by Chen and Zhang (2009) and Zheng et al. (2012). For instance, Chen and Zhang (2009) implemented the Zilitinkevich's empirical coefficient (C_{zil}) as a function of the canopy height, whereas Zheng et al. (2012) utilized the GVF for calculating kB^{-1} . An alternative way towards improving the kB^{-1} calculation within Noah is the implementation of the scheme specific for z_{oh} by Yang et al. (2008) as reported by Chen et al. (2010).

The performance of these three newly developed kB^{-1} schemes for the Noah LSM has so far not been evaluated for different seasons across the Tibetan Plateau. Only, Chen et al. (2010) have investigated modeling results obtained with the z_{oh} scheme by Yang et al. (2008) for two-month pre-monsoon episodes. Therefore, the performance of those kB^{-1} schemes is evaluated in this chapter for a Tibetan Plateau site in different seasons. A long-term dataset collected at the Maqu station (33.88°N, 102.15°E at an altitude of about 3430 m) from 20 May 2009 to 17 May 2010 is used for this analysis. The dataset includes eddy-covariance (EC) measurements and profile measurements of wind, air temperature and humidity. The bulk MOST formulation is used in combination with these micro-meteorological measurements to derive values for z_{0m} , z_{0h} and

kB^{-1} . Subsequently, these z_{0m} , z_{0h} and kB^{-1} values are utilized together with the H measurements to assess the performance of the various z_{0m} and z_{0h} or kB^{-1} schemes. Then, selected z_{0m} and z_{0h} schemes are implemented within the Noah LSM to evaluate their performance in simulating the surface energy balance and surface temperature. Finally, the impact of T_{sfc} calculation and energy-balance closure associated with measurement uncertainties on above assessment are discussed, and the selection of the appropriate z_{0h} scheme for applications is addressed.

4.2 Materials and methods

A detailed description of the Maqu observational dataset utilized for this investigation is available in Chapter 2 of this thesis. The data used in this investigation have been collected at the micro-meteorological observation system from 20 May 2009 to 17 May 2010. The episodes with snow on the ground are excluded by using only the data records for which the observed albedo attains the value of a snow free surface. The soil starts freezing around the beginning of November, while the frozen ground totally thawed around the beginning of May.

In the text below, several schemes of roughness lengths proposed for the Noah LSM are briefly introduced, and the methods to derive the values for z_{0m} , z_{0h} and kB^{-1} using the in-situ surface heat fluxes and profile data are described as well. Detailed descriptions of the bulk MOST equations and the Noah model physics associated with turbulent heat transfer can be found in Chapter 3 of this thesis (see Section 3.1).

4.2.1 Parameterization of roughness lengths

Four roughness length schemes that have previously been utilized within the Noah LSM (Chen and Zhang 2009; Chen et al. 1997; Chen et al. 2011; Zheng et al. 2012) are selected for this study, which are listed in Table 4.1. In the earlier version 2.7.1 of Noah (hereafter N2.7), the z_{0m} is defined as a function of land cover (specified as 0.035 m for grassland and 0.011 m for bare soil), and the Reynolds number (Re_*) dependent formulation of the kB^{-1} concept proposed by Zilitinkevich (1995) is implemented for the z_{0h} calculation (see also eqs. (3.28)-(3.29); Chen et al. 1997). In the latest version 3.4.1 of Noah (hereafter N3.4), seasonal values of z_{0m} are calculated based on the green vegetation fraction (GVF , see also eqs. (3.26)-(3.27)), and the Zilitinkevich's formulation is also adopted to calculate the z_{0h} . It should be noted that the Zilitinkevich's empirical coefficient (C_{zil}) is also taken as 0.1 by default in Noah 3.4.1, whereas the

formulation proposed by Chen and Zhang (2009) calculating C_{zil} as a function of canopy height via z_{0m} is implemented as an alternative option. The expression of Chen and Zhang (2009) is derived from 12 AmeriFlux data sets collected over a variety of land covers and climate regimes and is proven superior than the default C_{zil} constant, which is thus selected for the assessment. Similar modification has been proposed recently by Zheng et al. (2012) (hereafter Z12) to improve the cold bias in the daytime surface temperature (T_{sfc}) simulation over the arid western continental United States. Chen et al. (2010, 2011) reported on an alternative approach for improving the Noah's daytime T_{sfc} simulation through implementation of the specific scheme for z_{0h} proposed by Yang et al. (2008) (hereafter Y08).

Note that N2.7, N3.4 and Z12 have similar formulations for z_{0h} with different methods to specify C_{zil} . N2.7 utilizes a constant value ($C_{zil}=0.1$), N3.4 defines it based on z_{0m} ($C_{zil}=10^{-0.4z_{0m}/0.07}$), and Z12 calculates it based on GVF [$C_{zil}=(1-GVF)^2 \times 0.8$]. Besides, both N3.4 and Z12 calculate the z_{0m} using GVF , but different schemes are used: N3.4 interpolates the values of z_{0m} linearly between a specified minimum ($z_{0m,min}$, equal to bare soil z_{0m} when $GVF=0$) and maximum ($z_{0m,max}$, equal to fully vegetated z_{0m} when $GVF=1$) z_{0m} , while Z12 applies a quadric method to derive the effective momentum roughness length (z_{0m}) from the fully vegetated (z_{0v}) and bare soil (z_{0g}) to consider the convergence of z_{0m} in a model grid. The linear method in N3.4 and the quadric method in Z12 are similar as both obtain the GVF from satellite derived $NDVI$ data (Hong et al. 2009). The linear method tends to overestimate z_{0m} in sparse vegetated areas, while this overestimation can be minimized using the quadric method. The parameterization of Y08 is specific for the z_{0h} and does not depend on z_{0m} , which is a combination of friction velocity (u_*) and friction temperature (θ_*).

Table 4.1: Four parameterizations of roughness lengths (m) selected for this study *

Formulation	Reference/Source	Abbreviation
$z_{0m} = 0.035$ for grassland, and 0.011 for bare soil	Chen et al. (1997)	N2.7
$z_{0h} = z_{0m} \cdot \exp(-kC_{zil} \sqrt{\text{Re}_*}), C_{zil} = 0.1, \text{Re}_* = u_* \cdot z_{0m} / \nu$	/ Noah 2.7.1	
$z_{0m} = (1 - GVF_{norm}) \cdot z_{0m,\min} + GVF_{norm} \cdot z_{0m,\max}$	Chen and Zhang (2009)	N3.4
$z_{0h} = z_{0m} \cdot \exp(-kC_{zil} \sqrt{\text{Re}_*}), C_{zil} = 10^{-0.4z_{0m}/0.07}$	/ Noah 3.4.1	
$z_{0m} = \exp\{(1 - GVF)^2 \cdot \ln(z_{0g}) + [1 - (1 - GVF)^2] \cdot \ln(z_{0v})\}$	Zheng et al. (2012)	Z12
$z_{0h} = z_{0m} \cdot \exp(-kC_{zil} \sqrt{u_* \cdot z_{0g} / \nu}), C_{zil} = 0.8(1 - GVF)^2$		
$z_{0h} = (70\nu / u_*) \cdot \exp(-7.2u_*^{0.5} \theta_* ^{0.25}), \theta_* = (\theta_a u_*^2) / (kgL)$	Yang et al. (2008)	Y08

*The parameters in the formulations: k is the von Karman constant, GVF_{norm} is the normalized GVF, ν is the kinematic molecular viscosity, θ_a is the potential air temperature, g is the gravity acceleration, and L is the Obukhov length. Detailed descriptions of these parameters can be found in Chapter 3 (see Sections 3.1.1 and 3.1.6).

4.2.2 Estimation of roughness lengths

Two methods (Sun 1999; Yang et al. 2008) are used in this study for estimation of monthly z_{0m} values, from the profile measurements of wind (u), temperature (T_a) and humidity (RH) and single-level EC measurements of u , T_a , friction velocity (u_*) and sensible heat flux (H) collected at Maqu station. Following Sun (1999), the monthly z_{0m} is approximated from values derived from each 30-min observation interval with a linear least-square regression method (hereafter Sun99). The monthly z_{0m} is following Yang et al. (2008)

taken as the values associated with the highest occurrence within the histogram derived from the individual 30-min samples (hereafter Yang08). A detailed description of both methods is provided in Appendix A.1 of this thesis.

Given the obtained monthly z_{0m} values derived using method either by Yang08 or from Sun99, the z_{0h} or kB^{-1} is estimated through inversion of the bulk MOST equations (see eqs. (3.2)-(3.10)) using observed H (H_{obs}) for each 30-min observation interval by following: 1) assume $z_{0h} = z_{0m}$, 2) calculate H (H_{cal}) using eqs. (3.2)-(3.10), 3) adjust z_{0h} according to the difference in surface exchange coefficient for heat transfer (C_h) if $H_{cal} \neq H_{obs}$; 4) repeat step 2-3 until $H_{cal} = H_{obs}$; 5) calculate kB^{-1} as $kB^{-1} = \ln(z_{0m}/z_{0h})$. For the 5-level wind speed and air temperature profile measurements and 1-level EC measurements, kB^{-1} is calculated for each level and their average is used in the analysis.

Similarly, the kB^{-1} produced by the four z_{0h} schemes listed in Table 4.1 is calculated using the following steps: 1) assume $kB^{-1} = 0$, 2) derive the value of z_{0h} by $z_{0h} = z_{0m} \exp(kB^{-1})$, 3) use z_{0m} and z_{0h} to calculate u_* , θ_* and H_{cal} from eqs. (3.2)-(3.10), 4) use u_* and θ_* to calculate kB^{-1} from $kB^{-1} = \ln(z_{0m}/z_{0h})$ according to each of the four z_{0h} schemes; 5) repeat steps 2-4 until the cost function

$$J = \sum_{i=1}^6 (H_{cal,i} - H_{obs})^2 \text{ is minimized.}$$

4.2.3 Specific settings for the assessment

In order to assess the performance of the various roughness length schemes (shown in Table 4.1) for Maqu station in different seasons, three specific procedures are carried out step by step. Firstly, the monthly variations of z_{0m} and diurnal variations of z_{0h} are derived from the EC and profile measurements with the methods described in previous section (i.e., Section 4.2.2). Then these values are utilized to assess the skill of those z_{0h} and z_{0m} schemes in reproducing the observed z_{0h} and z_{0m} . Particularly, the comparison between the observed and the calculated kB^{-1} with the z_{0h} schemes is carried out for three periods: i) 15 December 2009 to 15 January 2010 (winter period) when soils are continuously frozen, ii) 8 April to 7 May 2010 (spring period) when soils are in transition from being frozen to thaw and iii) 1 to 30 September 2009 (monsoon period) when soils are completely thawed and vegetation is active.

Secondly, the bulk MOST equations (see eqs. (3.2)-(3.10)) are used to assess the performance of various roughness length schemes in estimating H . Observed air temperature and relative humidity at 2.35 m as well as air pressure from the Planetary Boundary Layer (PBL) tower, and wind speed at 3.2 m from

the EC system, as well as T_{sfc} derived from the observed longwave radiations are used within the bulk MOST calculations.

Finally, the selected z_{om} and z_{oh} schemes are implemented within the Noah LSM to evaluate the turbulent sensible (H) and latent (LE) heat flux as well as T_{sfc} simulations against measurements. This study presently employs version 3.4.1 of the Noah LSM (see Chapter 3), and the codes are revised to utilize the measured upward shortwave radiation. The model is forced by the meteorological measurements collected at the PBL tower, such as air temperature, relative humidity, wind speed, air pressure, downward and upward shortwave radiations, downward longwave radiation and precipitation. The vegetation type is prescribed as grassland at the Maqu station, and the soil type is set as silt loam based on Dente et al. (2012). The corresponding vegetation parameters (e.g., root depths) and soil hydraulic and thermal parameters are obtained from the default database of Noah. A monthly GVF database is used by Noah as default, which Gutman and Ignatov (1998) based on the 5 year (1985-1990) AVHRR $NDVI$ data. Jiang et al. (2009) pointed out, however, that the GVF climatology cannot capture the real-time vegetation status. Therefore, the GVF data for Maqu station in this study has been derived from 2009-2010 SPOT ten-daily synthesis $NDVI$ products by following:

$$GVF = \frac{NDVI - NDVI_{min}}{NDVI_{max} - NDVI_{min}} \quad (4.1)$$

where $NDVI_{min}$ is minimum $NDVI$ (or bare soil $NDVI$) and $NDVI_{max}$ is maximum $NDVI$ (or full canopy $NDVI$). The values of $NDVI_{min}$ and $NDVI_{max}$ are specified as 0.8 and 0.1 respectively. A detailed description of the $NDVI$ products and data-processing can be found in X. Chen et al. (2013).

4.3 Characteristic of roughness lengths

4.3.1 Momentum roughness length

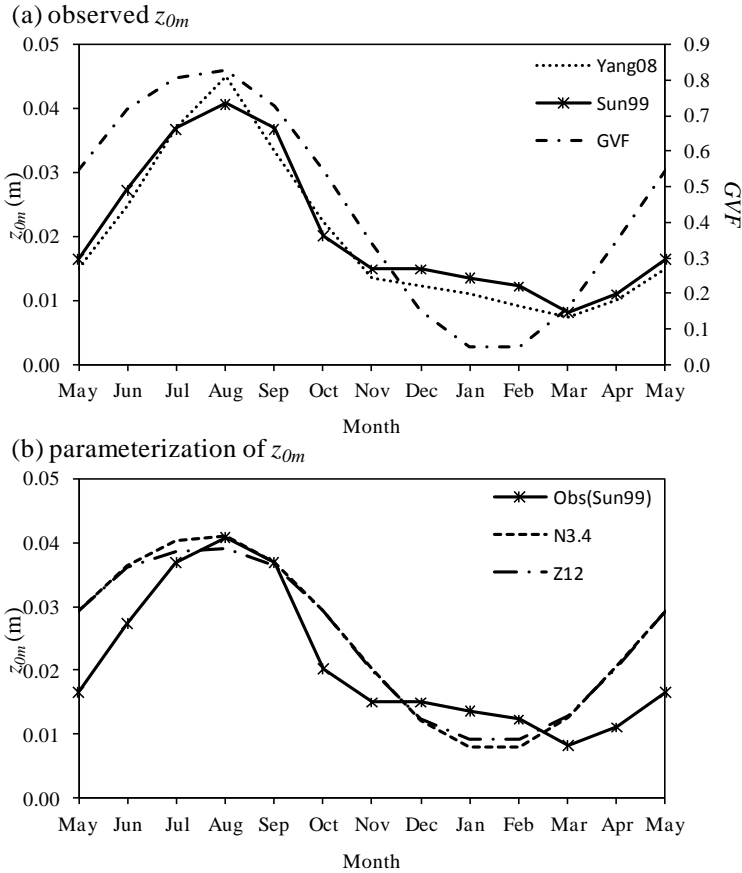


Figure 4.1: Comparison of the monthly variations of z_{0m} derived (a) using methods from Yang08 and Sun99, and (b) from observations (Sun99) and two z_{0m} schemes (N3.4 and Z12).

Figure 4.1a shows the monthly variations of z_{0m} obtained with methods from Yang08 and Sun99 respectively (see Section 4.2.2). It is noted that both methods produce similar monthly z_{0m} values and the order of magnitude varies from 0.007 to 0.045 m. The monthly z_{0m} increases from the pre-monsoon period (May to June) to the monsoon period (July to September) and reaches its peak in August, then drops from August to the cold season (November to April) achieving its minimum in March. The explanation for these seasonal variations can be that the surface is covered with sparse short grass over Maqu station

during the cold season, and it is partially covered with tall grass during the warm season (May to October). Since the z_{0m} is related to the surface conditions and canopy heights, the dynamics of GVF and canopy heights will change the values of z_{0m} as can be noted in Figure 4.1a. On the other hand, it is also well-known that the z_{0m} over smooth surfaces (e.g., plane and regular ice surface) is lower than bluff surfaces (e.g., grassland; Brutsaert 1982). Hence, it may also be expected that the z_{0m} is lower throughout winters because soil water is typically frozen during the cold season as noted in Figure 4.1a from November till April. It is, therefore, suggested to include the vegetation dynamics and consider soil water state in the parameterization of z_{0m} for seasonally frozen areas.

Figure 4.1a also shows that the derived value of z_{0m} for sparse short grass during the cold season (e.g., $z_{0m}=0.008$ m in March by Sun99) is comparable to the one prescribed in N2.7 for bare soil ($z_{0m}=0.011$ m in Table 4.1). The value for tall grass with dense GVF during the warm season (e.g., $z_{0m}=0.041$ m in August by Sun99) is somewhat higher than the one prescribed in N2.7 for grassland ($z_{0m}=0.035$ m). The values of z_{0m} calculated by N3.4 and Z12 z_{0m} schemes are shown in Figure 4.1b. For this study, the values for $z_{0m,\min}$ and $z_{0m,\max}$ of the N3.4 scheme are set to 0.008 m and 0.041 m respectively, and the values for z_{0g} and z_{0v} in Z12 are taken as 0.008 m and 0.041 m respectively. Figure 4.1b illustrates that both N3.4 and Z12 produce similar values and capture the trend of z_{0m} derived from the measurements (in this case following Sun99) reasonable well. Both schemes largely depend on the GVF dynamics. However, the linear method adopted in N3.4 produces higher z_{0m} for tall grass with dense GVF and lower z_{0m} for sparse short grass than the quadric method used in Z12.

4.3.2 Thermal roughness length or kB^{-1}

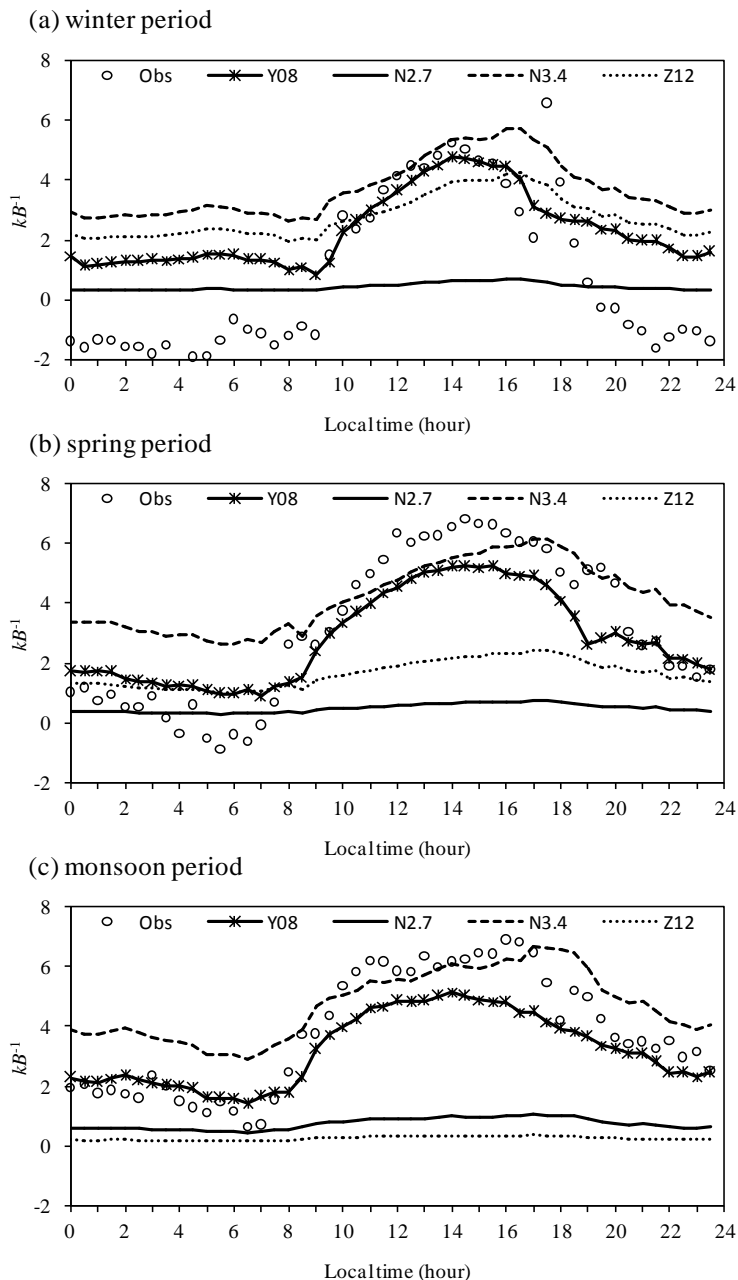


Figure 4.2: Comparison of the average composite diurnal variations between the observed kB^{-1} and four kB^{-1} schemes (Y08, N2.7, N3.4, and Z12) during the (a) winter, (b) spring, and (c) monsoon periods.

Figure 4.2 shows the average composite diurnal variations of observed kB^{-1} derived from the EC and profile measurements for Maqu station for three typical periods: a winter (15 December 2009 to 15 January 2010), a spring (8 April to 7 May 2010) and a monsoon period (1 to 30 September 2009). The observed kB^{-1} exhibits apparent diurnal variations for each period, and negative values of kB^{-1} occur during the night particularly in the winter period (Figure 4.2a). Verhoef et al. (1997) have also reported negative kB^{-1} values for a nearly aerodynamically smooth bare-soil surface. Ice exists when the ground surface is frozen during the winter period, and the surface during this period can be considered as aerodynamically smooth, which explains the negative kB^{-1} values. Yang et al. (2008) found that negative values of kB^{-1} are also often observed for aerodynamically rough surfaces, which may be attributed to heat transfer by inactive (nonlocal) eddies in the outer layer.

Figure 4.2 also compares the average composite diurnal variations of the observed kB^{-1} with the values calculated by four kB^{-1} schemes. It shows that the kB^{-1} schemes except N2.7 can reproduce the diurnal variations well during the winter period (Figure 4.2a). Both N3.4 and Z12 schemes produce comparable results, which indicate that the performance of N2.7 can be improved by increasing the value of C_{zil} . Similar results have also been reported by Zeng et al. (2012) for arid regions. They recommended $C_{zil}=0.9$. Both N3.4 and Y08 can capture the diurnal variations for the spring and monsoon periods (Figures 4.2b and 4.2c), whereas the variations produced by Z12 and N2.7 are very small. The reason for this is that the value of C_{zil} calculated by Z12 depends on the seasonally variable GVF , and the value of GVF during the spring ($GVF=0.35$ in April) or monsoon ($GVF=0.73$ in September) period is higher than the one during the winter period ($GVF<0.2$ between December and March). As such, the value of C_{zil} calculated by Z12 for the spring ($C_{zil}\approx 0.32$ in April) or monsoon ($C_{zil}\approx 0.06$ in September) period decreases sharply as compared to winter period ($C_{zil}\approx 0.72$ in January). N3.4 produces a comparable value of C_{zil} as Z12 for the winter period ($C_{zil}\approx 0.87$ when $z_{0m}=0.01$ m), but it tends to produce a higher value of C_{zil} for the spring and monsoon periods ($C_{zil}\approx 0.63$ when $z_{0m}=0.035$ m). This indicates that a relatively higher value of C_{zil} is recommended for the spring and monsoon periods when there is also a higher GVF .

Overall, Y08 and N3.4 perform better than other schemes, while Y08 produces a more distinct diurnal cycle and agrees better with the observed kB^{-1} , which is attributed to the use of the θ_* within the parameterization of z_{0h} (Yang et al. 2008). In addition, all the roughness length schemes tend to produce a better agreement with the observed kB^{-1} during the day than during the night.

4.4 Calculation of sensible heat flux based on MOST

4.4.1 Assessment of thermal roughness length schemes

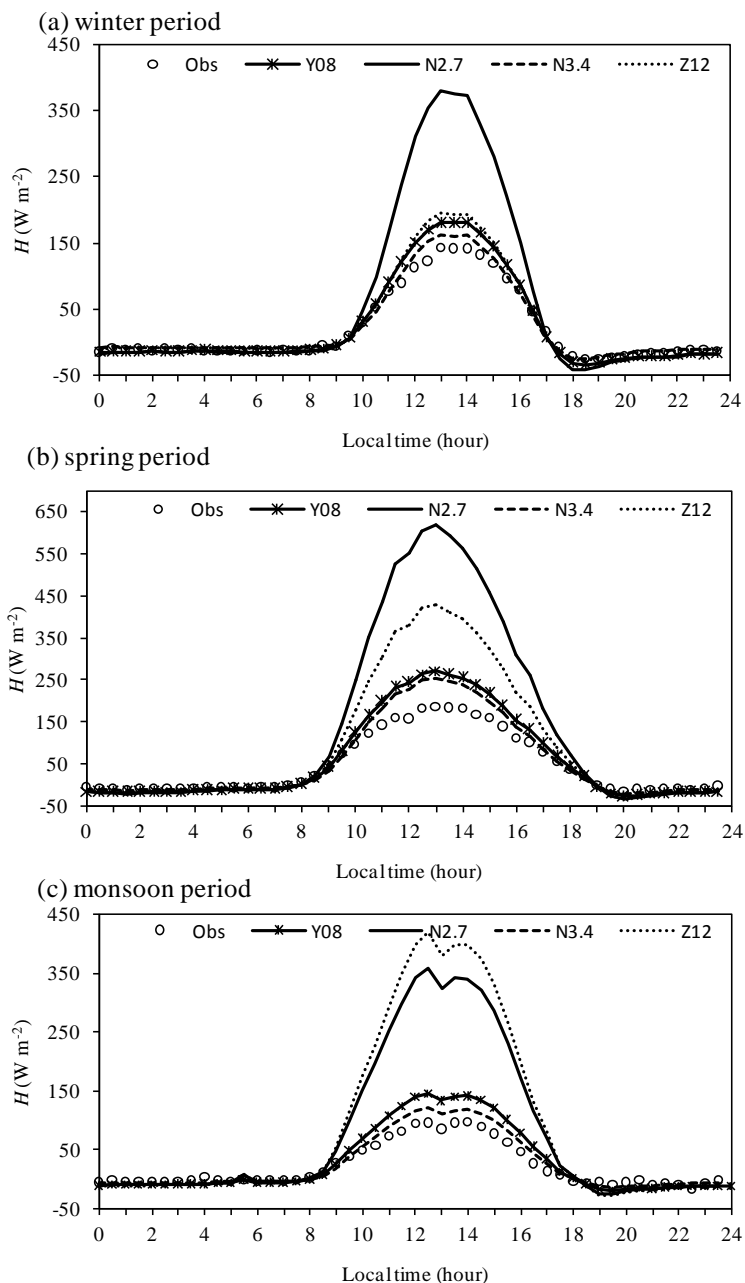


Figure 4.3: As in Figure 4.2, but for sensible heat flux (H).

Given the observed z_{0m} values (shown in Figure 4.1), the four z_{0h} schemes are utilized for estimating the sensible heat flux (H) from the bulk MOST equations (see eqs. (3.2)-(3.10)) with the measured surface temperature (T_{sfc}) as input. Figure 4.3 compares the average composite diurnal variations of the measured H and the calculations for the three periods. Overall, both N3.4 and Y08 schemes result in better agreements with the measured H than others during daytime. The poorer performance of N2.7 and Z12 schemes is caused by the much lower heat transfer resistances produced during the day due to the lower C_{zil} value, which is the key towards improving the H simulation.

Figure 4.3 shows further that the measured H is higher during the winter and spring periods (Figures 4.3a and 4.3b) than during the monsoon period (Figure 4.3c). The explanation for this seasonal variation is that the sensible heat flux is the dominant component of the surface energy budget before the onset of monsoon (about the end of May to the middle of June), because conditions (e.g., soil moisture and temperature) for the production of latent heat are not favorable during those periods. After the onset of monsoon, the temperature and the available soil moisture content doubles the latent heat production with respect to the sensible heat, while the net radiation remains at the same level due to more cloud cover.

Table 4.2: Determination coefficient (R^2), mean error (ME) and root mean square error (RMSE) computed between observed H ($W m^{-2}$) and simulations derived by four z_{0h} schemes for the three typical periods

z_{0h}	winter period			spring period			monsoon period		
	R^2	ME	RMS E	R^2	ME	RMS E	R^2	ME	RMSE
N2.7	0.90	38.4	95.7	0.93	65.24	141	0.91	54.7	123.1
N3.4	0.92	2.97	19.3	0.94	10.99	34.9	0.91	4.05	21.9
Z12	0.92	8.07	27.0	0.93	41.56	93.1	0.91	67.8	151.1
Y08	0.93	3.80	24.0	0.94	10.79	34.4	0.91	8.23	30.7

Table 4.2 provides the error statistics, such as coefficient of determination (R^2), mean error (ME) and root mean squared error (RMSE), computed between the observed and simulated H , which also indicates that N3.4 and Y08 perform better for all three periods, while Z12 performs better than N2.7 only during the winter period. Therefore, the simulation of H by the original Zilitinkevich's z_{0h} scheme implemented in N2.7 can be improved by all three

newly developed z_{0h} schemes (i.e., N3.4, Z12 and Y08) at least during the winter period. It should, however, be noted that for the spring and monsoon periods with higher GVF ($GVF > 0.35$), only N3.4 and Y08 produce better results than N2.7. The N3.4 and Y08 schemes will, therefore, be used for further analysis.

4.4.2 Assessment of momentum roughness length schemes

The monthly z_{0m} variations shown in Section 4.3.1 were attributed to vegetation dynamics and soil water state in seasonally frozen ground. Section 4.3.1 also showed that the current z_{0m} schemes (e.g., N3.4 and Z12 shown in Table 4.1) can reproduce comparable z_{0m} values and capture these z_{0m} dynamics. Therefore, the performance of three z_{0m} schemes in simulating H is assessed: N2.7, N3.4 and Z12. In N2.7, the values of z_{0m} are specified as 0.035 m for the warm season (May to October) and 0.011 m for the cold season (November to April), and the settings of N3.4 and Z12 were previously introduced in Section 4.3.1. N3.4 and Y08 z_{0h} schemes are combined with these three z_{0m} schemes to investigate the better combination of z_{0h} and z_{0m} parameterizations.

Table 4.3: Comparative statistics between observed H and simulations using three z_{0m} schemes for warm season and cold season respectively

z_{0m}	z_{0h}	warm season			cold season		
		R^2	ME ($W\ m^{-2}$)	RMSE ($W\ m^{-2}$)	R^2	ME ($W\ m^{-2}$)	RMSE ($W\ m^{-2}$)
N2.7	N3.4	0.89	4.92	32.8	0.92	8.23	38.9
	Y08	0.89	10.02	42.5	0.93	10.67	45.5
N3.4	N3.4	0.89	5.17	33.5	0.92	8.35	39.1
	Y08	0.89	10.17	42.9	0.93	11.27	43.4
Z12	N3.4	0.89	5.08	33.3	0.92	8.33	39.1
	Y08	0.89	10.11	42.8	0.93	11.40	47.6

Table 4.3 gives the error statistics (i.e., R^2 , ME and RMSE) between the observed and simulated H for the warm season (May to October) and cold season (November to April). Clearly, different z_{0m} schemes produce minor differences in simulating H , and the simulations are highly sensitive to the z_{0h} schemes and much less sensitive to the z_{0m} schemes.

In summary, the simulation of H is much more sensitive to the z_{0h} schemes than the z_{0m} schemes, and N3.4 and Y08 z_{0h} schemes perform better than other

schemes. Those newly developed z_{oh} schemes all provide better agreements with the measurements than the original N2.7 during the winter period with sparse GVF ($GVF < 0.2$ between December and March). However, only N3.4 and Y08 z_{oh} schemes perform better during the monsoon period with much higher GVF ($GVF > 0.70$ between June and September).

4.5 Implementation of Noah LSM

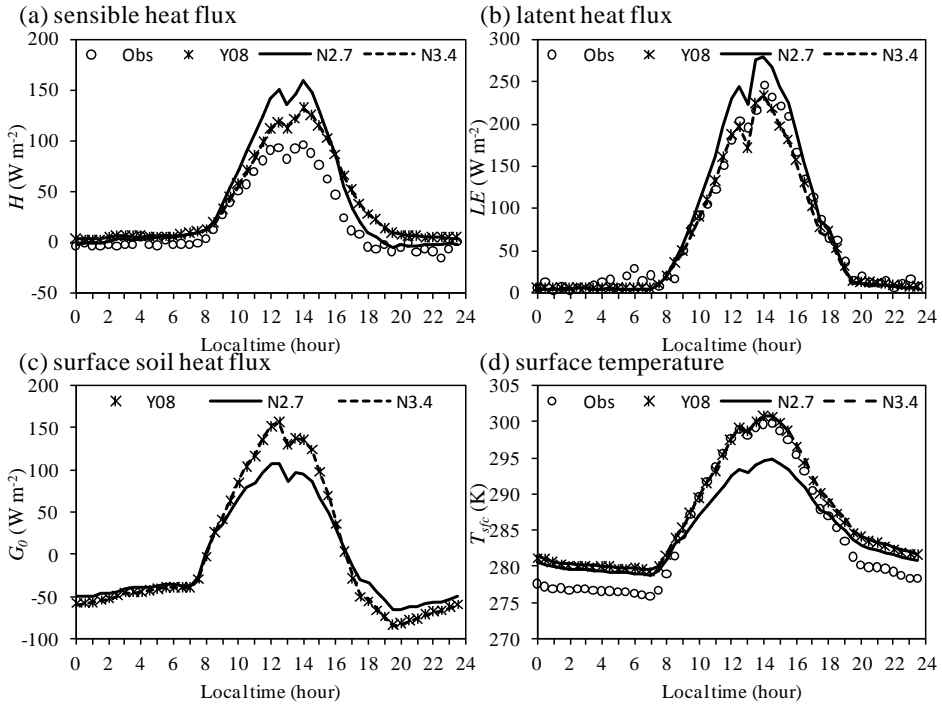


Figure 4.4: Comparison of the average composite diurnal variations during the monsoon period between observations and the simulations derived by the Noah LSM using three z_{oh} schemes (Y08, N2.7, and N3.4) of: (a) sensible heat flux, (b) latent heat flux, (c) surface soil heat flux, and (d) surface temperature.

As shown in Section 4.4, the simulation of H is much more sensitive to the choice of the z_{oh} scheme than z_{om} scheme, and N3.4 and Y08 z_{oh} schemes perform consistently better than other schemes. Therefore, both N3.4 and Y08 z_{oh} schemes are implemented within the Noah LSM to evaluate their performance in simulating the surface energy balance and soil temperature in comparison to the N2.7. The evaluation is carried out for the monsoon period (1 to 30 September 2009), and the codes of Noah 3.4.1 are further revised to utilize

the measured (liquid) soil moisture to prevent uncertainties associated with the soil water flow simulations from affecting the assessment.

Figure 4.4 compares the measured and simulated composite diurnal variations of heat fluxes and surface temperature (T_{sfc}) obtained using the three z_{oh} schemes. It shows that the original Zilitinkevich's z_{oh} scheme implemented in N2.7 strongly overestimates both measured turbulent sensible (H) and latent (LE) heat fluxes (Figures 4.4a and 4.4b), which leads to less energy available for heating the surface and transporting to the deeper soil layers (Figure 4.4c). As a consequence, the T_{sfc} (Figure 4.4d) is strongly underestimated. Such overestimation of H and LE by the original Zilitinkevich's z_{oh} scheme can be significantly improved by implementing the N3.4 or Y08 z_{oh} scheme. Indeed, more realistic heat flux and surface temperature simulations are produced with both schemes.

Figure 4.4 shows also that the major difference between the measurements and simulations occurs during daytime. Table 4.4 gives the error statistics between the measured heat fluxes (H and LE) and T_{sfc} and the Noah simulations during the daytime (0900-1800 local time). Clearly, the simulations with the original Zilitinkevich's z_{oh} scheme in N2.7 are significantly improved by implementing the N3.4 or Y08 z_{oh} scheme. The RMSE between measured and simulated H , LE and T_{sfc} are reduced respectively by about 28, 29 and 61 % using the N3.4 or Y08 z_{oh} scheme as compared to the N2.7, and the absolute ME are reduced by 29, 79, and 75 % respectively.

Table 4.4: Comparative statistics between observed and simulated daytime (0900-1800 LT) heat fluxes and surface temperature with Noah LSM obtained using three z_{oh} schemes for the monsoon period

z_{oh}	H ($W\ m^{-2}$)		LE ($W\ m^{-2}$)		T_{sfc} (K)	
	RMSE	ME	RMSE	ME	RMSE	ME
N2.7	51.96	35.69	56.43	23.91	4.18	-3.05
N3.4	37.27	25.08	39.61	-6.94	1.83	1.08
Y08	38.32	25.97	40.63	-4.90	1.62	0.76

4.6 Discussion

4.6.1 Ground surface temperature uncertainty and its impact

In Section 4.4, the bulk MOST equations (see eqs. (3.2)-(3.10) in Chapter 3) are used to assess the performance of various roughness length schemes in

estimating sensible heat flux (H), within which the ground surface temperature (T_{sfc}) is computed from measured longwave radiations (see eq. (2.1) in Chapter 2). Therefore, the uncertainty of ground-based longwave radiation measurements will affect the T_{sfc} and H estimates. The sensitivity of T_{sfc} and H to measurement uncertainties is tested by artificially adding 1, 2 and 4 % error to the longwave radiation during the daytime (0900-1800 local time), which corresponds to measurements with low, medium and high uncertainty according to Philipona et al. (2001) and Kohsiek et al. (2007).

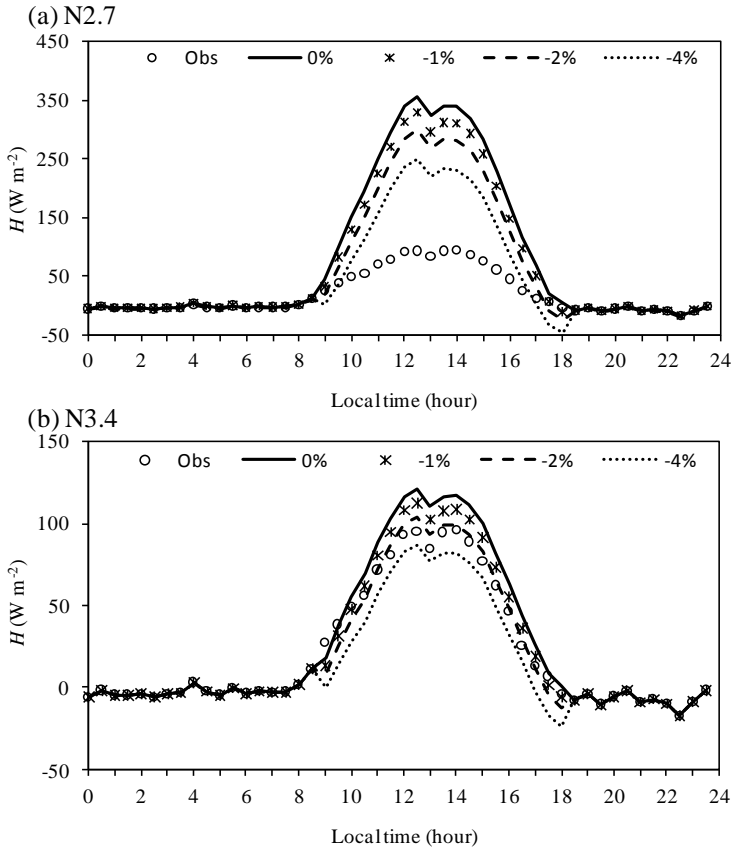


Figure 4.5: Average composite diurnal variations of sensible heat flux for the monsoon period from measurements and simulations using the MOST equations with (a) N2.7 and (b) N3.4 z_{oh} schemes with uncertainty levels imposed on longwave radiations of 0, -1, -2 and -4 %.

The monsoon period (1 to 30 September 2009) is taken as an example for the sensitivity test and the three error levels results in a T_{sfc} uncertainty of 0.29 K, 0.59 K and 1.18 K during the daytime, respectively. The bulk MOST equations are then used in combination with these T_{sfc} values to calculate H . Figure 4.5 shows the average composite diurnal variations of the measured H and the calculations using N2.7 and N3.4 z_{oh} schemes. The plot illustrates that 4 % decrease in the longwave radiation reduces the H calculated at midday with N2.7 and N3.4 by 100 and 30 W m^{-2} , respectively. Nevertheless, the N2.7 computed H severely overestimates measurements (Figure 4.5a), while the measurements fall within the ensemble of N3.4 H computations (Figure 4.5b). This is consistent with those findings in Section 4.4.

4.6.2 Energy-balance closure and its impact

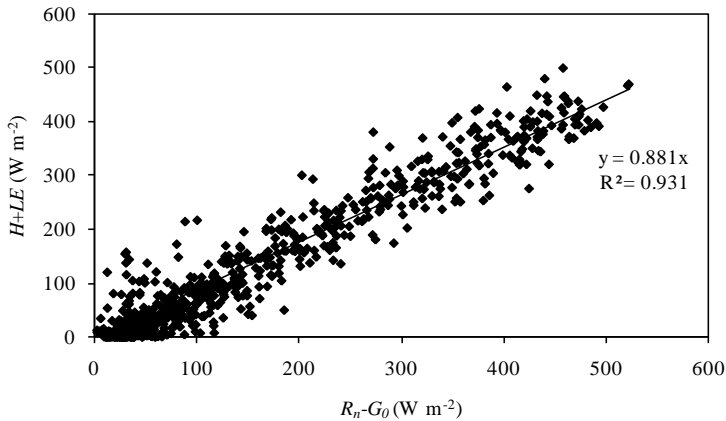


Figure 4.6: A plot of the quantity $H+LE$ versus R_n-G_0 showing energy balance closure of the surface fluxes over Maqu station during the monsoon period.

A well-known problem with surface heat flux measurements is the energy-balance closure (Foken 2008; Massman and Lee 2002; Wilson et al. 2002), which is particularly noticeable over the Tibetan Plateau (Tanaka et al. 2003; K. Yang et al. 2004). That is, the available energy, defined as the sum of net radiation (R_n) and ground heat flux (G_0), is larger than the sum of turbulent fluxes of sensible (H) and latent (LE) heat. In most of the surface heat flux experiments, the error in the energy budget is less than 20 % (Foken 2008). Figure 4.6 shows the sum of turbulent heat fluxes plotted against the available energy for part of the monsoon (1 to 30 September 2009), where G_0 is

calculated with the Noah LSM using N3.4 z_{0h} scheme. The closure ratio is high with a value of around 0.88 as shown in Figure 4.6.

Resolving the energy-balance closure issue is beyond the scope of this study, and a detailed review of this problem can be found in Twine et al. (2000) and Foken (2008). However, the use of surface flux data to validate the land surface model requires that conservation of energy is satisfied, and the measured energy budget should be closed by some method (Twine et al. 2000). Twine et al. (2000) suggested that the closure can be most reasonably forced by assuming that the measured available energy ($R_n - G_0$) is representative of the area, and thus the measured turbulent fluxes ($H + LE$) should be adjusted. The ‘Bowen-ratio closure’ method is used in this study, which assumes that the Bowen-ratio is correctly measured by the EC system, so that the individual value of H or LE can be adjusted (Twine et al. 2000):

$$H_{cor} = H + res \times \frac{H}{H + LE} \quad (4.2)$$

$$LE_{cor} = LE + res \times \frac{LE}{H + LE} \quad (4.3)$$

$$res = (R_n - G_0) - (H + LE) \quad (4.4)$$

To test the impact of the closure of the energy budget on the aforementioned assessment of roughness length schemes, the corrected sensible heat flux (H_{cor}) and latent heat flux (LE_{cor}) are used in combination with the Noah LSM and the other micro-meteorological measurements to evaluate the impact of measurement uncertainty on the assessment of various z_{0h} or kB^{-1} schemes. Figure 4.7a shows the average composite diurnal variations of observed kB^{-1} derived from the original and corrected sensible heat flux, while the values calculated by the four kB^{-1} schemes with H_{cor} are also shown. Figures 4.7b and 4.7c compare the simulated H and LE by Noah LSM using the four z_{0h} schemes with the original and corrected turbulent heat flux observations. Consistent with the previous findings, N3.4 and Y08 agree better with the corrected kB^{-1} (Figure 4.7a) and H_{cor} observations (Figure 4.7b) than N2.7 and Z12. However, it can be found that N3.4 and Y08 underestimate LE and perform poorer than N2.7 and Z12 when compared with LE_{cor} (Figure 4.7c).

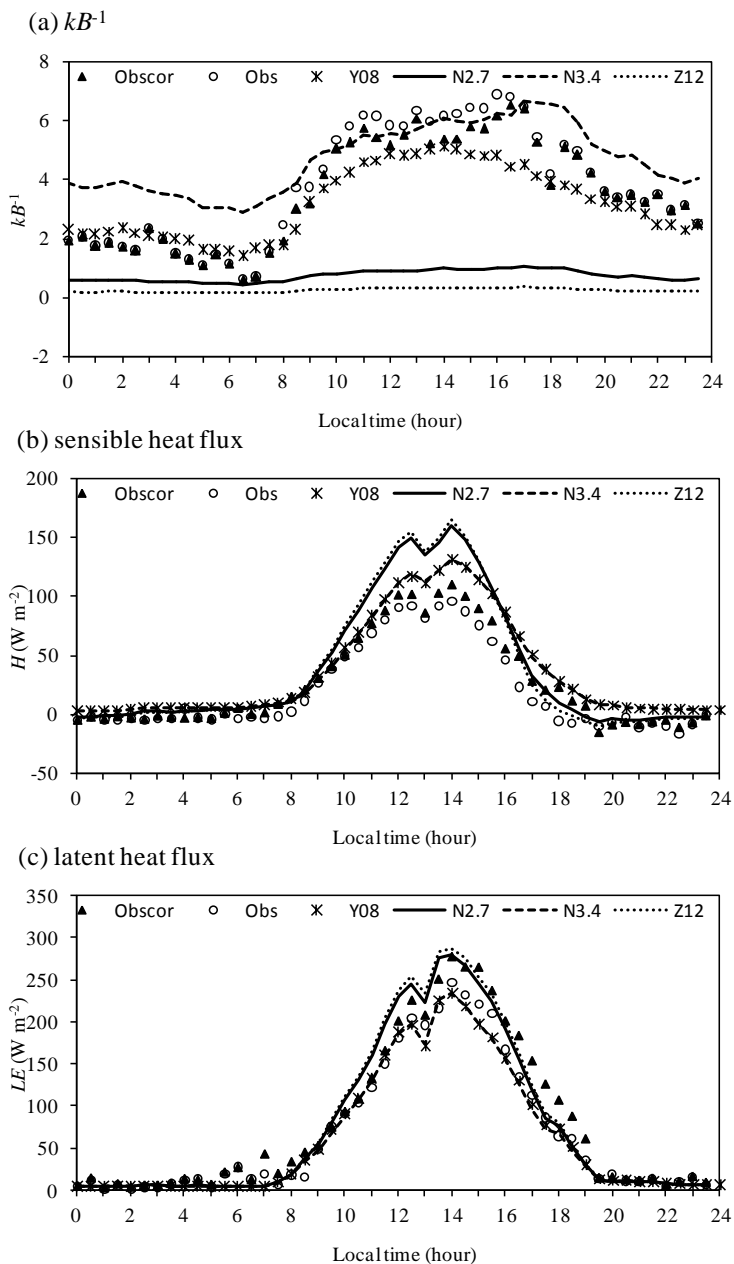


Figure 4.7: Comparison of the average composite diurnal variations of (a) kB^{-1} , (b) sensible heat flux and (c) latent heat flux between the original observations (obs), corrected observations (obscor), and the simulations derived from the corrected observations using four z_{0h} schemes (Y08, N2.7, N3.4, and Z12) during the monsoon period.

Although the comparison with LE_{cor} suggests that N2.7 and Z12 perform better than N3.4 and Y08, it should be noted that N2.7 and Z12 more severely overestimate the H_{cor} (Figure 4.7b) and underestimate the T_{sfc} (Figure 4.4d). The LE_{cor} underestimation by N3.4 and Y08 can be explained by the vegetation parameters prescribed in the Noah LSM. Indeed, van der Velde et al. (2009) have shown that, for Naqu station on the central Tibetan Plateau, a LE underestimation can be mitigated via calibration of the minimum stomatal resistance and the optimum temperature for transpiration. However, the objective of this study is to analyze the impact of roughness length schemes in simulating heat fluxes and not to address the problem of LE simulation in detail. As such, it can be concluded that the assessments related to kB^{-1} , H and surface temperature in previous sections are still valid if the measured energy budget is forced to be closed.

4.6.3 Choice of z_{0h} scheme

As seen in the previous sections, diurnal variations of z_{0h} are observed over Maqu station in different seasons, and a successful modeling of the variations is important for reliable H and T_{sfc} simulations as well as the overall model performance. The original Zilitinkevich's z_{0h} scheme in the Noah LSM (N2.7) cannot reproduce these diurnal variations, which can be enhanced by modifying the empirical coefficient C_{zil} . Zheng et al. (2012) and Zeng et al. (2012) suggested to use a range of values around 0.9 for C_{zil} together with explicit consideration of the GVF (Z12). This modification performs satisfactorily over the surface covered with sparse GVF , but it is inadequate for surfaces covered with dense GVF . Alternatively, the vegetation-type dependent formulation for C_{zil} from Chen and Zhang (2009) calculates C_{zil} as a function of the canopy height or z_{0m} (N3.4). This scheme performs consistently well for the surface with different GVF values in different seasons in this study, which has also been demonstrated with AmeriFlux data from a wide range of land covers and climate regimes (Chen and Zhang, 2009).

The z_{0h} scheme of Yang et al. (2008, Y08) is not associated with a specific z_{0m} scheme and also performs consistently well in the aforementioned assessment under different surface conditions. Chen et al. (2010, 2011) have found similar results over low vegetation and bare surfaces (e.g., alpine steppe, grassland and deserts), but they also reported on a poor performance over densely vegetated surfaces (e.g., forest and shrubland). As such, Zeng et al. (2012) argued that it is unclear how this scheme should be used over grid cells with different GVF values. Chen et al. (2011) suggested to resolve this issue via

combination of the schemes for bare soils and vegetated surfaces by taking their areal fraction into consideration, such as the kB^{-1} scheme implemented in the Surface Energy Balance System (SEBS, Su 2002). Recently, X. Chen et al. (2013) have replaced the soil part of the kB^{-1} scheme in SEBS with the z_{0h} scheme of Yang et al. (2008). The new scheme gave better performance than the original one over the Tibetan Plateau. However, additional validation is needed over other regions before it can be applied globally.

4.7 Conclusions

In this study, the performance of various recently developed parameterizations of roughness lengths for the Noah land surface model, as well as their effectiveness in simulating the surface heat flux transfer and land surface temperature (T_{sfc}) is investigated for different seasons in the source region of the Yellow River (SRYR) on the Tibetan Plateau. The major findings are as follows:

1) Monthly variations of momentum roughness length (z_{0m}) are found, which can be attributed to vegetation dynamics as well as to freeze-thaw processes, and current z_{0m} schemes can reproduce the observed z_{0m} and sensible heat flux (H) satisfactorily.

2) Diurnal variations of thermal roughness length (z_{0h}) are found for surfaces covered with different green vegetation fractions ($GVPs$) in different seasons, and Noah's original z_{0h} scheme by Zilitinkevich (1995) cannot reproduce the diurnal variations.

3) The simulation of H is much more sensitive to the z_{0h} scheme than the z_{0m} scheme, and the performance of Noah's original z_{0h} scheme in reproducing the diurnal variations of observed z_{0h} and H can be enhanced by modifying Zilitinkevich's empirical coefficient (C_{zil}). For instance, C_{zil} is related to the canopy height or z_{0m} by Chen and Zhang (2009), and it is calculated based on the GVP by Zheng et al. (2012). An alternative way is to use the z_{0h} scheme by Yang et al. (2008).

4) These newly developed z_{0h} schemes all produce better agreements with the measurements than the original one at least over the surfaces with sparse vegetation during the winter period. However, it should be noted that for the surfaces with dense vegetation during the spring and monsoon periods, not all newly developed schemes perform consistently better than the original one.

5) The Noah land surface model originally using the Zilitinkevich's z_{0h} scheme significantly overestimates H and LE , and underestimates T_{sfc} , and the

biases can be improved by about 29, 79, and 75 % respectively through implementing the most promising parameterization of roughness lengths.

Although the energy-balance closure issue of surface flux measurements has not been resolved in this study, it is shown that the above findings related to kB^{-1} , H and surface temperature are still valid if the measured energy budget is forced to be closed with the ‘Bowen-ratio closure’ method as in Twine et al. (2000). The z_{oh} scheme proposed by Chen and Zhang (2009) is suggested for further applications, due to its consistent performance over various surface conditions and in different seasons, that is, land cover and climate regimes. Another potential way is to integrate the z_{oh} scheme by Yang et al. (2008) for bare surfaces, into an existing kB^{-1} ($kB^{-1}=\ln(z_{om}/z_{oh})$) scheme that combines the schemes for bare soils and vegetated surfaces by taking their areal fractions into consideration, such as the work by X. Chen et al. (2013).

Chapter 5 Augmentations to the turbulent and soil heat transport simulation*

5.1 Introduction

Exchanges of energy and mass at the land-atmosphere interface play an important role in weather and climate dynamics. Climatic studies have demonstrated that an accurate quantification of these exchanges by atmospheric general circulation models (AGCMs) is crucial to arrive at the bottom boundary states needed for reliable weather forecast across various time scales (e.g., Beljaars and Holtslag 1991; Koster et al. 2004; Seneviratne et al. 2006). The soil temperature directly affects exchange of energy near the land surface as the upward longwave radiation, sensible and ground heat fluxes depend on it (e.g., Godfrey and Stensrud 2008; Mahanama et al. 2008). Although significant progress has been made by the land surface community to improve the modeling of surface heat fluxes and soil temperature (e.g., Koster et al. 2006; Niu et al. 2011; Sellers et al. 1997), there is still a great challenge to find ways to further reduce uncertainties and strive for consistency between model results and observations (Decker et al. 2011; Dirmeyer et al. 2006; Jiménez et al. 2011; Xia et al. 2012a).

Land-atmosphere exchanges on the Tibetan Plateau exert a profound impact on the atmospheric circulation in the Northern Hemisphere and specifically the evolution of the Asian monsoon (Sato and Kimura 2007; Wu and Zhang 1998; Zhou et al. 2009). Various field campaigns and monitoring programs have been conducted in the past (e.g., CAMP-Tibet; Koike 2004) and are ongoing (e.g., Tibet-Obs; Su et al. 2011) on the Tibetan Plateau, which have advanced our understanding of the prevailing hydro-meteorological processes in this high-altitude alpine region and resulted in numerous improvements in modeling the energy transport through the soil column as well as between the land and atmosphere. For instance, previous studies have found that i) the daytime land surface temperature (T_{sfc}) and sensible heat flux (H) are respectively underestimated and overestimated by model simulations (e.g., Chen et al. 2011;

***This chapter is based on the paper:** Zheng, D., R. van der Velde, Z. Su, X. Wang, J. Wen, M. J. Booi, A. Y. Hoekstra, and Y. Chen, 2015: Augmentations to the Noah model physics for application to the Yellow River source area: Part II. Turbulent heat fluxes and soil heat transport. *Journal of Hydrometeorology*, doi: 10.1175/JHM-D-14-0199.1.

Zheng et al. 2014), ii) the nighttime T_{sfc} simulation is unrealistic under stable atmospheric stratification condition (e.g., Zeng et al. 2012), and iii) the simulated heat transfer through the soil column is too weak to be able to reproduce the temperature variability measured in the deep soil, and the partitioning of the sensible and latent heat (LE) fluxes is biased (van der Velde et al. 2009).

A possible solution from these previous studies for amelioration of the daytime T_{sfc} and H simulations is to improve the parameterization of the diurnally varying roughness length for heat transport (z_{oh}), which has notably little impact on the nighttime T_{sfc} simulation. Zeng et al. (2012) suggested to improve the nighttime T_{sfc} simulation by constraining the ground heat flux (G_0) as the sensible and ground heat fluxes are complementary over bare soil, but one can question its validity for vegetation sites. van der Velde et al. (2009) showed that the simulation of turbulent heat fluxes and soil heat flow can be improved by making a distinction between the soil thermal properties of the upper and deep soil layers and by calibrating the soil and vegetation parameters. However, they arrived at unrealistically high values for the volumetric quartz fraction for the soil matrix to increase the heat conductance through the soil column. This is inconsistent with the findings of Yang et al. (2005) that the existence of dense vegetation roots and abundance of organic matter in the topsoil may significantly reduce thermal conductivity. Although Chen et al. (2012) have started to investigate the stratification of soil thermal properties induced by organic matter, the effects of the vertical heterogeneity on simulating heat fluxes and soil temperature profiles remain unknown.

Therefore, this study seeks to further improve a state-of-the-art Noah land surface model (LSM, Ek et al. 2003) in its ability to reproduce turbulent heat fluxes and soil temperature profiles measured in the high-elevation Source Region of the Yellow River (SRYR) on the Tibetan Plateau. A comprehensive dataset that includes in-situ micro-meteorological and soil moisture/temperature profile measurements, as well as soil properties characterized in the laboratory, is utilized here to assess the suitability of default model parameterizations and model augmentations. Four augmentations are made: i) the muting effect of vegetation on the heat conductivity (κ_h) is removed for heat transport from the first soil layer towards the second layer, ii) the exponential decay factor (β_{veg}) imposed on κ_h is calculated using the ratio of the leaf area index (LAI) over the green vegetation fraction (GVF), iii) Zilitinkevich's empirical coefficient (C_{zil}) for the turbulent heat transport is computed as a function of the momentum

roughness length (z_{0m}), and iv) the impact of organic matter is considered in the parameterization of the thermal heat properties.

This Chapter is outlined as follows: Section 5.2 introduces the in-situ dataset and describes the augmentations made to the Noah model structure aimed at improving the turbulent and soil heat transport processes. Section 5.3 presents the comparison of laboratory soil thermal property measurements with estimates computed using the newly developed parameterization that accommodates for the effect of organic matter. Section 5.4 reports on the performance of Noah in simulating turbulent heat fluxes and soil temperature in its default configuration as well as with augmentations. Section 5.5 provides a discussion on the simulation of nighttime T_{sfc} , presents Noah simulations whereby both soil moisture and heat flow processes are considered dynamically, and reports on the model performance in case when adopting very high organic matter contents. Finally, in Section 5.6 conclusions are drawn.

5.2 Materials and methods

A detailed description of the Maqu observational dataset utilized for this investigation is available in Chapter 2 of this thesis. Two soil moisture and soil temperature (SMST) monitoring stations (CST01 and NST01) are situated in the vicinity of the Maqu micro-meteorological observing system and are used for the presented analyses. The time period under investigation covers the majority of the monsoon season starting on 8 June 2010 and ending 30 September 2010. This episode is selected to avoid the impact of the cold season (e.g., snowpack and frozen soil) on the assessment of Noah's turbulent and soil heat transport model physics.

In the text below, the augmentations made to the Noah model physics aimed at improving the turbulent and soil heat transport processes are introduced. Detailed descriptions of the default Noah model physics associated with turbulent heat transfer and soil heat flow can be found in Chapter 3 of this thesis (see Section 3.1). Unless stated otherwise, a modified version of the default model is utilized here that is capable of ingesting the measured upward shortwave radiation and soil moisture to avoid that those uncertainties affect the performance in simulating the turbulent heat fluxes and soil heat transport as in Chapter 4 of this thesis (Zheng et al. 2014).

5.2.1 Vegetation effect on heat transport through soil

Recently, van der Velde et al. (2009), Rosero et al. (2010), and Niu et al. (2011) have reported on the underestimation of the heat conductance through

the soil column using the Noah LSM for vegetation areas. Rosero et al. (2010) pointed out that the value for the exponential decay factor (β_{veg} , see eq. (3.24)) may be too high, which unrealistically reduces the values for surface (κ_{h0}) and first soil layer (κ_{h1}) heat conductivities as well as the simulation of G_0 and the heat transport from/towards the second soil layer. The G_0 calculations can be improved by lowering the β_{veg} from 2.0 to 1.0 for grassland as Rosero et al. (2010) suggested, but this does not resolve the poor heat conductance towards the deep soil. In fact, the impact of vegetation on the heat conductance from the first to the second soil layer is questionable. It is, therefore, suggested to parameterize κ_{h0} and κ_{h1} independent from each other whereby the exponential decay of heat conductivity (κ_h) as a function of the GVF is only imposed on κ_{h0} as given in eq. (3.24) whereas it is ignored for κ_{h1} by changing eq. (3.25) as:

$$\kappa_{hi} = \kappa_h(\theta_i) \quad (5.1)$$

where i is the soil layer, θ is the soil moisture content ($\text{m}^3 \text{m}^{-3}$), κ_{hi} is the heat conductivity of each soil layer adopted by heat diffusion equation (see eq. (3.16)), and $\kappa_h(\theta_i)$ can be calculated using eq. (3.18).

The investigation by Rosero et al. (2010) indicates that a lower value for β_{veg} is needed. Other LSMs reduce the surface heat flux, instead of the heat conductivity, as a function of the vegetation cover. Early versions of the Variable Infiltration Capacity (VIC) model (Liang et al. 1999; Peters-Lidard et al. 1997) adopted for instance:

$$G_0 = G_{0,bs} \exp(-0.5LAI) \quad (5.2)$$

where $G_{0,bs}$ is the surface heat flux under bare soil (W m^{-2}) and LAI is the leaf area index ($\text{m}^2 \text{m}^{-2}$). From this the following expression for β_{veg} can be derived through combination with eqs. (3.13) and (3.24):

$$\beta_{veg} \approx \begin{cases} 0.5LAI/GVF, & GVF > 0 \\ 0 & , GVF = 0 \end{cases} \quad (5.3)$$

The GVF and LAI are here deduced from the 10 daily synthesis $NDVI$ (Normalized Difference Vegetation Index) product from the Satellite Pour l'Observation de la Terre (SPOT) observations as given in Zheng et al. (2014) and X. Chen et al. (2013).

5.2.2 C_{zil} parameterization

The surface exchange coefficient for heat (C_h) is another source of uncertainty that can be responsible for the overestimation of the sensible heat flux (H) and underestimation of surface temperature (T_{sfc}) during daytime by the

Noah LSM as has been reported in Chen et al. (2011), Niu et al. (2011) and Zeng et al. (2012). The most practical approach towards resolving this issue without violating the integrity of the model structure is through improvement of the kB^{-1} parameterization.

Both Zeng et al. (2012) and Zheng et al. (2014) recognized that this can be accomplished through a better quantification of the empirical C_{zil} parameter. Zheng et al. (2014) evaluated all kB^{-1} parameterizations developed for the Noah LSM and found that the best performance was achieved with the formulation proposed by Chen and Zhang (2009) , which can be expressed by:

$$C_{zil} = 10^{-0.4hc} \quad (5.4)$$

where h_c is the canopy height (m). This expression is implemented as an option in version 3.4.1 of the Noah LSM, but has not yet been taken up in the default model despite promising results. Further, it should be noted that within the Noah version 3.4.1 the canopy height is related to the z_{0m} by assuming z_{0m} is 7 % of the canopy height (Mölder and Lindroth 1999), which can be expressed as:

$$h_c = z_{0m}/0.07 \quad (5.5)$$

5.2.3 Organic matter effect on soil thermal parameterization

As described in Section 3.1.5 of Chapter 3, both the soil heat capacity (C_s) and conductivity (κ_h) depend on constituents of the soil matrix and, thus, on organic matter as well. In the default configuration, the Noah LSM does not accommodate the effect of organic matter on the soil thermal properties. However, eq. (3.17) can fairly easy be modified to include the volumetric fraction of solid organic matter ($f_{s,soc}$) according to the concept proposed by de Vries (1963) as follows:

$$C_s = \theta C_w + (\theta_s - \theta) C_{air} + (1 - \theta_s) \cdot f_{s,soc} \cdot C_{soc} + (1 - \theta_s) \cdot (1 - f_{s,soc}) \cdot C_{min} \quad (5.6)$$

$$f_{s,soc} = \frac{m_{soc} \rho_{s,min}}{m_{soc} \rho_{s,min} + (1 - m_{soc}) \rho_{s,soc}} \quad (5.7)$$

where θ_s is the porosity ($m^3 m^{-3}$), m_{soc} is the mass fraction of the soil organic matter ($kg kg^{-1}$), $\rho_{s,min}$ is the particle density of the mineral soil fraction (taken as $2700 kg m^{-3}$), $\rho_{s,soc}$ is the particle density of the soil organic matter (taken as $1300 kg m^{-3}$), C represents the heat capacity ($J m^{-3} K^{-1}$), and the subscripts ‘w’, ‘min’, ‘soc’, and ‘air’ refer to water, soil mineral matter, soil organic matter and air. Here, C_w , C_{min} , C_{soc} and C_{air} are taken as 4.2×10^6 , 2.0×10^6 , 2.5×10^6 and $1005 J m^{-3} K^{-1}$, respectively.

Further, Johansen (1975) pointed out that the bulk density of a dry soil is a major factor in defining the soil heat conductivity of a dry soil (κ_{dry}), while the soil texture has little effect on the conductivity. In other words, the semi-empirical equation (see eq. (3.20)) can be directly utilized to estimate the κ_{dry} , but the formulation for the bulk density of dry soil (ρ_b , see eq. (3.21)) needs to be modified to account for the impact of organic matter on the bulk density. Hence, the formulations for the calculation of κ_{dry} are now as:

$$\kappa_{dry} = \frac{0.135\rho_b + 64.7}{2700 - 0.947\rho_b} \quad (5.8)$$

$$\rho_b = \frac{\rho_{b,min}\rho_{b,soc}}{m_{soc}\rho_{b,min} + (1 - m_{soc})\rho_{b,soc}} \quad (5.9)$$

where $\rho_{b,min}$ and $\rho_{b,soc}$ are the bulk densities (kg m^{-3}) of the mineral soil fraction and soil organic matter, respectively. Additional information about the eq. (5.9) can be found in Chapter 6 of this thesis (see eq. (6.2)).

On the other hand, Johansen (1975) found that under saturated conditions the bulk density has little impact on the heat conductivity (κ_{sat}), whereas differences in soil composition become increasingly important for the magnitude of the conductivity. The effect of organic matter on κ_{sat} via κ_{soil} is accommodated by modifying its parameterization as follows:

$$\kappa_{sat} = \kappa_{soil}^{1-\theta_s} \kappa_w^{\theta_s} \quad (5.10)$$

$$\kappa_{soil} = \kappa_{soc}^{fs,soc} \kappa_{qtz}^{qtz \cdot (1-fs,soc)} \kappa_o^{(1-qtz) \cdot (1-fs,soc)} \quad (5.11)$$

where κ represents the heat conductivity ($\text{W m}^{-1} \text{K}^{-1}$), and the subscripts ‘w’, ‘soil’, ‘soc’, ‘qtz’, and ‘o’ refer to water, solid soil, soil organic matter, soil quartz content and other remaining soil content. Here, κ_w , κ_{soc} , κ_{qtz} and κ_o are taken as 0.57, 0.25, 7.7 and 2.0 $\text{W m}^{-1} \text{K}^{-1}$, respectively according to Peters-Lidard et al. (1998) and Lawrence and Slater (2008).

The effect of organic matter on κ_h is directly taken into consideration in the computations (see eqs. (3.18)-(3.19)) once the κ_{dry} and κ_{sat} are estimated using the updated bulk density and κ_{soil} formulations, respectively. That is:

$$\kappa_h(\theta) = K_e(\kappa_{sat} - \kappa_{dry}) + \kappa_{dry} \quad (5.12)$$

where K_e is the Kersten (1949) number representing the degree of saturation and is defined by:

$$K_e = \begin{cases} \log_{10}(\theta/\theta_s) + 1.0, & \text{for } \theta/\theta_s > 0.1 \\ 0.0, & \text{for } \theta/\theta_s \leq 0.1 \end{cases} \quad (5.13)$$

It should, however, be noted that the Noah simulated soil thermal properties are also affected by the soil organic matter via its impact on the hydraulic properties that regulate the soil moisture dynamics as well as the porosity. The latter is discussed in Chapter 6 of this thesis.

5.3 Estimation of soil heat conductivity

In this section the performance of Noah's default κ_h parameterization (see eqs. (3.18)-(3.23), hereafter 'J75') and the modified formulation (eqs. (5.8)-(5.13), hereafter 'Z14') that takes soil organic matter into account is evaluated using the laboratory measured soil properties of samples collected at the high-elevation SRYR. Soil samples were collected at two sites near the Maqu micro-meteorological station with relatively low organic content in the top soil layer (< 3 %, see Table 2.2 in Chapter 2 of this thesis), as well as two sites located in a wetland environment with abundant organic content (> 15 % near the surface). Detailed descriptions of the soil sampling and laboratory measurements can be found in Section 2.2.2 of this thesis (see Chapter 2).

Figure 5.1 shows the calculated Kersten number (K_e) and κ_h against values derived from the laboratory measurements of all the soil samples using the KD2 Thermal Properties Analyzer (Decagon Devices Inc.). The measured K_e is derived through inversion of eq. (5.12) using the heat conductivities measured over the complete soil moisture range from dry to fully saturated, which provides values for the κ_h , κ_{dry} and κ_{sat} . Figure 5.1a shows a plot with the measured K_e versus estimates computed with eq. (5.13). Both the slope of the fitted linear function (close to unity, i.e., 1.043) and the low scatter among data points (R^2 , coefficient of determination, 0.879) indicate that the K_e calculations match the measurements fairly well. This confirms that the K_e concept is also suitable for the soils encountered at the high-elevation SRYR.

Figure 5.1b and 5.1c present further comparisons of the κ_h measurements with estimates obtained via J75 and Z14, respectively, of which the latter accommodates for the effect of soil organic matter. A clear difference is noted in the ability of the J75 and Z14 schemes to reproduce the κ_h measurements. The slope of the linear function fitted through the Z14 matchups is closer to unity than that for the J75 matchups (e.g., 1.015 versus 1.160) and the scatter among the Z14 data points is also less leading to an R^2 of 0.885 versus 0.790. Apparently, soil organic matter is responsible for part of the κ_h variability and

its consideration is needed to further optimize the performance of parameterizations.

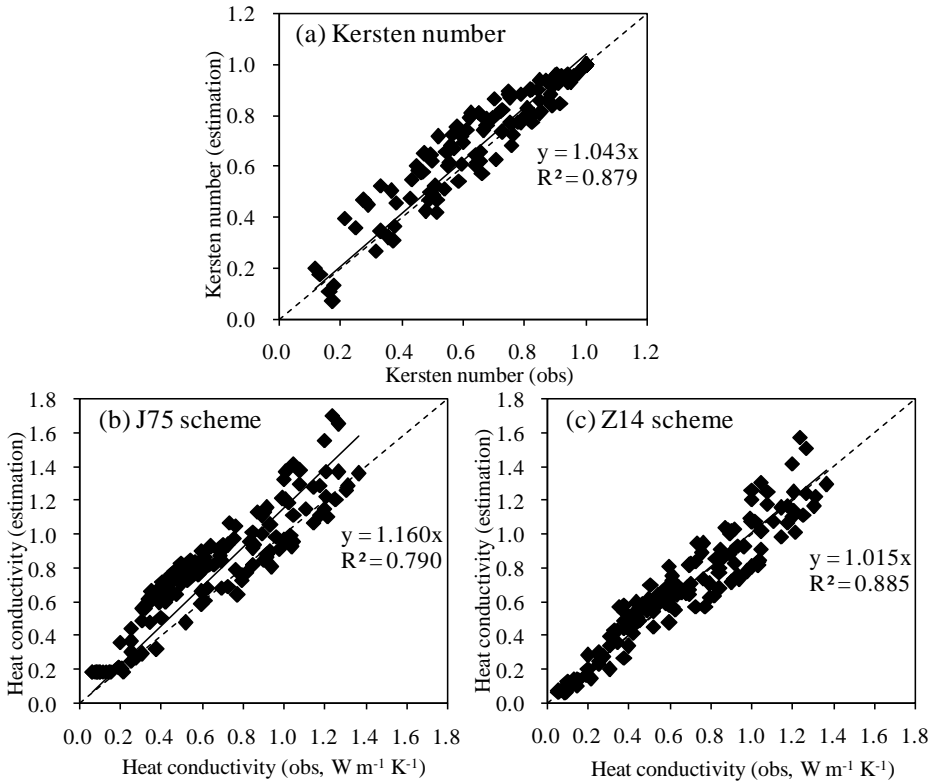


Figure 5.1: Scatter plots of laboratory measured and (a) computed Kersten number, (b) computed heat conductivity (κ_h) with J75, and (c) computed heat conductivity (κ_h) with Z14 of soil samples collected around SRYR.

Table 5.1: Coefficient of determination (R^2), mean error (ME) and root mean square error (RMSE) computed between measured and estimated dry heat (κ_{dry}), saturated heat (κ_{sat}) and heat conductivity (κ_h) for samples around Maqu station

Sche me	κ_{dry}			κ_{sat}		κ_h		
	R^2	ME (W m ⁻¹ K ⁻¹)	RMSE (W m ⁻¹ K ⁻¹)	R^2	ME (W m ⁻¹ K ⁻¹)	RMSE (W m ⁻¹ K ⁻¹)	ME (W m ⁻¹ K ⁻¹)	RMSE (W m ⁻¹ K ⁻¹)
J75	0.36	0.072	0.083	0.73	0.157	0.209	0.144	0.197
Z14	0.73	-0.009	0.026	0.81	0.008	0.128	0.022	0.115

Table 5.1 provides the error statistics computed between the measurements and heat conductivities (e.g., κ_h , κ_{dry} and κ_{sat}) and those estimated with the J75 and Z14 schemes, such as R^2 , mean error (ME) and root mean squared error (RMSE). From the error statistics can be deduced that on average the J75 scheme overestimates κ_{dry} by $0.072 \text{ W m}^{-1} \text{ K}^{-1}$ and κ_{sat} by $0.157 \text{ W m}^{-1} \text{ K}^{-1}$ leading to an overestimation of κ_h by $0.144 \text{ W m}^{-1} \text{ K}^{-1}$. This overestimation of the κ_h measurements is largely resolved through the consideration of soil organic matter by the Z14 scheme. It should, however, be noted that apart from the bias also a large part of the random differences between the measured and computed κ_{dry} is reduced given the increase of the R^2 from 0.362 to 0.727.

5.4 Noah simulations

5.4.1 Numerical experiments

Five experiments are performed to assess the impact of the augmentations described (see Section 5.2) to the default Noah LSM on the turbulent heat flux and soil temperature profile simulations using measurements collected at Maqu station located in the high-elevation SRYR. The Noah LSM is first run with the default soil property and roughness length parameterization, which is hereafter called ‘Ctrl’. The second experiment (EXP1) contains a Noah model run whereby the muting effect of vegetation on the heat conductivity from the mid-point of the 1st soil layer towards the mid-point of the 2nd soil layer is removed and a distinction is made between κ_{h0} and κ_{h1} . The third experiment (EXP2) consists of a simulation whereby the default value of β_{veg} in the Noah model structure is replaced by an expression (eq. (5.3)) as function of the *LAI* and *GVF*. For the fourth experiment (EXP3), a Noah model run is made with Zilitinkevich’s empirical coefficient, C_{zil} , parameterized as an indirect function of canopy height via z_{0m} (see Section 5.2.2) instead of a constant value. The default soil thermal parameterization is modified to the one that considers the effect of soil organic matter for the fifth experiment (EXP4).

An overview of these numerical experiments is provided in Table 5.2. The Noah model is run for all the experiments over the period from 8 June up to 30 September 2010 using measured atmospheric forcing data, i.e. air temperature, relative humidity, wind speed, air pressure, downward and upward shortwave radiations, downward longwave radiation and precipitation (see Table 2.1 of Chapter 2). The observation height of the air temperature and wind speed is 2.35 m. The soil temperature at the bottom boundary is defined as the annual mean air temperature, which is specified as 275 K at a depth of 8 m here based on observations. The prescribed vegetation type is grassland, and the monthly

GVF and *LAI* are given in Sections 5.2. The specified minimum ($z_{0m,min}$) and maximum ($z_{0m,max}$) momentum roughness length (z_{0m}) for grassland are set to 0.008 m and 0.041 m respectively as in Chapter 4. The silt loam is adopted as soil texture according to measured properties (see Table 2.2 of Chapter 2) found at the upper layers of the two SMST sites (CST01 and NST01) near the Planetary Boundary Layer (PBL) tower, while the hydraulic parameters and m_{soc} are taken as the average of the value derived from the measurements collected at the CST01 and NST01 sites. The other parameters are obtained from Noah’s default database (see Section 3.4 of Chapter 3).

Table 5.2: List of numerical experiments designed to test augmentations for the Noah LSM

Experiments	κ_{h0} and κ_{h1}	β_{veg}	C_{zil}	heat properties
Ctrl	Same (eqs. (3.24) and (3.25))	Constant (2.0)	Constant (0.1)	Default (Section 3.1.5)
EXP1	Different (eqs. (3.24) and (5.1))	Constant	Constant	Default
EXP2	Different	Variable (eq. (5.3))	Constant	Default
EXP3	Different	Variable	Variable (eqs.(5.4) and (5.5))	Default
EXP4	Different	Variable	Variable	New (Section 5.2.3)

Soil moisture and temperature measurements are used to initialize each model run as well as to validate Noah simulations. For both, the measurements collected at sites CST01 and NST01 are averaged for each soil depth (e.g., 0.05, 0.10, 0.20, 0.40 and 0.80 m), and subsequently interpolated to the mid-points of the upper three model layers (i.e., 0.05, 0.25 and 0.70 m). Then the soil moisture and temperature of the fourth layer is taken for initialization equal to the states of the third layer. The Noah simulations are validated further through comparisons of the simulated latent heat flux (LE) and sensible heat flux (H) with measurements collected by an eddy-covariance (EC) system.

5.4.2 Turbulent heat fluxes and soil temperature profiles

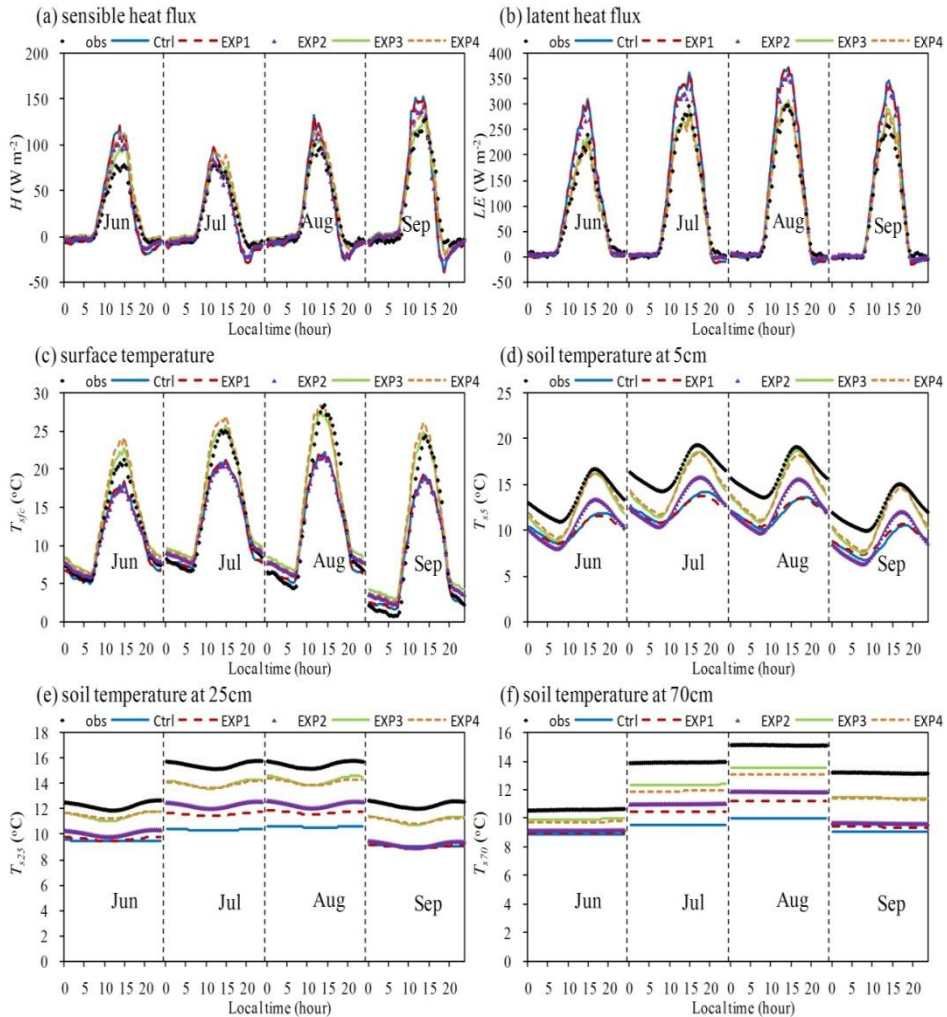


Figure 5.2: Average diurnal cycles for the months June, July, August and September of the measured and simulated (a) sensible heat flux, (b) latent heat flux, (c) surface temperature and soil temperatures for the depths (d) 5 cm, (e) 25 cm, and (f) 70 cm produced by five numerical experiments.

Figure 5.2 shows the mean diurnal variability for the months June, July, August and September of the measured and simulated turbulent (sensible and latent) heat fluxes and soil temperature profiles. Tables 5.3 and 5.4 provide respectively the ME and RMSE computed between the measured and simulated turbulent heat fluxes and soil temperature profiles. Analysis of the

measurements (black dots) reveals that the latent heat flux (LE) is, on average, more than twice as large as the sensible heat flux (H) during daytime. Further, it is noted that the amplitude of the diurnal temperature cycle diminishes with depth as expected and is almost completely vanished at the mid-point on the 3rd soil layer (70 cm). Also, the phase of the diurnal temperature cycle is affected by the soil depth showing that the maximum temperature is reached at a later time at greater depths.

Table 5.3: Mean error (ME) computed between the measured and simulated sensible (H) and latent (LE) heat fluxes, surface (T_{sfc}) and soil temperatures at depths of 5 cm (T_{s5}), 25 cm (T_{s25}), and 70 cm (T_{s70}) produced by five numerical experiments

ME	H ($W\ m^{-2}$)	LE ($W\ m^{-2}$)	T_{sfc} (K)	T_{s5} (K)	T_{s25} (K)	T_{s70} (K)
Ctrl	1.78	27.29	-1.07	-3.77	-4.16	-3.97
EXP1	1.72	27.11	-1.09	-3.84	-3.44	-3.31
EXP2	-0.05	22.93	-0.68	-3.32	-2.96	-2.88
EXP3	3.46	3.51	1.31	-1.43	-1.23	-1.43
EXP4	7.72	-0.42	1.44	-1.37	-1.27	-1.73

Table 5.4: Root mean square error (RMSE) computed between the measured and simulated sensible (H) and latent (LE) heat fluxes, surface (T_{sfc}) and soil temperatures at depths of 5 cm (T_{s5}), 25 cm (T_{s25}), and 70 cm (T_{s70}) produced by five numerical experiments

RMSE	H ($W\ m^{-2}$)	LE ($W\ m^{-2}$)	T_{sfc} (K)	T_{s5} (K)	T_{s25} (K)	T_{s70} (K)
Ctrl	24.38	54.75	2.85	3.93	4.36	4.19
EXP1	24.71	54.88	2.86	4.01	3.51	3.45
EXP2	20.44	46.86	2.99	3.39	3.01	2.99
EXP3	14.12	30.93	2.48	1.76	1.29	1.50
EXP4	17.44	30.36	2.62	1.61	1.35	1.81

In its default configuration, Noah (Ctrl) overestimates both the daytime (09-18 h) sensible (H , Figure 5.2a) and latent (LE , Figure 5.2b) heat fluxes, and somewhat underestimates the heat fluxes after dusk (19-24 h). Most notable is the daytime LE overestimation, which can be larger than $50\ W\ m^{-2}$. On the other hand, the Ctrl model run underestimates the daytime surface temperature (T_{sfc} , Figure 5.2c) because H and LE affect the magnitude of the computed surface

temperature negatively (see eq. (3.15) in Chapter 3). Moreover, an underestimation of the temperatures at soil depths of 5 cm (T_{s5} , Figure 5.2d), 25 cm (T_{s25} , Figure 5.2e) and 70 cm (T_{s70} , Figure 5.2f) is found. This can be explained by the fact that less heat is entering the soil column during daytime due to overestimations of H and LE , and more heat is released during nighttime due to the heat flux (H and LE) underestimations.

The turbulent heat fluxes and T_{sfc} produced by EXP1 are nearly identical to the Ctrl simulations. This demonstrates that the separation of heat conductivities for the surface (κ_{h0}) and first (κ_{h1}) soil layers has a minor impact on the turbulent heat flux and T_{sfc} simulations. In contrast, the deep soil temperature (e.g., T_{s25} and T_{s70}) simulations are improved in the EXP1, particularly for the months July and August when the vegetation cover is largest. This is caused by the removal of the muting effect of vegetation on the heat conductivity from the mid-point of the 1st soil layer towards the mid-point of the 2nd soil layer (κ_{h1}). As such, more heat is transported into the soil column, which increases the deep soil temperature. The parameterization of β_{veg} via eq. (5.3) included in EXP2 further improves the deep soil temperature simulations and enlarges the simulated diurnal T_{s5} variability. Eq. (5.3) generates lower β_{veg} (≈ 1.0) values resulting in a larger κ_{h0} (see eq. (3.24)) and ground heat flux (G_0 , see eq. (3.13)). As more energy is transported into the soil column, less energy remains for the production of the turbulent heat fluxes leading to improvements of 4.27 W m^{-2} and 8.06 W m^{-2} in the RMSEs computed between measured and simulated H and LE in EXP2, respectively. It should, however, be noted that the daytime T_{sfc} underestimation remains and that in the morning (00-08 h) the EXP2 simulations overestimate T_{sfc} , while T_{s5} is underestimated. The latter is induced by the lower β_{veg} that enables an accelerated release of heat from the soil column as will be further elaborated on in the discussion.

The overestimation of the daytime turbulent heat fluxes is greatly resolved in the EXP3 model run, for which Zilitinkevich's empirical coefficient, C_{zil} , is calculated as an indirect function of canopy height via z_{0m} (see Section 5.2.2). With this augmentation, the Noah LSM uses higher C_{zil} values and computes, thus, lower C_h values (see eqs. (3.3) and (3.28)). This leads to the production of less turbulent heat (see eq. (3.2) for H and eq. (3.11) for LE), which consequently causes an increase in the simulated daytime T_{sfc} . Most notably the RMSEs computed between the measured and simulated turbulent heat fluxes improves by 31 % and 34 % for H and LE in comparison to the performance of EXP2, respectively. This is, in particular for the LE , achieved by a reduction in the bias from 22.93 W m^{-2} to 3.51 W m^{-2} .

As less energy is consumed by turbulent transport, more heat is available for the warming of the soil column leading to an improved soil temperature profile simulation. Hence, the underestimation of the measured temperature reduces in comparison to EXP2 by 1.89 K, 1.73 K and 1.45 K for soil depths of 5 cm, 25 cm and 70 cm, respectively. It should, however, be noted that the overestimation of nighttime T_{sfc} , first seen in the EXP2 simulation, is further amplified by the augmentation introduced in EXP3.

The performance of EXP4 is comparable to that of EXP3 implying that consideration of organic matter in the soil thermal parameterization (see Section 5.2.3) has little impact on the heat flux and soil temperature simulations at the Maqu micro-meteorological station. On the other hand, the soil organic matter mass fraction (m_{soc}) is relatively low for this site (< 3 %). The effect of organic matter on the Noah LSM performance will be further investigated in the discussion through a sensitivity analysis.

5.4.3 Assessment via Taylor diagram

Taylor diagrams (Taylor 2001) are further used to assess the model performance in reproducing the diurnal surface heat flux and soil temperature patterns (with a 30-min interval) in terms of phase, and amplitude of unbiased matchups for all five experiments. The magnitude of RMSE as error statistics is largely determined by the bias between two dataset and may, therefore, provide an ambiguous view on the model performance. Pearson's product-moment correlation coefficient (R) is used as a measure for the agreement between the measured and simulated phase. The normalized standard deviation (SDV) is utilized to evaluate the amplitude, which is defined by,

$$SDV = \hat{\sigma}_f = \sigma_f / \sigma_r, \hat{\sigma}_r = 1 \quad (5.14)$$

where σ_f and σ_r are the standard deviations of a test field (i.e., simulation) and a reference field (i.e., measurement), respectively.

Obs – Observations, 0 – Ctrl, 1 – EXP1, 2 – EXP2, 3 – EXP3, 4 – EXP4

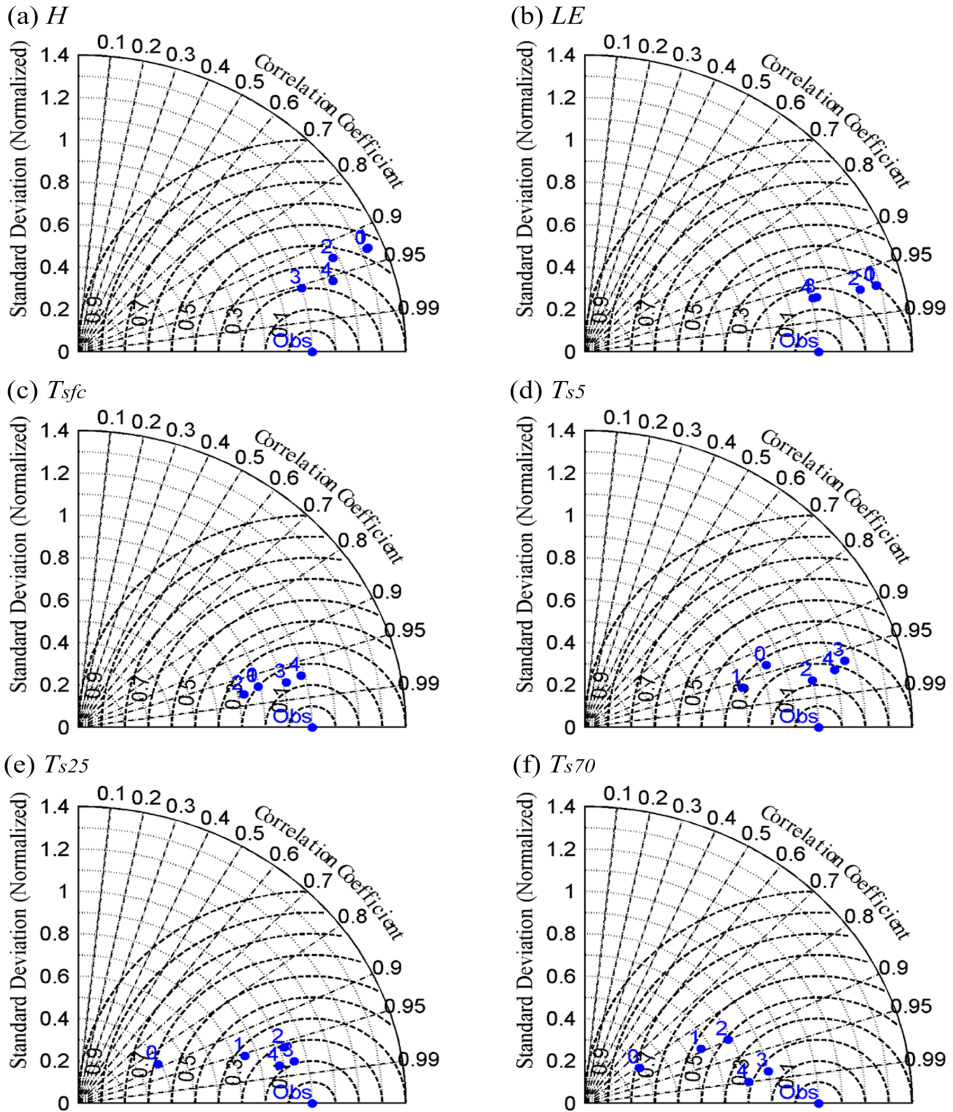


Figure 5.3: Taylor diagrams illustrating the model performance as if the measurements and the simulated variables are unbiased: (a) sensible heat flux, (b) latent heat flux, (c) surface temperature and soil temperatures for the depths (d) 5 cm, (e) 25 cm, and (f) 70 cm. The radial distance from the origin is the normalized standard deviation (SDV) and the correlation coefficient (R) is displayed as the azimuthal position. Then, the distance of the data point to the measurements (located at $R = 1$ and $SDV = 1$) is the normalized centered root mean squared error (cRMSE).

In Taylor diagrams, the normalized standard deviation is taken as the radius, whereas Pearson's correlation coefficient is adopted as the angle of a polar plot. Data points showing a perfect fit with the measurements are located on the x-axis at $R = 1$ and $SDV = 1$. The distance to this point is the RMSE of two unbiased data sets, which is referred to as the centered normalized RMSE (cRMSE) and can also be calculated as,

$$cRMSE = \hat{E}' = E' / \sigma_r \quad (5.15)$$

$$E' = \left\{ \frac{1}{N} \sum_{i=1}^N [(f_i - \bar{f}) - (r_i - \bar{r})]^2 \right\}^{1/2} = (RMSE^2 - ME^2)^{1/2} \quad (5.16)$$

where E' is the centered RMSE, \bar{f} and \bar{r} are the mean values of the simulation and measurement, respectively.

Figure 5.3 shows that in all the experiments the Noah LSM is able to produce a phase that matches the surface heat flux and soil temperature profile measurements reasonably well as indicated by the R values varying from about 0.90 up to 0.99. In the case of the simulated LE , T_{sfc} and T_{s5} the magnitude of R remains about the same for all five model runs. On the other hand, differences are noted among the R values computed between the measurements and simulations of H , T_{s25} and T_{s70} , whereby a better agreement in the phase is achieved with the augmentations made for EXP3 (and EXP4).

The Ctrl model run exaggerates the amplitude of the diurnal cycle of the turbulent heat fluxes by more than 25 % (e.g., $SDV > 1.25$), and underestimates the amplitude of diurnal cycle of the surface and soil temperatures by more than 15 % (e.g., $SDV < 0.85$). The latter underestimation is most severe for the deep soil temperatures (T_{s25} and T_{s70}) and is as large as 60 %. The augmentation incorporated in EXP1 largely resolves this bias in the deep soil temperatures, but has little impact on Noah's performance in the turbulent heat flux and near surface temperature (T_{sfc} and T_{s5}) simulations. The major improvement in the simulation of the T_{s5} variability is obtained with EXP2 when the vegetation effect on the heat transport through the soil is reconsidered, which also reduces somewhat the overestimation of the turbulent heat flux variability.

With SDV values close to 1.0 for both the H and LE , the most significant enhancement in the performance of simulating the diurnal turbulent heat flux variability is, however, noted once the C_{zil} is parameterized as (indirect) function of canopy height (EXP3). As less energy is consumed by the turbulent heat transport, the simulated diurnal surface and soil temperature variability increases yielding a better agreement with the measurements, except for T_{s5} in

which case the diurnal variability is overestimated. In general, the EXP4 model run produces very similar, but slightly worse SDV values in comparison to EXP3. Only the ability of capturing the diurnal H variability deteriorates quite drastically with more than 10 %, which follows most likely from smaller imperfections in the simulation of the T_{sfc} .

The distance of the points in the Taylor diagram to the perfect matchup at $R = 1$ and $SDV = 1$ (or $cRMSE$) is typically found for EXP3 and comparable results are obtained by EXP4 in terms of LE and T_{sfc} . In the T_{s5} simulation, however, EXP2 outperforms EXP3 and EXP4. In essence, this confirms the conclusions drawn based on Figure 5.2 and the Tables with the RMSE and ME as performance indicators. Nevertheless, the favorable result noted for EXP2 in simulating T_{s5} is somewhat surprising, which suggests that room is available for further improving the model physics of the soil heat transport as will be discussed below.

5.5 Discussion

5.5.1 Improvement of nighttime surface temperature simulation

Although the augmentations proposed for the default Noah LSM (see Section 5.2) greatly improved the performance of turbulent heat fluxes and soil heat transport, one of the remaining issues is the overestimation of nighttime T_{sfc} . This leads to the underestimation of nighttime T_{s5} (see Figure 5.2d) and decreasing performance with respect to the Taylor statistics. Zeng et al. (2012) investigated recently a similar issue associated with the simulation of nighttime T_{sfc} by the Noah LSM. They suggested that the problem may be resolved by: i) increasing the number of iterations to secure a converged solution for the MOST equations (see eqs. (3.2)-(3.10)) for turbulent heat transport, ii) modifying the stability function, Ψ , for stable atmosphere conditions, and iii) constraining the ground heat flux (G_0).

In accordance with Zeng's recommendation, three additional experiments are carried out to investigate the possibility of resolving the nighttime T_{sfc} overestimation. Firstly, the maximum number of iterations for the turbulent heat transport is increased from 5 to 30 (hereafter 'EXPS1'). Secondly, the Noah's default stability functions (see eqs. (3.7)-(3.10)) for stable conditions by Paulson (1970) is replaced with the formulations proposed either by Holtslag and De Bruin (1988) (hereafter 'EXPS2a') or by Łobocki (1993) (hereafter 'EXPS2b'). The above mentioned stability functions are given in Appendix A.2 of this thesis. Thirdly, the G_0 is constrained for stable atmospheric conditions by

setting factor β_{veg} to 2.0 and is hereafter referred to as ‘EXPS3’. Other settings of the Noah LSM are kept the same as for EXP3 described in Section 5.4.

Table 5.5 gives the RMSEs computed between the measurements and simulated turbulent heat fluxes and soil temperatures. It indicates that the maximum number of iterations and adopted atmospheric stability function do not affect the model performance as EXPS1 and EXPS2a/b yield RMSEs comparable to EXP3. In contrast, the performance in simulating soil temperature profiles (T_{s5} , T_{s25} and T_{s70}) greatly improved by implementing different β_{veg} values for stable and unstable conditions (EXPS3). This reduces in comparison to EXP3 the RMSE computed between the measured and simulated soil temperatures for depths of 5 cm, 25 cm and 70 cm by about 41, 35 and 78 %, respectively. A decrease in the RMSE is also noted for T_{sfc} , while the agreement between measured and simulated turbulent heat fluxes (e.g., LE and H) somewhat degrades.

Table 5.5: Root mean square error (RMSE) computed between the measured and simulated sensible (H) and latent (LE) heat fluxes, surface (T_{sfc}) and soil temperatures at depths of 5 cm (T_{s5}), 25 cm (T_{s25}), and 70 cm (T_{s70}) produced by the experiments performed for the discussion (Section 5.5)

RMSE	H ($W\ m^{-2}$)	LE ($W\ m^{-2}$)	T_{sfc} (K)	T_{s5} (K)	T_{s25} (K)	T_{s70} (K)
Ctrl	24.38	54.75	2.85	3.93	4.36	4.19
EXP3	14.12	30.93	2.48	1.76	1.29	1.50
EXPS1	14.12	30.93	2.48	1.76	1.29	1.50
EXPS2a	14.11	30.93	2.48	1.76	1.29	1.50
EXPS2b	14.13	30.93	2.48	1.76	1.29	1.50
EXPS3	14.74	32.39	2.37	1.04	0.84	0.33
EXPS4	19.86	31.45	2.70	1.25	1.01	0.41
EXPS5	20.57	31.50	2.76	1.21	0.96	0.51
EXPS6	29.30	32.00	3.42	1.67	1.21	0.71

Figure 5.4 further shows the average diurnal cycle of the measured and simulated turbulent heat fluxes and soil temperatures produced with Ctrl, EXP3 and EXPS3. The overestimation of nighttime T_{sfc} invoked by EXP2 and further amplified in the EXP3 is considerably mitigated by the augmentation made for the EXPS3, which leads to the likewise improvements in the simulations of deep soil temperature (see Figures 5.4d-5.4f). Moreover, amelioration of the

nighttime T_{sfc} leads also to an enhancement in the nighttime sensible heat flux (H) simulation.

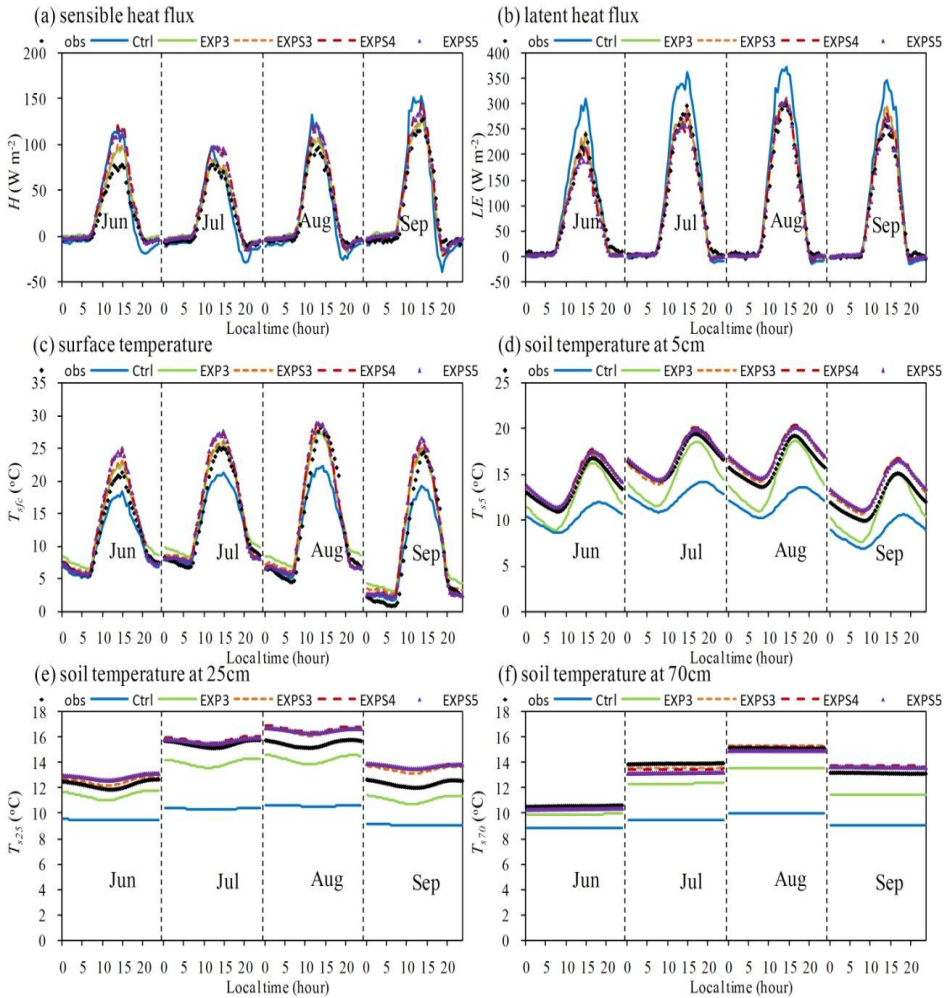


Figure 5.4: Average diurnal cycles for the months June, July, August and September of the measured and simulated (a) sensible heat flux, (b) latent heat flux, (c) surface temperature and soil temperatures for depths of (d) 5 cm, (e) 25 cm, and (f) 70 cm produced by the experiments performed for the discussion (Section 5.5).

The above results support the suggestion by Zeng et al. (2012) that the issue associated with the heat exchange under stable conditions should be treated from a coupled land-atmosphere rather than from an atmospheric turbulence

perspective alone. In other words, deficiencies in simulating nighttime T_{sfc} and turbulent heat fluxes can be improved by constraining the G_0 because of the link with the turbulent heat fluxes via the surface energy budget. In the case of EXPS3, a higher value of β_{veg} (2.0) is utilized to suppress the heat released from the soil column to the surface at night and a lower value of β_{veg} (≈ 1.0 , computed with eq. (5.3)) ensures an accelerated warming of the soil column during the day. Similarly, Best (1998) found that the T_{sfc} simulated for a grassland environment does not decrease sufficiently during the night without modifying the role of the vegetation canopy in the surface energy budget calculations.

The rationale for utilizing different daytime and nighttime β_{veg} values here is associated with the Noah model structure that the soil-vegetation system is represented as a single heat/water vapor source, and the canopy effect on the radiation transfer and surface energy budget computations cannot be explicitly considered. A similar issue was resolved by Wang et al. (2010) through considering the under-canopy resistance, while Niu et al. (2011) substantially revised the Noah LSM to a dual source model structure. The solution found here by the EXPS3 sensitivity test provides a pragmatic solution to a complex problem without the necessity of changing the Noah model structure. Obviously, a more formal approach with robust physics is preferred and deserves further study.

5.5.2 Impact of soil moisture simulation

Since both thermal heat conductivity (κ_h) and capacity (C_s) depend on all soil constituents and the soil moisture content, see Section 5.2.3, the uncertainties associated with the soil moisture characterizations will affect the soil heat transport simulation. Moreover, the LE produced by the Noah LSM depends also on the water availability in the root zone and, thus, soil moisture affects the computed surface energy budget as well. Despite the soil moisture profile simulations are greatly improved with the modified soil hydraulic parameterization and vertical root distribution (see Chapter 6 of this thesis), uncertainties remain with RMSEs of 0.04 and 0.015 $\text{m}^3 \text{m}^{-3}$ for the surface (e.g., 5 cm) and deeper (e.g., 25 and 70 cm) soil layers, respectively.

Instead of using the measurements, the soil water flow component is invoked (parameterized as ‘EXP2’ in Chapter 6) to investigate the impact of soil moisture uncertainties on the turbulent heat flux and soil heat transport simulations, while other settings are as EXPS3 (hereafter ‘EXPS4’). The average diurnal cycle of the turbulent heat fluxes and soil temperatures produced by the EXPS4 is also plotted in Figure 5.4, and Table 5.5 lists the

respective RMSEs. Figure 5.4 shows that EXPS4 overestimates the daytime H (Figure 5.4a) and T_{sfc} (Figure 5.4c) with respect to EXPS3 and the measurements, which may be due to the surface soil moisture underestimation (see Table 6.4 in Chapter 6). The soil moisture underestimations in the upper two soil layers (e.g., 5 and 25 cm) also lead to a slight overestimation of temperatures of the corresponding soil layers (see Figures 5.4d-5.4e). The EXPS4 RMSEs are about 0.33, 0.21, 0.17 and 0.08 K larger for surface and 5 cm, 25 cm and 70 cm soil temperatures in comparison to the EXPS3. Also the RMSE for H increases by 5.12 W m^{-2} , while the RMSE for LE improves somewhat (0.94 W m^{-2}). Nevertheless, the performance of the fully augmented Noah LSM (e.g., EXPS4) performs considerably better than the default Noah LSM that makes use of the soil moisture measurements. This study highlights once again that the surface energy budget calculations by physically based LSMs can only be ameliorated if the water budget is considered as well.

5.5.3 Sensitivity analysis of organic matter parameterization

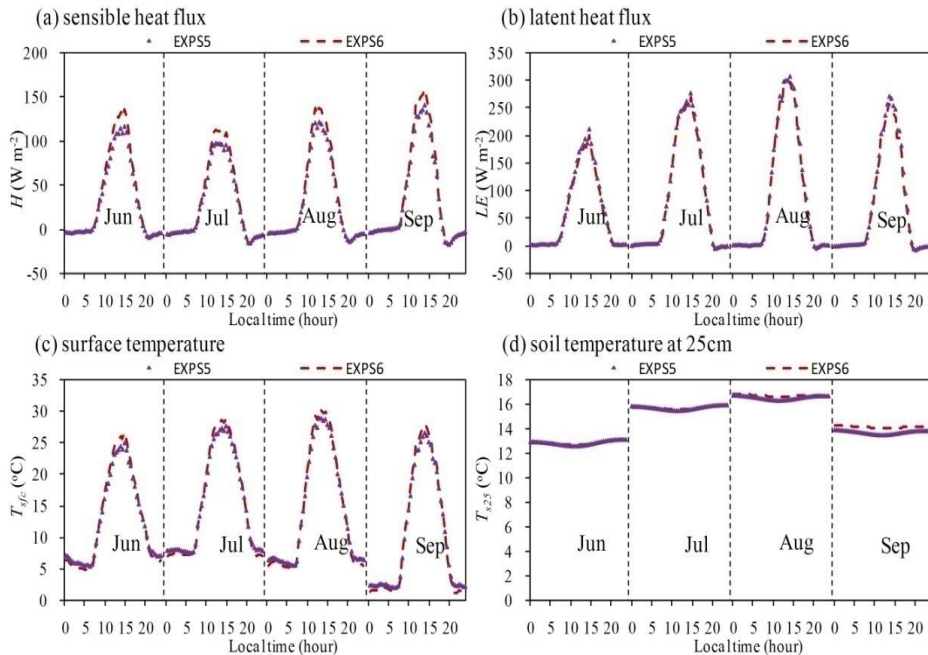


Figure 5.5: Average diurnal cycles for the months June, July, August and September of the simulated (a) sensible heat flux, (b) latent heat flux, (c) surface temperature and (d) soil temperature for the depth of 25 cm produced by EXPS5 and EXPS6 designed to assess the sensitivity for soil organic matter (Section 5.5.3).

Although usage of organic matter for calculating the thermal heat conductivity (κ_h) improves the agreement between estimates and laboratory measurements across the entire m_{soc} range, the results of Section 5.4 reveal only a small impact on the heat flux and soil temperature simulations for the Maqu micro-meteorological station. On the other hand, Maqu station holds a relatively low m_{soc} for the top ($\sim 2.5\%$) as well as the deep soil layers ($\sim 0.5\%$ at 60 cm), whereas the wetland ecosystems in the region contain a much larger amount of organic matter ($> 15\%$ near the surface). Two additional numerical experiments are carried out to further assess the sensitivity of the model results when m_{soc} is considered for both the soil thermal and soil hydraulic parameterizations. For the first experiment (hereafter ‘EXPS5’), the consideration of m_{soc} is also invoked for the soil thermal parameterization as described in Section 5.2.3, while the other settings are taken as in EXPS4. In the second experiments (hereafter ‘EXPS6’), Noah is run with the same options as EXPS5 but using m_{soc} of the wetland soil profile, e.g., 15 %, 10 %, 5 % and 2.5 % for the respective four soil layers.

Figure 5.5 shows the time series of the average diurnal cycle of the turbulent heat fluxes and soil temperatures produced with EXPS5 and EXPS6. In addition, the average diurnal turbulent heat flux and soil temperature cycle produced by EXPS5 is added to Figure 5.4. Further, the RMSEs computed for EXPS5 and EXPS6 are included in Table 5.5 primarily for reference purposes and not as an accuracy measure, especially for EXPS6. In general EXPS5 is nearly identical to EXPS4, which confirms the findings of Section 5.4 that consideration of m_{soc} in the soil thermal parameterization has little impact on the Noah performance for Maqu station. Similarly, the comparison of the diurnal cycles of EXPS5 and EXPS6 shows that the impact of m_{soc} is inferior to the effect of the roughness parameterization. Nevertheless, average differences of about 6 and 5 W m^{-2} are noticed for H and LE respectively, and a proportional effect is seen among the simulated temperatures.

5.6 Conclusions

This study investigates the turbulent heat flux and soil heat transport simulated by the Noah land surface model (LSM) through comparisons against sensible (H) and latent (LE) heat flux, and soil temperature profile measurements taken during the monsoon season (e.g., June, July, August, and September) at the Maqu station in the source region of the Yellow River (SRYR). The default Noah LSM constrained by soil moisture profile measurements significantly overestimates the daytime turbulent heat fluxes and

underestimates the surface temperature (T_{sfc}), and the soil temperatures are systematically underestimated as well.

Four augmentations to the model physics are investigated for resolving the above deficiencies: i) the muting effect of vegetation on the soil heat conductivity (κ_h) from the mid-point of the 1st soil layer towards the mid-point of the 2nd soil layer is removed, ii) the exponential decay factor (β_{veg}) imposed on κ_h is parameterized as a function of the ratio of the leaf area index (LAI) over the green vegetation fraction (GVF), iii) Zilitinkevich's empirical coefficient (C_{zil}) defining the efficiency of turbulent heat transport is parameterized as a function of canopy height via the momentum roughness length (z_{0m}), and iv) the impact of organic matter is included in the thermal heat conductivity (κ_h) and capacity (C_s) parameterization. The modified soil thermal parameterization is compared against laboratory measured soil heat conductivities. It is shown that through consideration of organic matter within the default heat conductivity scheme (Johansen 1975) of the Noah LSM, the root mean squared error (RMSE) computed between the estimated and measured heat conductivities under dry (κ_{dry}) and saturated (κ_{sat}) soil moisture conditions reduced by 69 and 39 %, respectively. Similar improvements are noted for the estimated heat conductivities at intermediate saturation levels.

Five numerical experiments, including a control run with the default model structure (Ctrl), are designed to progressively assess the impact on the model performance of the four augmentation described above. Removal of the muting effect of vegetation on the soil heat transport from the first layer towards the deep soil increases the diurnal temperature variability simulated for the deep soil by about 50 %, while a negligible impact is noted on the turbulent heat flux and T_{sfc} simulations. The parameterization of β_{veg} by the LAI/GVF ratio (≈ 1.0) enhances the heat exchange between the land surface and soil column. This mitigates the underestimation of the diurnal temperature variability in the deep soil (T_{s5} , T_{s25} , and T_{s70}) and simultaneously alleviates somewhat the turbulent heat flux overestimation. The most significant improvements in the T_{sfc} and turbulent heat flux simulations are found once C_{zil} is parameterized as a function of the canopy height via z_{0m} . However, the model run whereby soil organic matter is used for determining the soil thermal properties does not yield any noticeable improvement with respect to the other numerical experiments performed for Maqu station that holds a relatively low organic matter content (m_{soc}) of 2.5 % for the top soil. In comparison to the default model structure, the performance in simulating the turbulent heat fluxes and soil heat transport improves for the Noah LSM with the three most promising augmentations. In

this case the RMSEs computed between the measurements and simulations reduced by about 42, 44, 13, 55, 70, and 64 % for H , LE , T_{sfc} , T_{s5} , T_{s25} , and T_{s70} , respectively.

Three additional experiments are conducted to investigate the remaining issue associated with the overestimation of nighttime T_{sfc} . It is found that this problem cannot be solved by considering the atmospheric turbulence alone, but should be treated from a coupled land-atmosphere perspective. Further, the impact of the uncertainty associated with the model's characterization of the soil moisture profile on the simulated surface energy budget is assessed as well. This experiment demonstrates that the fully augmented Noah LSM, including the improved soil water flow (see Chapter 6 of this thesis) as well as the above described turbulent heat flux and soil heat transport model physics, provides better estimations of turbulent heat fluxes and soil temperatures in comparison to the control run, which is constrained by the soil moisture profile measurements. As such, the performance enhancement achieved with the selected augmentations outweighs the uncertainty introduced by the imperfection in the simulated soil moisture. Furthermore, the impact of m_{soc} on the Noah performance is assessed by adopting the case of an organic wetland soil common to the region. This experiment demonstrates that while the consideration of organic matter is imperative for the soil moisture profile, the impact on the heat flux and temperature profile is inferior to other augmentations addressed herein.

This study highlights again that the most effective way to improve the heat flux and soil temperature simulations on the Tibetan Plateau is to improve the parameterization of the diurnally varying roughness length for heat transfer (z_{oh}) as found by previous studies (Chen et al. 2011; Zeng et al. 2012; Zheng et al. 2014). While a significant improvement is achieved in the soil water flow simulation through a better representation of the hydraulic parameterization with the consideration of the organic matter effect (see Chapter 6 of this thesis), it is shown that consideration of organic matter in the soil thermal parameterization has little impact on the heat flux and soil temperature simulations. Although the Noah LSM simulations are validated in this study only for a site on the Tibetan Plateau, the addressed issues are inherent to the model structure of the Noah LSM. For instance, the large negative biases in the Noah LSM simulated soil temperature found by Xia et al. (2012a) within the North American Land Data Assimilation System (NLDAS) product may be resolved by adopting the suggested augmentations.

Chapter 6 Augmentations to the soil water flow simulation*

6.1 Introduction

Soil moisture is a key state variable controlling the partitioning of available energy at the land surface between sensible and latent heat, as well as determining the partitioning of rainfall between subsoil drainage, surface runoff, and evaporation. Thus, it is crucial to reliably simulate soil water flow processes to enable providing realistic soil moisture states. However, large differences and biases exist among the soil moisture products generated by various land surface models (LSMs) driven with the same meteorological forcing (Dirmeyer et al. 2006; Xia et al. 2014) due to different model physics, structure and parameter choices. For instance, several vertical root distribution schemes (i.e., root depth and density) are implemented by the current LSMs (Zeng 2001), and the diversity of soil hydraulic functions as well as hydraulic parameters pose a high uncertainty as well (Decharme et al. 2011; Shao and Irannejad 1999). Moreover, the LSMs have originally been developed for large-scale applications and numerical efficiency. Therefore, the presence of irrigation and groundwater processes is often ignored (e.g., Xia et al. 2014), and the number of soil layers is limited and extends down to a few meters (e.g., Gulden et al. 2007). Besides, the soil profile is assumed homogeneous, and either the diffusivity form of Richards' equation (e.g., Balsamo et al. 2009; Liang et al. 1996) or a force-restore approach (Decharme et al. 2006) is employed for the soil water flow simulation by LSMs that does not accommodate for transport across layers with different hydraulic properties.

Recently, Y. Chen et al. (2013), Su et al. (2013) and Xue et al. (2013) have reported on the inability of LSMs to reproduce the soil moisture and temperature profiles measured by newly developed in-situ monitoring networks across the central and eastern parts of the Tibetan Plateau (Su et al. 2011; Yang et al. 2013). A major reason for the weak performance of LSMs in this region is the absence of vertical soil heterogeneity within model structures (Y. Chen et al. 2013; Yang et al. 2005). Particularly, many roots are present in the upper soil

***This chapter is based on the paper:** Zheng, D., R. van der Velde, Z. Su, X. Wang, J. Wen, M. J. Booi, A. Y. Hoekstra, and Y. Chen, 2015: Augmentations to the Noah model physics for application to the Yellow River source area: Part I. Soil water flow. *Journal of Hydrometeorology*, doi: 10.1175/JHM-D-14-0198.1.

layer of Tibetan ecosystems as an adaptation to the harsh Tibetan environment (Y. Yang et al. 2009a). This leads to the accumulation of organic matter in the topsoil (Y. Yang et al. 2009b) and causes a soil stratification (Chen et al. 2012). Organic matter, and living and decayed root systems share a large volume of the topsoil, affecting the soil structure as well as its hydraulic and thermal properties (Chen et al. 2012). Organic matter generally has a higher porosity, hydraulic conductivity, and thermal heat capacity, while a lower thermal heat conductivity and less suction needs to be applied to release water as compared to mineral soils (de Vries 1963; Lawrence and Slater 2008; Letts et al. 2000).

Previous studies have shown that the vertical soil heterogeneity as well as the effect of organic matter and root systems not only affects the thermal and moisture regimes at the ground (Beringer et al. 2001; Letts et al. 2000; Yang et al. 2005), but also the dynamic interactions with the overlaying atmosphere (Lawrence and Slater 2008; Rinke et al. 2008). It is, therefore, indispensable for the applicability atmospheric general circulation models (AGCMs) to polar and boreal ecosystems that the organic matter as well as the vertical soil heterogeneity is considered by LSMs. However, parameterizations for organic soil types are typically not implemented by the state-of-the-art LSMs. In the past, Beringer et al. (2001) and Letts et al. (2000) have studied the soil water flow through a column of pure organic material overlaying mineral soil layers, while Lawrence and Slater (2008) conceptualized the soil water transport through a mixture of coexisting organic and mineral components whose physical properties are additive. These two approaches have been developed specifically for the Arctic and Boreal organic soils and its applicability to the Third Pole Environment, as the Tibetan Plateau is also referred to, is yet to be proven. Although Chen et al. (2012) have recently investigated the effect of organic soil on soil thermal parameterization for grasslands in Central Tibet, additional work is needed to assess the impact of organic soil on soil hydraulic parameterization as well as the simulated surface energy and water budgets.

Therefore, this study seeks to further improve a state-of-the-art Noah LSM (Ek et al. 2003) in its ability to produce soil moisture profiles measured in the Source Region of the Yellow River (SRYR) on the Northeastern Tibetan Plateau. The model physics associated with the soil water flow simulation is investigated through comparisons of the soil parameterization with hydraulic properties measured in the laboratory and through comparisons of simulations with in-situ soil moisture profile measurements. Three augmentations are made: Firstly, the effect of organic matter on soil hydraulic properties is considered via the ‘additivity’ hypothesis (Zeiliger et al. 2000). Secondly, the saturated

hydraulic conductivity (K_s) is implemented as an exponentially decaying function of soil depth according to Beven (1982). Thirdly, the vertical root distribution scheme is modified to represent the abundance of roots in the topsoil that is characteristic for the Tibetan conditions. The impact of the augmentations on the simulated surface energy and water budgets is evaluated via inter-comparisons, whereas specifically the sensible and latent heat flux computations are assessed using in-situ measurements.

The structure of this Chapter is as follows: Section 6.2 introduces the measurements and describes the augmentations made to the Noah model physics associated with soil water flow and root water uptake. Section 6.3 presents comparisons of the modified hydraulic parameterization and measured soil properties. Section 6.4 provides a performance assessment of the soil moisture profiles simulated by Noah with different options. The impact of the improved soil moisture simulations on the calculated surface energy and water budgets is evaluated in Section 6.5, and Section 6.6 summarizes the findings of this study.

6.2 Materials and methods

A detailed description of the Maqu observational dataset utilized for this study is available in Chapter 2 of this thesis. Two soil moisture and soil temperature (SMST) monitoring stations (CST01 and NST01) are situated in the vicinity of the Maqu micro-meteorological observing system and are used for the presented analyses. The time period under investigation covers the majority of the monsoon season starting on 8 June 2010 and ending 30 September 2010. This episode is selected to avoid the impact of the cold season (e.g., snowpack and frozen soil) on the assessment of Noah's soil water flow and heat transport model physics.

In the text below, the augmentations made to the Noah model physics aimed at improving the soil water flow simulation are introduced. Detailed descriptions of the default Noah model physics associated with soil water flow and root water uptake can be found in Chapter 3 of this thesis (see Section 3.2). Unless stated otherwise, an updated version of the default model that implementing the augmentations made to the turbulent and soil heat transport processes given in Chapter 5 of this thesis is utilized.

6.2.1 Organic matter effect on soil hydraulic parameterization

Soil organic matter content affects the structure as well as the physical properties of the soil and, thus, the effects of organic matter on the hydraulic

properties need to be understood and taken into consideration. The approach utilized in this study is based on the ‘additivity’ hypothesis (Federer et al. 1993; Lawrence and Slater 2008; Zeiliger et al. 2000) that considers i) each soil layer as a mixture of organic and mineral masses, ii) the bulk densities of soil organic matter ($\rho_{b,soc}$) and mineral material ($\rho_{b,min}$) constant in any mixture, and iii) the volume occupied by the organic ($V_{t,soc}$) and mineral ($V_{t,min}$) fractions, as well as water retention to be additive.

Based on above assumptions, the volumetric soil carbon or organic fraction of a soil layer ($f_{t,soc}$) can be defined as (Chen et al. 2012; Federer et al. 1993):

$$f_{t,soc} = \frac{V_{t,soc}}{V_t} = m_{soc} \frac{\rho_b}{\rho_{b,soc}} \quad (6.1)$$

$$\rho_b = \frac{\rho_{b,min} \rho_{b,soc}}{m_{soc} \rho_{b,min} + (1 - m_{soc}) \rho_{b,soc}} \quad (6.2)$$

$$\rho_{b,min} = \rho_{s,min} \cdot (1 - \theta_{s,min}) \quad (6.3)$$

where V_t is the total volume of the soil layer (m^3), $V_{t,soc}$ is the volume occupied by organic matter (m^3), m_{soc} is the organic carbon mass content ($kg\ kg^{-1}$), ρ_b , $\rho_{b,soc}$ and $\rho_{b,min}$ are bulk densities ($kg\ m^{-3}$) of respectively the soil mixture, the organic and mineral materials, $\rho_{s,min}$ and $\theta_{s,min}$ are the particle density ($kg\ m^{-3}$) and the porosity ($m^3\ m^{-3}$) of mineral matter. Herein $\rho_{s,min}$ and $\rho_{b,soc}$ are taken as $2700\ kg\ m^{-3}$ (equivalent to a standard particle density of quartz; Peters-Lidard et al. 1998) and $130\ kg\ m^{-3}$ (equivalent to a standard bulk density of peat; Lawrence and Slater 2008) respectively. Given the m_{soc} , the ρ_b as well as the $f_{t,soc}$ can be derived via above equations. It should be noted that the definition of the fractional soil organic matter is different for the calculation of the hydraulic properties (eq. (6.1)) compared to the one used for the computation of the thermal properties (see eq. (5.7)) as in Chapter 5 of this thesis.

An alternative approach for estimating ρ_b based on observed m_{soc} has been developed for the Tibetan Plateau by Y. Yang et al. (2009b) and is formulated by:

$$\rho_b = 0.3 + 1.28 \cdot \exp(-0.1724 \cdot m_{soc}) \quad (6.4)$$

Following the additivity hypothesis, the soil hydraulic properties can be estimated as a weighted combination of values for the mineral and organic materials according to Lawrence and Slater (2008) as follows:

$$\theta_s = (1 - f_{t,soc}) \cdot \theta_{s,min} + f_{t,soc} \cdot \theta_{s,soc} \quad (6.5)$$

$$\psi_s = (1 - f_{t,soc}) \cdot \psi_{s,min} + f_{t,soc} \cdot \psi_{s,soc} \quad (6.6)$$

$$b = (1 - f_{t,soc}) \cdot b_{min} + f_{t,soc} \cdot b_{soc} \quad (6.7)$$

where θ_s is the porosity ($\text{m}^3 \text{m}^{-3}$), ψ_s is the soil water potential at air-entry (m), and b is an empirical parameter (-) related to the pore-size distribution of the soil matrix. The hydraulic parameters of the mineral soil (i.e., $\theta_{s,min}$, $\psi_{s,min}$ and b_{min}) can be obtained through a class or continuous pedotransfer function (PTF) given by, for instance, Cosby et al. (1984), while the hydraulic properties of pure organic matter (i.e., $\theta_{s,soc}$, $\psi_{s,soc}$ and b_{soc}) depend on the state of decomposition as described in Letts et al. (2000). The Cosby et al. (1984) class and continuous PTFs applicable for this study, as well as the hydraulic properties for three organic soil types reported in Letts et al. (2000) are given in Appendix A.3 of this thesis. The impact of organic matter on the saturated hydraulic conductivity (K_s) is considered via the Kozeny-Carman equation (eq. (6.9)) as is described in the section below.

6.2.2 Decrease of K_s with depth

Organic matter, living and decayed root systems affect the K_s (Decharme et al. 2006), which can be very high near the surface and enlarge the hydraulic conductivity of the soil. On the other hand, the absence of organic material can reduce the K_s by as much as five orders of magnitude, specifically at deeper layers at 0.4 to 0.8 m where the soil particles are also more closely aligned (Letts et al. 2000). Beven (1982) proposed to estimate the observed decrease of K_s with depth using an exponential relationship, which has been adopted by various LSMs (Chen and Kumar 2001; Decharme et al. 2006; Famiglietti and Wood 1994; Niu et al. 2011; Stieglitz et al. 1997).

The exponential profile of K_s can be described as:

$$K_{s,z} = K_{s,r} e^{-f(z-d_r)} \quad (6.8)$$

where $K_{s,r}$ is the reference saturated hydraulic conductivity (m s^{-1}) at the reference depth d_r (m), while $K_{s,z}$ is the estimated saturated hydraulic conductivity (m s^{-1}) at the soil depth z (m), and f is the exponential profile decay factor (m^{-1}). This formulation can be transformed to a similar expression as introduced by Stieglitz et al. (1997) once d_r is set to 0, as well as into expressions comparable to the ones developed by Chen and Kumar (2001) and Decharme et al. (2006) if d_r is set to the depth at which the compacted value $K_{s,r}$, provided in Clapp and Hornberger (1978), is reached. The $K_{s,r}$ can also be indirectly estimated by the Kozeny-Carman equation using both porosity (θ_s)

and the slope (b) of the water retention curve at the reference depth as follows (Ahuja et al. 1984; Saxton and Rawls 2006):

$$K_{s,r} = C_e \cdot (\theta_{s,r} - \theta_{33,r})^{3-1/b} \quad (6.9)$$

where θ_{33} is the water content ($\text{m}^3 \text{m}^{-3}$) at -33 kPa matric potential, and C_e is an empirically derived constant and herein taken as 1930 mm h^{-1} from Saxton and Rawls (2006). Besides the exponential function, the impact of organic matter on K_s can also be indirectly accounted for by combining eq. (6.9) with above eqs. (6.5)-(6.7).

The f factor in eq. (6.8) can be estimated indirectly through calibration against measured streamflow recession curves or directly from in-situ measurements that capture the K_s decline as a function of depth (Chen and Kumar 2001). At large scale, the f is usually obtained via the first approach and Niu et al. (2011) found that a value of 6 m^{-1} is appropriate for global applications based on calibration against stream flow measurements collected worldwide.

6.2.3 Root distribution

As described in Section 3.2.3 of Chapter 3, the Noah LSM assumes by default a uniform vertical distribution of the root across the soil profile (see eq. (3.41)). In reality this is, however, hardly ever the case. Especially for the Tibetan Plateau there have been reports (van der Velde et al. 2009; Yang et al. 2005) on a very dense distribution of roots in the top 10 cm whereas the roots are sparse in the deeper soil layers. Through the one-parameter asymptotic function proposed by Gale and Grigal (1987), such a vertical distribution of the roots can be considered as:

$$Y = 1 - \beta^d \quad (6.10)$$

where Y is the cumulative root fraction from the soil surface to depth d (cm), and β is an empirical parameter (-). Jackson et al. (1996) estimated the β parameter from the measured root distribution for each biome across the globe and for the Tibetan Plateau Y. Yang et al. (2009a) more recently reported values of 0.937 for alpine steppe and 0.900 for alpine meadow. The latter is applicable for this study.

The uniform root distribution implemented in the current Noah LSM can be replaced with above asymptotic function as follows:

$$f_{root,i} = Y_i - Y_{i-1} \quad (6.11)$$

$$Y_i = (1 - \beta^{d,i}) / (1 - \beta^{d,root}) \quad (6.12)$$

The total rooting depth can be defined as the depth at which the cumulative root fraction Y reaches an arbitrary value herein taken as 99 % (Zeng 2001), and thus the total number of root layers (n_{root}) as well as its vertical distribution are known.

6.2.4 Modified soil water flow scheme implementation

The current implementation of the diffusivity form of Richards' equation in Noah (see eq. (3.31)) is not able to simulate water flow across a vertically heterogeneous soil profile. As such, the model code is firstly revised to enable the assignment of different hydraulic parameters for each soil layer. Specifically, the soil hydraulic parameters (i.e., θ_s , ψ_s and b) of each soil layer are calculated as the weighted combination of values for mineral and pure organic materials (eqs. (6.5)-(6.7)), and the exponential profile of K_s (eq. (6.8)) is utilized as well.

Secondly, the implementation of Richards' equation is modified to mitigate the discontinuity in the soil water content at the interface of two soil layers with different hydraulic properties. This is accomplished via the solution provided by Hills et al. (1989) through adding a term to the Crank-Nicolson scheme (see eq. (3.32)):

$$\Delta z_i \frac{\theta_i^{n+1} - \theta_i^n}{\Delta t} = D_i^{n+1} \frac{\theta_{i+1}^{n+1} - \theta_i^{n+1}}{z_{i+1} - z_i} - D_{i-1}^{n+1} \frac{\theta_i^{n+1} - \theta_{i-1}^{n+1}}{z_i - z_{i-1}} - (K_i^{n+1} - K_{i-1}^{n+1}) + \Delta z_i \cdot S_i - (D_i^{n+1} \frac{\Delta \theta_{a,i}^{n+1}}{z_{i+1} - z_i} - D_{i-1}^{n+1} \frac{\Delta \theta_{a,i-1}^{n+1}}{z_i - z_{i-1}}) \quad (6.13)$$

where n and i represent the time and spatial step separately, Δt represents the time step (s), Δz represents the depth of the soil layer (m), z represents the position of the mid-point of the soil layer (m), θ is the soil moisture content ($\text{m}^3 \text{m}^{-3}$), D is the soil water diffusivity ($\text{m}^2 \text{s}^{-1}$), K is the hydraulic conductivity (m s^{-1}), S represents sources and sinks (i.e., precipitation and evapotranspiration, m s^{-1}), and $\Delta \theta_a$ is introduced to account for the discontinuity in the soil water content across the interface of two soil layers, defined as:

$$\Delta \theta_{a,i} = \theta_{s,i} \cdot (\psi_{a,i} / \psi_{s,i})^{-1/b_i} - \theta_{s,i+1} \cdot (\psi_{a,i} / \psi_{s,i+1})^{-1/b_{i+1}} \quad (6.14)$$

where ψ_a is the soil water potential at the interface and can be estimated as:

$$\psi_{a,i} = \frac{(K_i - K_{i+1}) + 2K_i \cdot \psi_i / \Delta z_i + 2K_{i+1} \cdot \psi_{i+1} / \Delta z_{i+1}}{2K_i / \Delta z_i + 2K_{i+1} / \Delta z_{i+1}} \quad (6.15)$$

6.3 Estimation of soil hydraulic properties

6.3.1 Bulk density and porosity

From Section 6.2.1 three methods can be deduced for calculating the bulk density (ρ_b) based on the measured organic carbon mass content (m_{soc}): using eqs. (6.2)-(6.3) with the porosity for the mineral soil ($\theta_{s,min}$) adopted from either Cosby's i) class (hereafter 'SOC+class') or ii) continuous PTF (hereafter 'SOC+continuous'), and iii) the empirical approach proposed by Y. Yang et al. (2009b) (eq. (6.4), hereafter 'Y09b'). The porosity (θ_s) can be estimated by Cosby's i) class and ii) continuous PTF disregarding the contribution of organic matter content. On the other hand, the impact of organic matter on θ_s can also be accounted for via eq. (6.5) with the $\theta_{s,min}$ adopted from either Cosby's iii) class (SOC+class) or iv) continuous PTF (SOC+continuous), and the porosity of a organic soil ($\theta_{s,soc}$) given in Letts et al. (2000), which taken equal to $0.83 \text{ m}^3 \text{ m}^{-3}$ due to the similarity between the soil water retention curve of organic soil in this study and that for Sapric peat (shown in the following section). The organic fraction ($f_{t,soc}$) in eq. (6.5) is estimated by eqs. (6.1)-(6.3) based on the measured m_{soc} .

This study applies the methods for estimating the θ_s and ρ_b to two soil property datasets collected across the Tibetan Plateau. The first is based on the measurements around the Maqu station described in Section 2.2.2 of Chapter 2, and the second is reported in Chen et al. (2012) that constitutes of samples from four sites situated in the central and eastern parts of the Plateau. Table 6.1 gives the error statistics following from the comparison of the measured and estimated ρ_b and θ_s , i.e., the coefficient of determination (R^2), mean error (ME) and root mean squared error (RMSE). With R^2 values larger than 0.89, the error statistics indicate that all three methods are capable of providing reasonable ρ_b estimates. Although with the ρ_b estimates obtained via Y09b comparable or better R^2 values are obtained, the ME and RMSE achieved with the methods proposed in this study are significantly lower, on absolute average 0.013 versus 0.104 g cm^{-3} for the ME and 0.145 versus 0.169 g cm^{-3} for the RMSE. In this regard, the continuous PTF performs slightly better than the class PTF. Apparently, the reliability of ρ_b estimates benefits from the within class variability embedded within the continuous PTF.

The error statistics associated with the θ_s determination reveals a somewhat mixed performance. The θ_s estimates produced with the standard Cosby's class and continuous PTFs yield with a R^2 ranging from 0.281 up to 0.607 and RMSE values as high as $0.196 \text{ m}^3 \text{ m}^{-3}$. However, with consideration of the soil organic

matter content via the additivity approach this improves significantly to a R^2 better than 0.915 and a RMSE varying from 0.028 to 0.068 $\text{m}^3 \text{m}^{-3}$. To investigate this further Table 6.2 provides correlation coefficients calculated among θ_s , ρ_b and m_{soc} , as well as soil texture (i.e., percentage of sand, clay and silt) for both soil datasets combined. The θ_s as well as ρ_b have clearly much stronger relationship with m_{soc} than other soil texture components. This explains why the Cosby's PTFs with explicit consideration of organic matter outperforms the standard approach. Hence, it can be concluded from this analysis that including the m_{soc} within a PTF is imperative for providing a robust θ_s estimate, at least, for Tibetan soils.

Table 6.1: Coefficient of determination (R^2), mean error (ME) and root mean square error (RMSE) between measured and estimated bulk density (ρ_b) and porosity (θ_s) using the data collected around Maqu station and the data from Chen et al. (2012)

Property	Method	Maqu data			Chen's data		
		R^2	ME	RMSE	R^2	ME	RMSE
ρ_b (g cm^{-3})	SOC+class	0.944	-0.021	0.099	0.893	-0.016	0.199
	SOC+continuous	0.943	0.012	0.093	0.914	-0.001	0.189
	Y09b	0.943	-0.073	0.122	0.924	-0.134	0.215
θ_s ($\text{m}^3 \text{m}^{-3}$)	class PTF	0.553	-0.105	0.148	0.363	-0.118	0.180
	continuous PTF	0.607	-0.127	0.164	0.281	-0.133	0.196
	SOC+class	0.973	0.004	0.030	0.932	0.005	0.068
	SOC+continuous	0.971	-0.009	0.028	0.916	0.011	0.066

Table 6.2: Correlation coefficients calculated among porosity (θ_s), bulk density (ρ_b), soil organic carbon content (m_{soc}) and soil particle size distribution

	θ_s	ρ_b	m_{soc} (%)	Sand (%)	Clay (%)	Silt (%)
θ_s ($\text{m}^3 \text{m}^{-3}$)	-	-0.932	0.754	-0.340	0.051	0.385
ρ_b (g cm^{-3})	-0.932	-	-0.775	0.273	-0.024	-0.317

6.3.2 Soil water retention curve

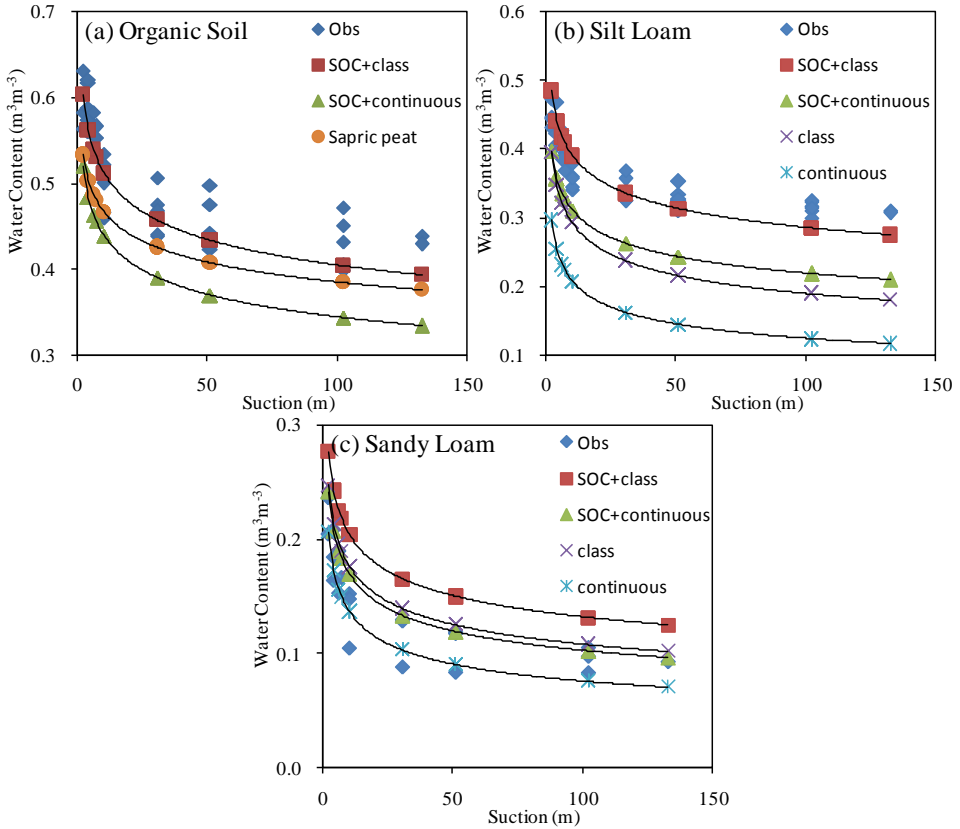


Figure 6.1: Comparison of the observed and estimated soil water retention curves for (a) organic soil, (b) silt loam and (c) sandy loam deduced from Cosby’s class or continuous PTF without and with consideration of the soil organic content (SOC).

Figure 6.1 shows for the three soil types (organic soil, silt loam and sandy loam) the soil water retention measurements as well as estimates of the retention curve with soil hydraulic model proposed by Campbell (1974) (see eq. (3.33)). Specifically, the soil data given in Table 2.2 of Chapter 2 is regrouped by soil texture. Comparable to the previous section, the hydraulic parameters (e.g., θ_s , ψ_s and b) are for both organic and mineral soils deduced from Cosby’s class and continuous PTFs without and with consideration of the m_{soc} as described in Section 6.2.1. Again, the Sapric peat parameterization reported in Letts et al. (2000) is adopted to represent the hydraulic characteristics of pure organic matter. It should be noted that Figure 6.1a for the organic soils shows for clarity

the retention curve produced with only Letts's Sapric peat parameterization instead of the two curves obtained with Cosby's class and continuous PTFs. It shows that the retention curve for the organic soils in this study is comparable to that for Sapric peat.

Table 6.3 lists for each soil type the mean m_{soc} , percentages sand and clay as well as the RMSE computed between the measured and estimated soil water content. This table shows that the m_{soc} of sandy loam soils is much lower than for other two types, which can be attributed to the fact that the sandy loam soils in the Maqu region are mostly present in deeper layers (see Table 2.2 of Chapter 2). The RMSEs reported in Table 6.3 as well as the plots of Figure 6.1 highlight that the Cosby's class PTF with consideration of organic matter (SOC+class) provides the best estimates of the soil water retention measurements for the organic and silt loam soils. The obtained RMSEs are 0.034 and 0.027 $\text{m}^3 \text{m}^{-3}$ for the organic and silt loam soils, respectively, versus RMSEs of respectively 0.090 and 0.078 $\text{m}^3 \text{m}^{-3}$ achieved with the SOC+continuous parameterization as the runner up.

Table 6.3: Averaged feature of soil properties regrouped by soil type, as well as RMSE between measured and estimated soil water contents associated with different pressure heads

Soil Type	m_{soc} (%)	Sand (%)	Clay (%)	RMSE ($\text{m}^3 \text{m}^{-3}$)			
				class	continuous	SOC+class	SOC+continuous
Organic Soil	15.31	27.47	8.35	0.232	0.316	0.034	0.090
Silt Loam	3.44	30.12	9.70	0.097	0.176	0.027	0.078
Sandy Loam	0.70	58.13	6.36	0.031	0.022	0.055	0.026

In contrast to the ρ_b results, the SOC+class parameterization outperforms the SOC+continuous estimates of the retention curve. Apparently, the empirical shape parameter, b , and the ψ_s provided by Cosby's continuous PTF are less representative for the organic and silt loam soils studied here. This is confirmed by the large RMSEs obtained with the continuous parameterization in comparison to the results with the class parameterization. On the other hand, better results are achieved with Cosby's continuous PTF for the sandy loam

soils, for which also the inclusion of m_{soc} in the estimation of the retention curve somewhat reduces its accuracy. This suggests that consideration of the m_{soc} for estimation of the retention curve is only beneficial if the soil includes a significant amount of organic matter. Otherwise uncertainties following from inaccuracies in the m_{soc} determination become relatively large.

6.3.3 Saturated hydraulic conductivity

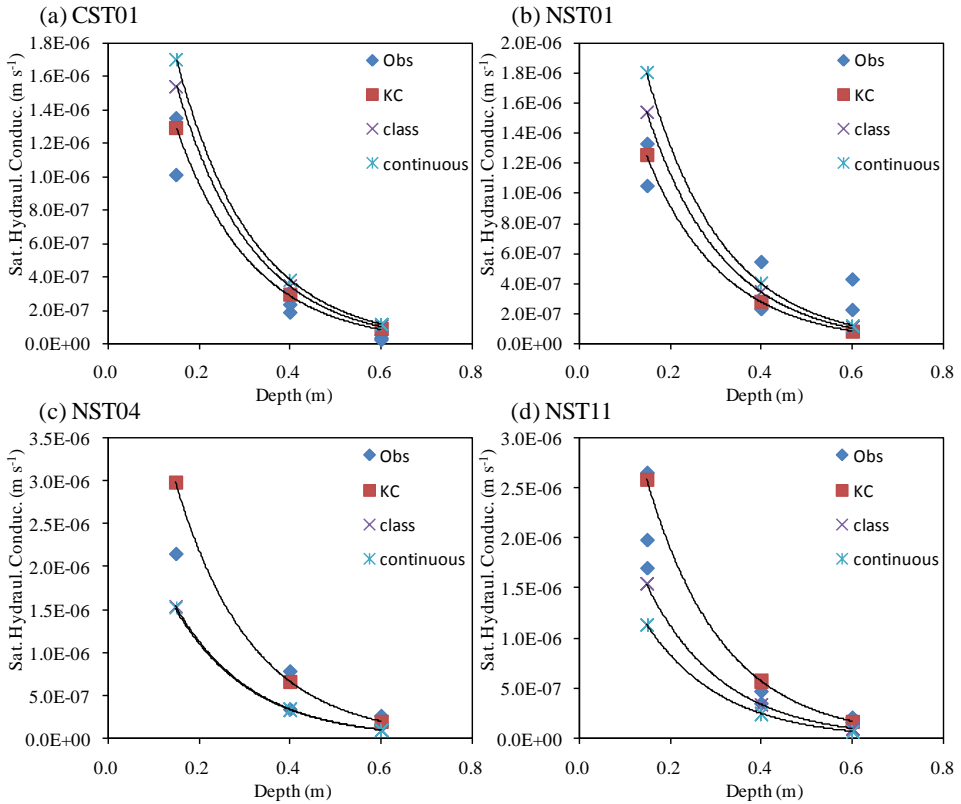


Figure 6.2: Comparison of the observed and estimated saturated hydraulic conductivity as an exponential function of soil depth carried out for four SMST sites. *Obs* stands for the laboratory measurements, *KC*, *class*, and *continuous* stand for the estimates obtained with the Kozeny-Carman equation, Cosby's class and continuous pedotransfer function.

Figure 6.2 shows the in-situ saturated hydraulic conductivity (K_s) measurements as a function of soil depth carried out around the four SMST stations. In addition, K_s -soil depth relationships are plotted that are estimated with the approach by Beven (1982), eq. (6.8), whereby the exponential decay

factor (f) is taken equal to 6 m^{-1} as suggested by Niu et al. (2011). The required reference saturated hydraulic conductivity ($K_{s,r}$) is estimated here using Cosby's i) class or ii) continuous PTF with the reference depth (d_r) set at 0.05 m (i.e., the mid-point of first layer in the Noah LSM), as well as via iii) the Kozeny-Carman equation (eq. (6.9), hereafter 'KC') with the unknown hydraulic parameters adopted from Cosby's class PTF with consideration of organic matter as described in Section 6.2.2.

The measurements indicate that in general the K_s decreases by one to two orders of magnitude over a soil depth from 0.15 m to 0.6 m. The reason for this is that organic matter and plant roots are abundant in the upper soil layers (see Table 2.2) affecting the soil aggregation and associated pore space distribution that leads to higher water holding capacity and conductivity compared with lower soil layers. Further, it should be noted that the K_s values for the two wetland sites (NST04 and NST11) are comparable to the other two grassland sites, which suggests that a higher m_{soc} does not necessarily imply a larger K_s . This is in agreement with earlier findings of, for instance, Nemes et al. (2005) who concluded that organic matter retains water well, which limits the hydraulic conductivity. Moreover, according to Carey et al. (2007), the K_s is typically constrained by the pore segments with the smallest diameter that may form only a small fraction of the total pore size distribution of organic soils.

The implementation of Beven's approach for describing the K_s as a function of soil depth which matches the measurements best is the one that uses the Kozeny-Carman equation. The most notable differences are obtained near the soil surface where the K_s is largest and, thus, the flow of water through the soil is largest. The implementations with Cosby's class and continuous PTFs typically overestimate the K_s for the mineral soils (CST01 and NST01), while they underestimate K_s for the organic soil wetland sites (NST04 and NST11). It should, however, be noted that the Kozeny-Carman estimate of K_s for the wetland NST04 site overestimates the measurements, but falls within the measured K_s range for the other wetland site (NST11).

6.4 Simulation of soil moisture with the Noah LSM

6.4.1 Design of numerical experiments

Three experiments are designed to assess the impact of the augmentations to the default Noah LSM described in Section 6.2. A control experiment (hereafter 'Ctrl') is performed firstly by running the Noah LSM with the default soil hydraulic and root uptake scheme as described in Section 3.2 of Chapter 3. Secondly, the default hydraulic scheme is replaced with the soil organic scheme,

see Section 6.3, and the modified diffusivity form of Richards' equation (eq. (6.13)) that resolves the soil moisture discontinuity at the interface of two layers, see Section 6.2.4 (hereafter 'EXP1'). Thirdly, the distribution of roots in the soil profile is implemented as a function of depth following eqs. (6.11)-(6.12) instead of the default uniform distribution (hereafter 'EXP2').

All the experiments are forced by the meteorological measurements collected at the Planetary Boundary Layer (PBL) tower from 8 June 2010 to 30 September 2010 and include air temperature, relative humidity, wind speed, air pressure, downward and upward shortwave radiations, downward longwave radiation and precipitation (see Table 2.1 of Chapter 2). The observation height of the air temperature and wind speed is 2.35 m. The prescribed vegetation type is grassland, and the monthly values of green vegetation fraction (*GVF*) and leaf area index (*LAI*) are derived from the SPOT ten-daily synthesis *NDVI* product as in Chapter 5. The other vegetation parameters (e.g., number of root layers) are obtained from Noah's default land cover database. The parameter β for EXP2 is taken as the value (i.e., 0.900) for the alpine meadow reported in Y. Yang et al. (2009a) and, then, the number of root layers is computed using the method described in Section 6.2.3.

The silt loam is adopted as soil texture according to measured properties (see Table 2.2) found at the upper layers of the two SMST sites (CST01 and NST01) near the PBL tower. Corresponding hydraulic parameters for Ctrl are obtained using Cosby's class PTF. The m_{soc} of each soil layer for EXP1 and EXP2 is taken as the average of the value derived from measurements collected at the CST01 and NST01 sites and Sapric peat data from Letts et al. (2000) are adopted to represent the hydraulic parameters for pure organic matter. Beven's approach for describing the K_s as a function of soil depth is implemented by EXP1 and EXP2, and the reference saturated hydraulic conductivity ($K_{s,r}$) is estimated via the Kozeny-Carman equation (eq. (6.9)), see Section 6.3.3. Further, it should be noted that the K_s value of the bottom (fourth) layer is set equal to that for the third layer as the decrease of K_s with depth is limited for the deep layers. Similarly, the m_{soc} value of the bottom layer is set equal to that for the third layer as well.

Soil moisture and temperature measurements are used to initialize each model run as well as to validate Noah simulations. For both, the measurements collected at sites CST01 and NST01 are averaged for each soil depth (e.g., 0.05, 0.10, 0.20, 0.40 and 0.80 m), and subsequently interpolated to the mid-points of the upper three model layers (i.e., 0.05, 0.25 and 0.70 m). Then the soil moisture and temperature of the fourth layer is taken for initialization equal to

the states of the third layer. The Noah simulations are validated further through comparisons of the simulated latent (LE) and sensible (H) heat flux with measurements collected by an eddy-covariance (EC) system.

6.4.2 Noah soil moisture simulations

Figure 6.3 shows time series with a 30-min interval of the measured soil moisture and the simulations produced by the above described three numerical experiments along with the measured rainfall. The upper, mid and lower panels provide the measurements and simulations for soil depths of 5, 25, and 70 cm, respectively. Three distinct dry-down episodes (periods in which soil moisture gradually deplete) can be deduced from Figure 6.3a, e.g., i) DOYs 159-179, ii) DOYs 204-224, and iii) DOYs 244-264 with corresponding wetting periods (i.e., DOYs 179-204, DOYs 224-244 and DOY 264- onwards). The default configuration of the Noah LSM (Ctrl) tends to underestimate the soil moisture especially for the two upper soil layers. For the top layer the soil moisture underestimation is most notable under wet conditions, while below a soil moisture content of $0.25 \text{ m}^3 \text{ m}^{-3}$ the underestimation changes into an overestimation.

The inability to accurately simulate the surface soil moisture over the Tibetan Plateau has also been recently reported for other LSMs (Y. Chen et al. 2013; Su et al. 2013; Xue et al. 2013). Yang et al. (2005) and Y. Chen et al. (2013) attributed this to the absence of a soil stratification linked to specifically organic matter within model structures. Indeed, the underestimation of surface soil moisture significantly improved during the wetting periods after implementing the soil organic scheme (EXP1). The explanation for this is that the relative abundance of organic matter in the upper layers leads to a larger soil porosity and higher water holding capacity. Consequently, the EXP1 simulation tends to retain water in the upper layers, which causes an overestimation of soil moisture in the upper layers during dry downs. This is further enhanced by the exponential K_z decay as a function of depth, which reduces the convective and diffusive flow components toward the deeper layer via the transport coefficients, K and D , and suppresses the redistributed soil water across soil layers (Braun and Schädler 2005).

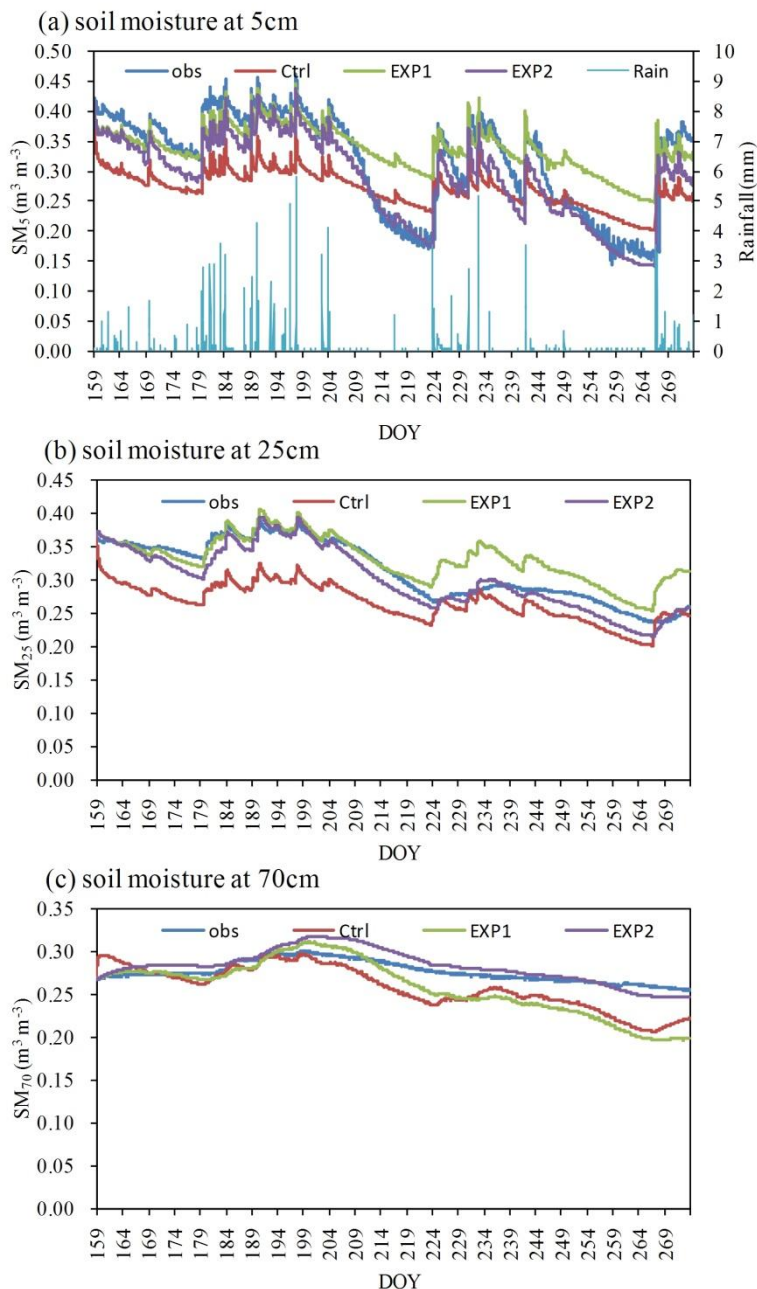


Figure 6.3: Comparison of the observed and simulated soil moisture produced by three Noah numerical experiments for each soil layer during 8 June 2010 and 30 September 2010.

As such, the augmentations implemented for EXP1 enables the Noah model to better simulate the soil moisture content during wet episodes, but it does not lead to an improvement for the dry-downs. The soil moisture results following from the EXP2 simulation show that this can be associated with the default uniform root distribution implemented in Noah. This assumed that the root fraction (f_{root}) in each layer is proportional to the layer thickness, which leads to more root uptake from the deeper (lower) soil layers. In reality, however, the majority of the plant roots are located in the upper soil layer of Tibetan ecosystems (Y. Yang et al. 2009a). Hence, both Ctrl and EXP1 overestimate during dry-downs the soil moisture content of the upper soil layers (i.e., 0.05 m and 0.25 m) and underestimate it for the lower soil layers (i.e., 0.70 m). Implementation of the root distribution as an asymptotic function of depth (eqs. (6.11)-(6.12)) allows Noah (EXP2) to take up more water for transpiration from the upper soil layers. This modification to the model structure enables the soil moisture simulations to capture much better the dynamics measured at each soil depth also under dry down conditions as can be seen in Figure 6.3.

Table 6.4: Error statistics computed between measurements and simulated soil moisture produced by three Noah numerical experiments for the period between 8 June 2010 and 30 September 2010

Exp eri men t	SM_5 ($m^3 m^{-3}$)			SM_{25} ($m^3 m^{-3}$)			SM_{70} ($m^3 m^{-3}$)		
	R^2	ME	RMS E	R^2	ME	RMS E	R^2	ME	RMS E
Ctrl	0.80	-0.046	0.07	0.77	-0.047	0.05	0.61	-0.018	0.03
EX P1	0.81	0.021	0.06	0.76	0.019	0.03	0.84	-0.018	0.03
EX P2	0.92	-0.028	0.04	0.94	-0.011	0.02	0.92	0.007	0.01

Table 6.4 gives the error statistics (i.e., R^2 , ME and RMSE) between the measured and simulated soil moisture produced by the three experiments. The error statistics confirm improvement in the soil moisture simulation achieved by EXP1 and EXP2 model runs in comparison to Ctrl. The R^2 calculated for the difference between the measurements and simulations increased on average for the three soil depths (0.05 m, 0.25 m and 0.70 m) from 0.73 for Ctrl, 0.8 for EXP1 to 0.93 for EXP2. This clearly highlights that the EXP2 simulations are

superior in capturing the soil moisture dynamics. This is further supported by reductions in the ME by about 39, 77 and 61 % and RMSE by 49, 70 and 56 % in comparison to the Ctrl error statistics for the three soil depths, respectively.

6.5 Discussion

6.5.1 Impact on surface energy budget simulations

Soil moisture plays an important role in the energy balance by controlling the partitioning of the surface energy budget into the sensible heat flux (H) and the latent heat flux (LE). Below critical soil moisture levels, evaporation is suboptimal and the radiation excess is converted into heat. Soil moisture also affects the soil heat conductivity and the soil heat capacity that influences the transport of heat into the soil (G_0). The accuracy of the simulated soil moisture will, therefore, have inevitably an impact on the simulations of the heat fluxes and soil temperatures.

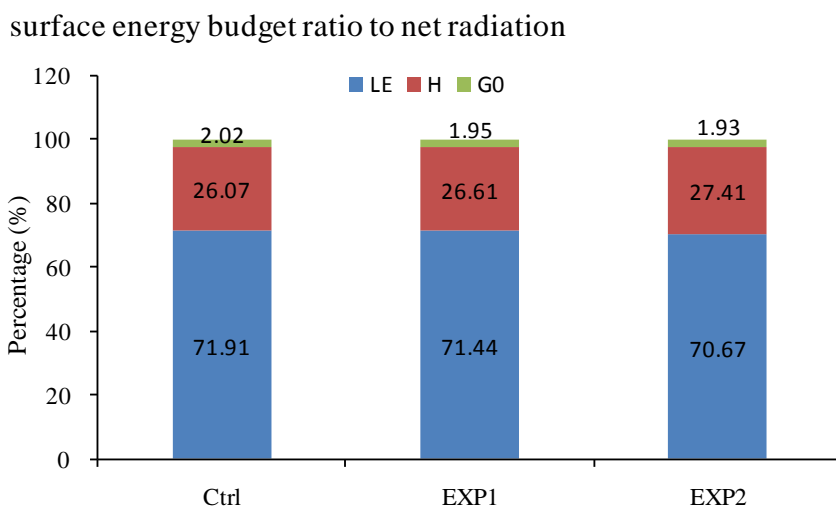


Figure 6.4: Partitioning of the surface energy budget into latent (LE), sensible (H) and ground (G_0) heat fluxes produced by three Noah numerical experiments (Ctrl, EXP1 and EXP2) presented as a ratio of the net radiation (R_n) accumulated for the study period from 8 June 2010 to 30 September 2010.

Figure 6.4 shows the partitioning of the surface energy budget into LE , H and G_0 produced by the three Noah runs (Ctrl, EXP1 and EXP2) presented as a ratio of the net radiation (R_n), whereby the heat fluxes are accumulated over the entire study period. In general, LE is the dominant component of the surface

energy budget for the selected simulation period and little differences are noted in the energy partitioning between the three Noah runs. To support the analysis Figure 6.5 shows the mean diurnal cycle of the measured and simulated sensible and latent heat fluxes for the months June, July, August and September, which confirms the little impact of the soil water flow physics on the simulated surface heat flux. The reason for this is that the LE in the selected study area is primarily driven by the available energy during the wet monsoon season. Hence, all three numerical experiments generate soil moisture profiles that sustains the production of non-water limited LE , while they do perform significantly different in redistributing the total transpiration and soil water extraction across the soil profile (see Figure 6.3). Nevertheless, it is noted that the measured H is overestimated by about 20 up to 40 $W\ m^{-2}$ during midday for each of the three Noah runs, whereas fairly small systematic differences are observed between the simulated and measured LE .

Table 6.5 gives the error statistics (i.e., RMSE and ME) computed between the measured and simulated heat fluxes (e.g., LE and H) and soil temperature (e.g., surface and 25 cm) for the study period at a 30-min time step. Overall, the statistics indicate that the heat fluxes produced with Noah are reasonable (also shown in Figure 6.5) with RMSE values for the LE on the order of 30 $W\ m^{-2}$, and also confirm the small differences among the three numerical experiments. It should, however, be noted that Noah somewhat overestimates heat fluxes and soil temperature, which can be associated with the energy closure problem of EC observations as described in Zheng et al. (2014). Moreover, the RMSE computed for the heat fluxes (i.e., H and LE) increased upon implementation of each set of augmentations, from Ctrl, EXP1 to EXP2, because less LE is produced, and more H and G_o (see Figure 6.4). This can be attributed to the definitions of wilting soil moisture (θ_w) and critical soil moisture (θ_c) as well as the vegetation parameters that control the soil water stress imposed on the soil evaporation and vegetation transpiration within Noah. Indeed, van der Velde et al. (2009) have shown that through modification of the vegetation parameterization large improvements can be obtained in the simulation of the heat fluxes and particularly the LE . However, further work is needed to assess the suitability of Noah's LE parameterization for the Tibetan Plateau ecosystems.

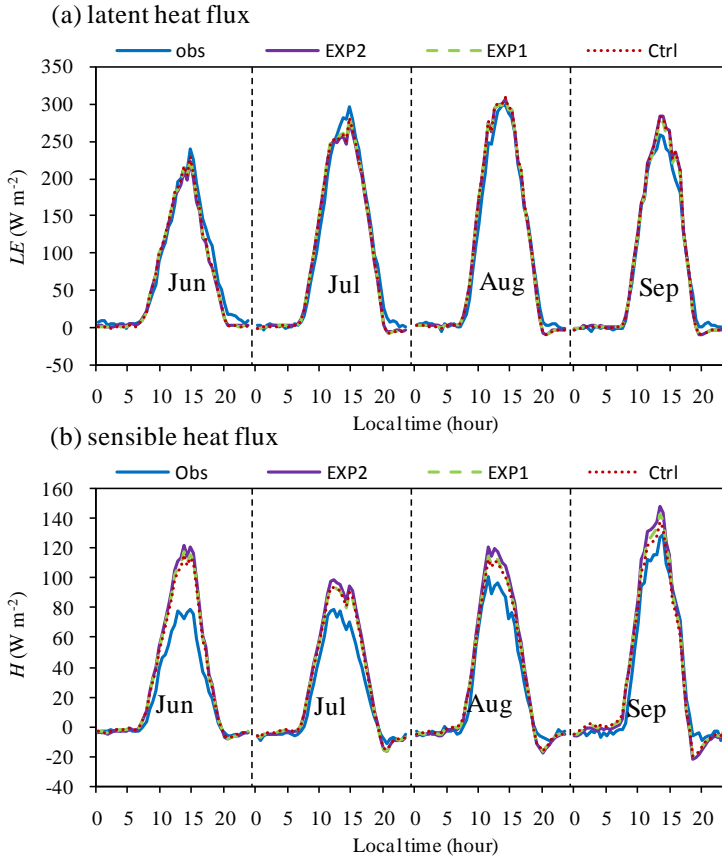


Figure 6.5: Average diurnal cycles for the months June, July, August and September of the measured and simulated (a) latent heat flux and (b) sensible heat flux produced by three Noah numerical experiments.

Table 6.5: Error statistics computed between measurements and simulations of the latent (LE) and sensible (H) heat fluxes as well as surface (T_{sfc}) and 25-cm soil (T_{s25cm}) temperature for three Noah numerical experiments for the period between 8 June 2010 and 30 September 2010

Numerical Experiment	H ($W\ m^{-2}$)		LE ($W\ m^{-2}$)		T_{sfc} (K)		T_{s25cm} (K)	
	RMSE	ME	RMSE	ME	RMSE	ME	RMSE	ME
Ctrl	17.48	6.84	31.06	0.65	2.56	1.20	1.03	0.86
EXP1	18.29	7.70	30.96	0.04	2.62	1.20	1.11	0.92
EXP2	19.86	9.15	31.45	-1.11	2.70	1.20	1.01	0.86

6.5.2 Impact on surface water budget simulations

Apart from its influence on the surface energy balance, soil moisture has also an effect on the simulated water budget by i) determining the rainfall-runoff response through partitioning of precipitation into surface runoff (R_s) and infiltration, ii) defining the drainage (R_b) through the soil column towards deeper layers, and iii) limiting the actual evapotranspiration (ET_a) in case of soil water stress (see also the previous section). The impact of the augmentations made to the Noah model structure on the simulated water budget is illustrated by Figure 6.6, in which the ratios of the different water budget components are shown. These ratios are calculated by dividing the total simulated ET_a , R_s , R_b and change in soil water storage (ΔW_s) by the total rainfall measured from 8 June to 30 September 2010.

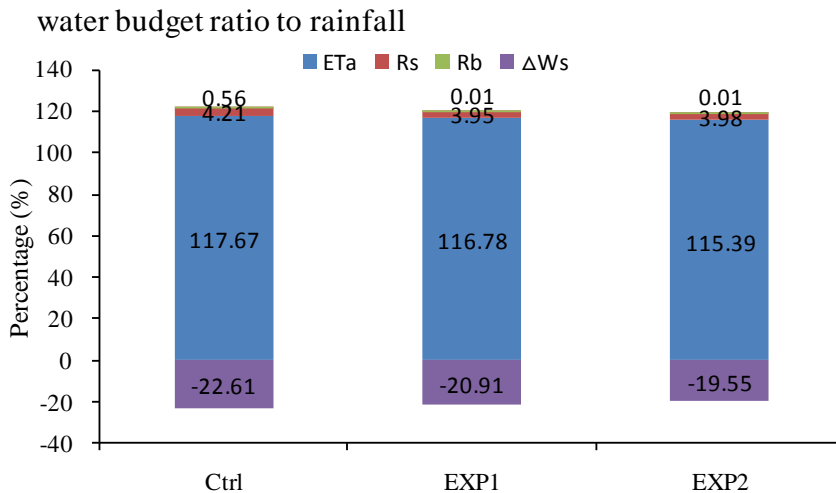


Figure 6.6: Comparison of the ratios of different water budget components produced by three Noah numerical experiments (Ctrl, EXP1 and EXP2) presented as a ratio of the rainfall accumulated for the study period from 8 June 2010 to 30 September 2010.

Figure 6.6 shows in analogy with the simulated surface energy budgets (Figure 6.4) that all three Noah runs produce comparable water budgets, and that the ET is the dominant contribution. In comparison with the Ctrl run, Noah partitions with the EXP2 setup less solar energy into ET_a (or LE). This leads to less water being extracted from the soil for evapotranspiration (i.e., lower ratio of ET_a), which explains the higher ΔW_s ratio for EXP1 and EXP2 to lesser

extent. Further, the implementation of the exponentially decaying of K_s with depth (i.e., EXP1 and EXP2) reduces the drainage component. Also, the R_s is lower for EXP1 and EXP2, which can be attributed to the consideration of organic matter that increases the water holding capacity of the soil. In summary, the modifications made to the Noah model structure lead to more water retained in the soil column at the expense of the other water balance components (e.g., ET_a , R_s and R_b).

6.6 Conclusions

This study investigates the ability of the Noah land surface model (LSM) to simulate the soil water flow in the high altitude Source Region of the Yellow River (SRYR) through comparison with soil moisture profiles measured during the monsoon season. Noah with its default model structure underestimates the soil moisture content of the top layer under wet conditions and overestimates it during dry-down episodes, whereas the moisture contents in the deeper soil layers are systematically underestimated. Three augmentations to the model physics are investigated to remediate these deficiencies: i) the impact of organic matter is considered on the soil water retention curve via the additivity hypothesis, ii) the saturated hydraulic conductivity (K_s) is implemented as an exponentially decaying function with soil depth, and iii) the vertical root distribution is modified to better represent the Tibetan alpine grassland conditions characterized by an abundance of roots in the top soil layer. Further, the diffusivity form of Richards' equation is revised to allow for the simulation of the soil water flow across soil layers with different hydraulic properties.

The modified hydraulic parameterization is compared against laboratory measurements of the soil water retention curve and in-situ K_s measurements. It is shown that through consideration of organic matter within the class pedotransfer function (PTF) by Cosby et al. (1984), the default option in Noah, the root mean squared error (RMSE) computed between the estimated and measured porosity (θ_s) improved by more than 80 % from 0.148 to 0.030 $\text{m}^3 \text{m}^{-3}$. This leads to similar improvements in the estimated soil water retention curves of the organic and silt loam soils in the SRYR, whereas a slightly reduced performance is noted for the sandy loam soils. The latter is attributed to the fact that the sandy loam soils have little organic matter contents and, thus, usage within the parameterization primarily adds uncertainty to the estimates. The K_s measurements taken in-situ at various soil depths show a decrease by as much as two orders of magnitude across a soil depth from 0.15 to 0.6 m, which is

described best with the exponential function combined with the Kozeny-Carman equation.

Three numerical experiments are designed to assess the impact of the augmentations: i) a control run with the default model structure (Ctrl), ii) a Noah run with the modified soil hydraulic parameterization (EXP1), and iii) a Noah run with the modified soil hydraulic parameterization and vertical root distribution (EXP2). Through implementation of the modified hydraulic parameterization alone (EXP1) the soil moisture underestimation in the upper soil layer under wet conditions is resolved, whereas the overestimation during dry-downs remains. This somewhat improves the simulations for the deeper soil layers but not to its full extent. By including the modified root distribution in the soil profile also the soil moisture dynamics of the upper layer under dry conditions are better captured and the simulations of the deeper layers match better with the measurements as well. This leads to a reduction in the RMSE computed between the simulated and measured soil moisture by about 49, 70 and 56 % for the upper three layers.

The impact of the improved soil moisture simulations on the calculated surface energy and water budgets is assessed, and shows that Noah retains more water in the soil column with the augmentations causing a decrease in the other water balance components. On the other hand, the surface heat flux simulation is hardly affected. This is attributed to the fact that LE in the selected study area and period is primarily constrained by the energy rather than the available soil water.

This study shows through comprehensive measurements performed in the laboratory and field that significant improvements can be achieved in the soil water flow simulation by the Noah LSM for a Tibetan Plateau site through a better representation of the hydraulic parameters and the root distribution across the soil profile. This further confirms the necessity to incorporate the impact of vertical soil heterogeneity caused by organic matter and root systems into state-of-the-art LSMs for their application to the Tibetan Plateau (Y. Chen et al. 2013; Xue et al. 2013; Yang et al. 2005). This study can also be seen as an attempt to investigate the transferability of LSM parameterizations developed for the Polar and Boreal organic soils (Lawrence and Slater 2008; Letts et al. 2000) to the Third Pole Environment (i.e., Tibetan Plateau). Additional work is, however, needed to extend the findings of this study to large spatial domains. The soil property datasets (e.g., soil particle size distribution, soil organic carbon) recently developed for China as well as the globe (Shangguan et al. 2012; 2014; 2013) can, for instance, be utilized for such application.

Chapter 7 Impact of model physics on catchment scale runoff simulation*

7.1 Introduction

The Asian water towers, originating from the Himalayas and adjacent Tibetan Plateau, are threatened by a projected decline in the water availability as a result of climate change (Immerzeel et al. 2010). Many previous studies (e.g., Gao et al. 2012; Immerzeel et al. 2010; Lutz et al. 2014) have used hydrological models for quantifying the water fluxes and the projection of the water availability across the Tibetan Plateau. A substantial part of the Plateau is, however, underlain with permafrost and/or subject to seasonally frozen ground, which makes the freeze-thaw process as one of the key components for understanding the surface hydrology of this region. The presence of ice dramatically changes the soil hydraulic and thermal properties (Farouki 1986; Zhang et al. 2008; 2010) that, in turn, affects the water and heat fluxes (Gouttevin et al. 2012; Li et al. 2010; Viterbo et al. 1999). While hydrological models constrain the hydraulic conductivity of frozen ground, the implication of phase transition on the energy budget is typically neglected. Likewise, various warm season ‘soil’ and ‘above ground’ heat transfer processes are not included in the structure of hydrological models. Such incomplete treatment of both cold and warm season energy processes forms a source of uncertainty (Luo et al. 2003) that may particularly be important for high-altitude regions, such as the Tibetan Plateau.

The land surface modeling community, on the other hand, has made significant progress in developing model physics for the effects of the freeze-thaw process on water and energy budgets (Cherkauer and Lettenmaier 1999; Dankers et al. 2011; Ek et al. 2003; Niu and Yang 2006), leading to increased interests for using land surface models (LSMs) for runoff or streamflow modeling across domains with the frozen ground (Finney et al. 2012; Livneh et al. 2011; Slater et al. 2007; Y. Zhang et al. 2013). For instance, L. Zhang et al. (2013) and Xue et al. (2013) have recently applied LSMs for modeling the runoff regime of the Tibetan Plateau. However, key findings on understanding

***This chapter is based on the manuscript:** Zheng, D., R. van der Velde, Z. Su, J. Wen, X. Wang, M. J. Booij, A. Y. Hoekstra, S. Lv and Y. Zhang, 2015: Impacts of Noah model physics on vertical heat and water exchanges and regional runoff simulations. *In revision for Journal of Geophysical Research: Atmospheres.*

the prevailing hydro-meteorological processes in this high-altitude alpine region (e.g., Chen et al. 2011; K. Yang et al. 2009; Yang et al. 2005; Zheng et al. 2014) have not been thoroughly investigated.

The understanding of the hydro-meteorological processes on the Tibetan Plateau has greatly advanced due to the development of data sets collected as part of the various field campaigns and monitoring networks since 1998 (e.g., Koike 2004; 1999; Y. Ma et al. 2008; Su et al. 2011; Yang et al. 2013). Among the key findings are i) the diurnally varying roughness length for heat transfer (z_{oh}) as an imperative for reliable surface temperature and turbulent heat simulation (Chen et al. 2011; Zeng et al. 2012; Zheng et al. 2014), and ii) the necessity of vertical soil heterogeneity caused by organic matter and root systems for accurate soil water and heat flow calculations (Y. Chen et al. 2013; Yang et al. 2005). Above results are included into the Noah LSM as done in Chapters 5 and 6 of this thesis, and it's demonstrated that the augmentations improve the simulation of the vertical processes through comparisons with measurements performed at a hydro-meteorological station on the Tibetan Plateau.

This study further investigates the impact of the improved representation of the vertical processes within the Noah LSM on the runoff regime produced at catchment scale. For this investigation, the source region of the Yellow River (SRYR) in the northeastern part of the Tibetan Plateau and the study period 2001-2010 are selected. Apart from the default Noah LSM, four additional model runs are performed with augmentations to the i) soil and turbulent heat, ii) soil water and iii) frozen soil processes separately as well as combined. The high resolution (0.1 °) dataset by Chen et al. (2011) developed specifically for China is utilized as atmospheric forcing. Performance of the Noah simulations is assessed at point-scale using in-situ soil moisture and temperature measurements, and for the model domain using Yellow River discharge measurements. In addition, the spatial distributions of the runoff production mechanisms are quantified across the SRYR for each set of model physics.

This Chapter is outlined as follows: Section 7.2 introduces the Noah model physics and the augmentations. Section 7.3 describes the study area and in-situ measurements, and a description of the experimental design and datasets utilized for the model setup is provided as well. Section 7.4 and Section 7.5 present respectively the point scale and catchment scale assessment of the model performance in simulating soil states (i.e., moisture and temperature) and discharge. The sensitivity of the simulated runoff production for the impending

effect of frozen ground is also investigated in Section 7.5. Further Section 7.6 concludes with a summary of the findings in this study.

7.2 Noah model physics

Detailed descriptions of the default Noah model physics are given in Chapter 3 of this thesis, whereas the augmentations selected for this investigation are described below.

7.2.1 Noah-H

Overestimation of the turbulent heat fluxes and underestimation of skin and soil temperatures by Noah have been widely reported (Chen et al. 2011; Niu et al. 2011; Rosero et al. 2010; van der Velde et al. 2009; Zeng et al. 2012; Zheng et al. 2014). Four augmentations are proposed in Chapter 5 of this thesis to mitigate these deficiencies, which are hereafter referred to as ‘Noah-H’.

Firstly, the muting effect of vegetation, modeled as an exponential decay as function of the green vegetation fraction (*GVF*) and an empirical muting factor ($\beta_{veg}=2.0$), on the soil heat conductivity defining the heat transport from the first layer towards the second layer (κ_{h1}) is removed. Secondly, the exponential decay factor (β_{veg}) imposed on the surface heat conductivity defining the heat transport from the surface to the first soil layer (κ_{h0}) is calculated using the ratio of the leaf area index (*LAI*) over the *GVF* (i.e., $\beta_{veg}=0.5LAI/GVF$) for unstable atmospheric conditions. Thirdly, Zilitinkevich’s empirical coefficient ($C_{zil}=0.1$) for the turbulent heat transport is computed as a function of the roughness length for momentum transfer ($C_{zil}=10^{-0.4z_{0m}/0.07}$) given in Chen and Zhang (2009) and Zheng et al. (2014). Fourthly, the impact of organic matter is considered in the parameterization of the thermal heat capacity according to the method proposed by de Vries (1963), while the parameterization of thermal heat conductivity (Johansen 1975; Peters-Lidard et al. 1998) is modified to incorporate the organic matter effect on dry thermal heat conductivity via bulk density and saturated heat conductivity via the geometric mean of the heat conductivities of the materials present within the soil matrix including organic matter.

7.2.2 Noah-W

Recently, Y. Chen et al. (2013), Su et al. (2013) and Xue et al. (2013) have reported on the inability of the state-of-the-art LSMs to reproduce the soil moisture profiles measured across the Tibetan Plateau. This is attributed to the absence of vertical soil heterogeneity within the model structures that is present

within Tibetan ecosystems due to the abundance of plant roots and organic matter in the top soil. Four augmentations are proposed in Chapter 6 of this thesis to include the vertical soil heterogeneity into the Noah LSM, which is hereafter referred to as Noah-W.

Firstly, the effect of organic matter on the soil hydraulic properties is considered via the additivity hypothesis, which estimates the hydraulic parameters as a weighted combination of the mineral and organic fractions (Lawrence and Slater 2008; Zeiliger et al. 2000). Secondly, a function is implemented that decays the saturated hydraulic conductivity (K_s) exponentially with soil depth (Beven 1982), whereby the K_s at the reference depth (e.g., surface) is estimated by the Kozeny-Carman equation using the porosity and slope of the water retention curve (Ahuja et al. 1984; Saxton and Rawls 2006). Thirdly, the vertically uniform root distribution is replaced with an asymptotic function (Jackson et al. 1996; Y. Yang et al. 2009a) to better represent the abundance of roots in the topsoil of Tibetan ecosystems. Fourthly, the diffusivity form of Richards' equation is revised to allow soil water flow simulation across layers with different hydraulic properties (Hills et al. 1989).

7.2.3 Noah-F

Niu et al. (2011) recently pointed out that the Noah simulated impediment of frozen ground for infiltration is too strong, which causes too much surface runoff. Similarly, Slater et al. (2007) concluded that LSMs need to allow more infiltration under frozen ground conditions to adequately simulate the hydrographs of Arctic rivers. Noah approximates by default the fraction of impermeable ground under frozen conditions as a gamma distribution function applied to the total ice content present within the entire 2 m soil column (see eqs. (3.51)-(3.53)). It should, however, be noted that the datasets employed for the development of this approach originates from several Russian river basins and only extends to depths of 0.8 m (see Figure 4 in Koren et al. (1999)). Other LSMs (e.g., Balsamo et al. 2009; Cherkauer and Lettenmaier 1999) also utilize the soil ice and water contents of the first 0.5-0.6 m to estimate the fraction of impermeable area (f_{imp}). Moreover, Wang et al. (2009) have shown that the critical depth over which the active soil thawing affects surface runoff is around 60 cm for a Tibetan permafrost watershed. Therefore, it sounds more appropriate to use a shallower layer thickness within Noah for determining f_{imp} . Since the upper two layers represent only a 0.4 m soil depth, this study has chosen to take the upper three layers, extending up to 1.0 m, as the active thawing region.

In addition, the parameterization proposed by Niu and Yang (2006) is adopted for calculating the soil hydraulic conductivity (K) and soil water diffusivity (D). This formulation computes the transport coefficients as function of the total soil water content reduced by impermeable fraction of each layer, as follows,

$$K = (1 - f_{frz})K_s (\theta/\theta_s)^{2b+3} \quad (7.1)$$

$$D = (1 - f_{frz})D_s (\theta/\theta_s)^{b+2} \quad (7.2)$$

$$f_{frz} = \exp[-a(1 - \theta_{ice}/\theta_s)] - \exp(-a) \quad (7.3)$$

where K is the hydraulic conductivity (m s^{-1}), D is the soil water diffusivity ($\text{m}^2 \text{s}^{-1}$), θ is the total soil water content ($\text{m}^3 \text{m}^{-3}$), θ_{ice} is the soil ice content ($\text{m}^3 \text{m}^{-3}$), b is an empirical parameter (-) related to the pore-size distribution, f_{frz} is the impermeable fraction, a is an adjustable scale-dependent parameter taken as 4.0 as suggested by Niu et al. (2011), and the subscript 's' stands for the respective quantity under saturated soil conditions. Niu et al. (2011) recommend the above parameterization (eqs. (7.1)-(7.3)) over the default (eqs. (3.47)-(3.49)) to allow more transport of water when ice is present in the soil column.

7.3 Measurements and model implementation

A detailed description of the SRYR, the monthly streamflow measurement and the Maqu observational dataset utilized for this investigation is available in Chapter 2 of this thesis. The monthly streamflow data from the catchment outlet (i.e., Tangnag station) are available for the period of 2002-2009, and these will be utilized to investigate the performance of Noah LSM in simulating runoff at catchment scale. The Maqu dataset from both the micro-meteorological observing system and soil moisture and soil temperature (SMST) monitoring network are available from November 2009 to December 2010 except the precipitation data which only cover the period June-September 2010. Because of this, the daily precipitation measurements from the CMA (China Meteorological Administration) station located in the Maqu city, 10 km from the station, are utilized. Four SMST sites (CST01 and NST01/02/14, see Figure 2.1 of Chapter 2) of the regional scale network located in the vicinity of the micro-meteorological station (radius < 5 km) are used for validation of the Noah simulations at point scale. In the text below, the atmospheric forcing, the vegetation and soil parameterization adopted for the model setup as well as the design of numerical experiments are briefly introduced.

7.3.1 Atmospheric forcing

The atmospheric forcing data utilized for the Noah model runs are provided by the hydro-meteorological research group of the Institute of Tibetan Plateau Research, Chinese Academy of Sciences (hereafter ITPCAS), which were produced by merging a variety of data sources (Chen et al. 2011), e.g., CMA measurements, Global Land Data Assimilation Systems (GLDAS) forcing dataset (Rodell et al. 2004), Tropical Rainfall Measuring Mission (TRMM) satellite observed precipitation (Huffman et al. 2007) and GEWEX-SRB (Global Energy and Water Exchanges/Surface Radiation Budget) radiation (Yang et al. 2010). The ITPCAS dataset has a spatial resolution of 0.1° , a temporal resolution of 3h and includes seven forcing variables, i.e., 2 m air temperature (T_a), 10 m wind speed, air pressure, specific humidity, accumulated precipitation (P), downward shortwave (S^\downarrow) and longwave (L^\downarrow) radiations. Additional information on the ITPCAS forcing product and access can be obtained from <http://dam.itpcas.ac.cn/rs/?q=data>.

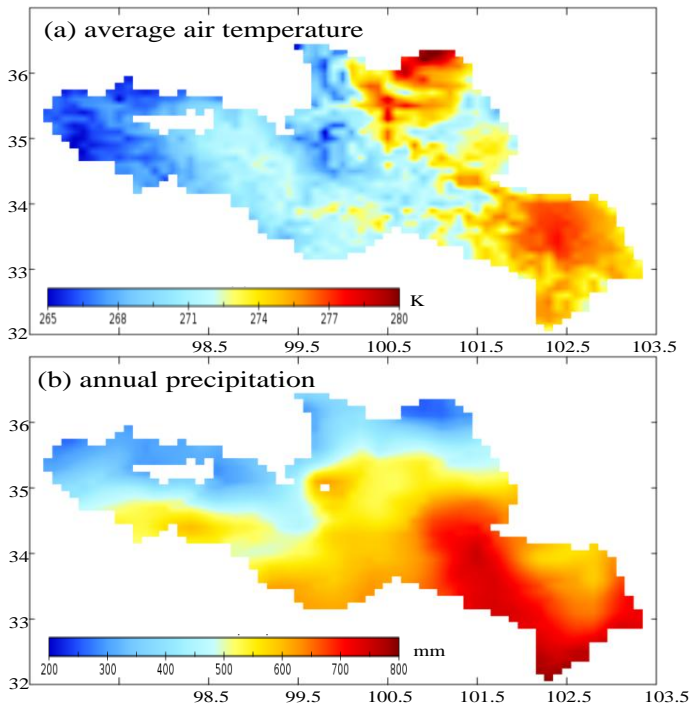


Figure 7.1: Mean annual 3-hourly air temperature (a) and mean annual precipitation (b) for the SRYS derived from 0.1° ITPCAS atmospheric forcing data covering the period of 2001-2010.

The time period under investigation is the episode 2001-2010, for which Figure 7.1 shows the spatially distributed mean annual 3-hourly T_a and mean annual P for the SRYR. The maps demonstrate that the spatial T_a distribution is in overall agreement with the topography (see Figure 2.1 of Chapter 2) with the lowest temperatures in the high altitude western part of the study area and the highest temperature in regions with the lowest elevation. A similar pattern is noted in the spatial precipitation field with, as expected, the largest rainfall amounts in the humid and low altitude southeast. The reliability of the ITPCAS forcing data for the Tibetan Plateau was previously confirmed (Chen et al. 2011; Guo and Wang 2013; Xue et al. 2013) and will be further investigated in Section 7.4 through comparisons to measurements collected at the Maqu station.

7.3.2 Vegetation and soil parameters

The vegetation and soil parameter data sets used in this study are mainly from the Weather Research and Forecasting (WRF) model input dataset (http://www2.mmm.ucar.edu/wrf/users/download/get_sources_wps_geog.html) and reprocessed using the WRF preprocessing system. Specifically, the 20-category land-use data map derived from the Moderate Resolution Imaging Spectroradiometer (MODIS) satellite observations and the hybrid STATSGO/FAO soil texture map are selected for assigning the vegetation and soil type to each grid cell. The green vegetation fraction (GVF) and leaf area index (LAI) are both obtained from the monthly MODIS climatology. Soil hydraulic and vegetation parameters are specified for each vegetation and soil type by means of Noah's default look-up tables (see Chapter 3) with the exception of momentum roughness lengths (z_{0m}) for grassland and bare ground, which are set at 0.035 and 0.011 m respectively following Zheng et al. (2014).

Further, the organic matter content for the updated soil thermal and hydraulic parameterizations (Sections 7.2.1 and 7.2.2) are taken from the China Soil Database developed by the land-atmosphere interaction research group at Beijing Normal University (<http://globalchange.bnu.edu.cn/research/soil2>; Shangquan et al. 2013). The organic matter contents available for eight soil layers are linearly interpolated to match with the four layers of the Noah model structure according to Xia et al. (2014). Moreover, the Sapric peat parameterization reported by Letts et al. (2000) is adopted to represent the hydraulic properties for pure organic matter.

7.3.3 Experimental design

Five experiments are designed to assess the impact of the augmentations to the default Noah LSM described in Section 7.2. The Noah LSM is firstly run with its default model physics described in Chapter 3 of this thesis (hereafter Noah). Secondly, three Noah runs are performed by implementing each set of augmentations described in Section 7.2 respectively. As such, the Noah model is run with augmentations to the model physics of the i) turbulent and soil heat flux processes (Section 7.2.1, hereafter Noah-H), ii) soil water flow processes (Section 7.2.2, hereafter Noah-W), and iii) runoff production under frozen ground conditions (Section 7.2.3, hereafter Noah-F). Lastly, all three sets of augmentations are combined to form the fifth experiment (hereafter Noah-A).

This study presently employs Noah LSM version 3.4.1 available as part of the HRLDAS (High Resolution Land Data Assimilation System). The codes are modified to make use of the ITPCAS forcing dataset (Section 7.3.1) and organic matter content derived from the China Soil Database (Section 7.3.2), as well as to accommodate the augmentations described in Section 7.2. All the experiments are initialized with the same arbitrary hydrologic and thermal states taken constant across the model domain. For instance, the surface and soil temperatures are set to 278.5, 284, 284.5, 282.5 and 280.5 K respectively from the surface to the bottom layer, and the soil moisture is initialized as 70 % of the porosity. The annual 3-hourly mean T_a from the ITPCAS forcing (Figure 7.1a) is used as the fixed bottom (8 m) boundary for soil temperature computation. The model time step is 30 min, and the 3h ITPCAS forcing is interpolated to the model time step automatically using the HRLDAS functionality. A single-year recurrent spin-up during the period between 1st of July 2001 and 30th of June 2002 is carried out for each experiment to achieve the equilibrium model states. The choice of July for the start of the spin-up is based on the suggestions by Shrestha and Houser (2010) and Lim et al. (2012) that the equilibrium states are more quickly achieved with the spin-up run started in the summer monsoon months. A single continuous 8.5 yr simulation during the period between 1st of July 2002 and 31st of December 2010 is conducted for each experiment.

Point (or grid) scale validation is performed through comparison of the Noah simulations with the measurements of soil moisture and temperature profiles as well as latent heat flux (LE) from Maqu station available for the period November 2009 to December 2010. The soil moisture and soil temperature measurements collected at the four SMST sites (i.e., CST01 and NST01/02/14) are averaged for each soil depth (e.g., 0.05, 0.10, 0.20, 0.40 and 0.80 m), and subsequently interpolated to the mid-points of the upper three model layers (i.e.,

0.05, 0.25 and 0.70 m) for the analysis. Streamflow data from the catchment outlet (i.e., Tangnag station) integrating spatial information across the entire SRYR are used for the regional scale assessment for the period July 2002 to December 2009. Monthly streamflow (m^3) observations are converted to the areally averaged runoff depth (mm) by dividing by the area of the SRYR (km^2). Surface runoff (R_s) and base flow (or drainage, R_b) simulated by each Noah model run are accumulated over the individual model grid except for the lakes and glaciers in the SRYR, and accumulated for each month to produce the monthly areally averaged total runoff by dividing by the number of accumulated model grids. River routing is not applied to the Noah output, also since averaging at the monthly scale will largely eliminate the differences between the computed runoff and the time-delay implicitly incorporated in instantaneous observed runoff (Cai et al. 2014; Pitman et al. 1999).

7.4 Point-scale assessment

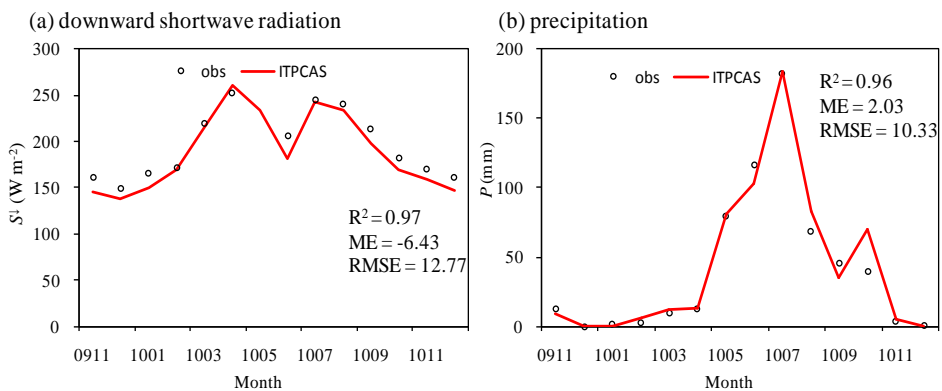


Figure 7.2: Comparisons of in-situ measured and ITPCAS atmospheric forcing data for the period November 2009 - December 2010: (a) monthly averaged downward shortwave radiation and (b) monthly accumulated precipitation.

Figure 7.2 shows the monthly average of the downward shortwave radiation (S^{\downarrow}) and monthly precipitation (P) sums computed from the Maqu measurements and ITPCAS forcing (Section 7.3) for the period between November 2009 and December 2010. The error statistics computed between the measurements and the ITPCAS forcing are shown in the Figure as well, i.e., the coefficient of determination (R^2), mean error (ME) and root mean squared error (RMSE). The agreement noted between the measurements and the ITPCAS forcing supported by the error statistics, e.g., R^2 of 0.97 and 0.96, RMSE of

12.77 W m⁻² and 10.33 mm month⁻¹ for S^l and P respectively, confirms the reliability and suitability of the ITPCAS forcing for this study.

Figure 7.3 shows the monthly average of the measured and simulated latent heat flux (LE), soil temperature (T_s) and liquid soil moisture (θ_{liq}) profiles produced by the five Noah experiments (Section 7.3.3), and Table 7.1 lists the respective RMSEs. With its default model physics, Noah overestimates the LE (Figure 7.3a) and underestimates the T_s profile measurements (Figures 7.3b and 7.3c) during the summer monsoon season between June and October, and the θ_{liq} profile measurements are consistently underestimated across the whole year (Figures 7.3d and 7.3e). After implementing the augmentations made to the model physics associated with the turbulent and soil heat transport (Section 7.2.1), the overestimation of LE and underestimation of T_s are greatly resolved as can be deduced from the Noah-H results. This reduces in comparison to the default Noah model the RMSE computed between the measured and simulated LE and T_s for depths of 5 cm and 25 cm by about 24, 6, and 36 %, respectively.

Also, an improvement is noted in θ_{liq} simulations as a result of selected augmentations. Notably, the θ_{liq} underestimation by the default Noah model is significantly ameliorated through implementation of the modified soil hydraulic parameterization with consideration of the organic matter effect and asymptotic vertical root distribution (Section 7.2.2) as applied in the Noah-W run. This leads to a reduction in the RMSE computed between the simulated and measured θ_{liq} by about 39 and 54 % for the upper two soil layers. On the other hand, it results in a somewhat degraded model performance with respect to the LE and T_s simulation. Noah-F produces a slight improvement in the surface soil moisture simulation through allowing a larger liquid water movement into the frozen front during the cold season at the cost of degraded soil moisture simulation for the lower layer in comparison to the default Noah model. Noticeable improvements are found in simulation of LE , T_s as well as θ_{liq} by including all augmentations described in Section 7.2 in the Noah model physics (i.e., Noah-A model run). In this case the RMSEs computed between the measurements and simulations reduced by about 15, 11, 44, 60, 55 % for LE , T_{s5} , T_{s25} , θ_{liq5} , and θ_{liq25} respectively in comparison to the default Noah model run. This demonstrates the necessity to include complete and robust descriptions of both surface energy and water budget processes in model physics for reliable simulations of heat and mass exchanges at the SRYR land-atmosphere interface.

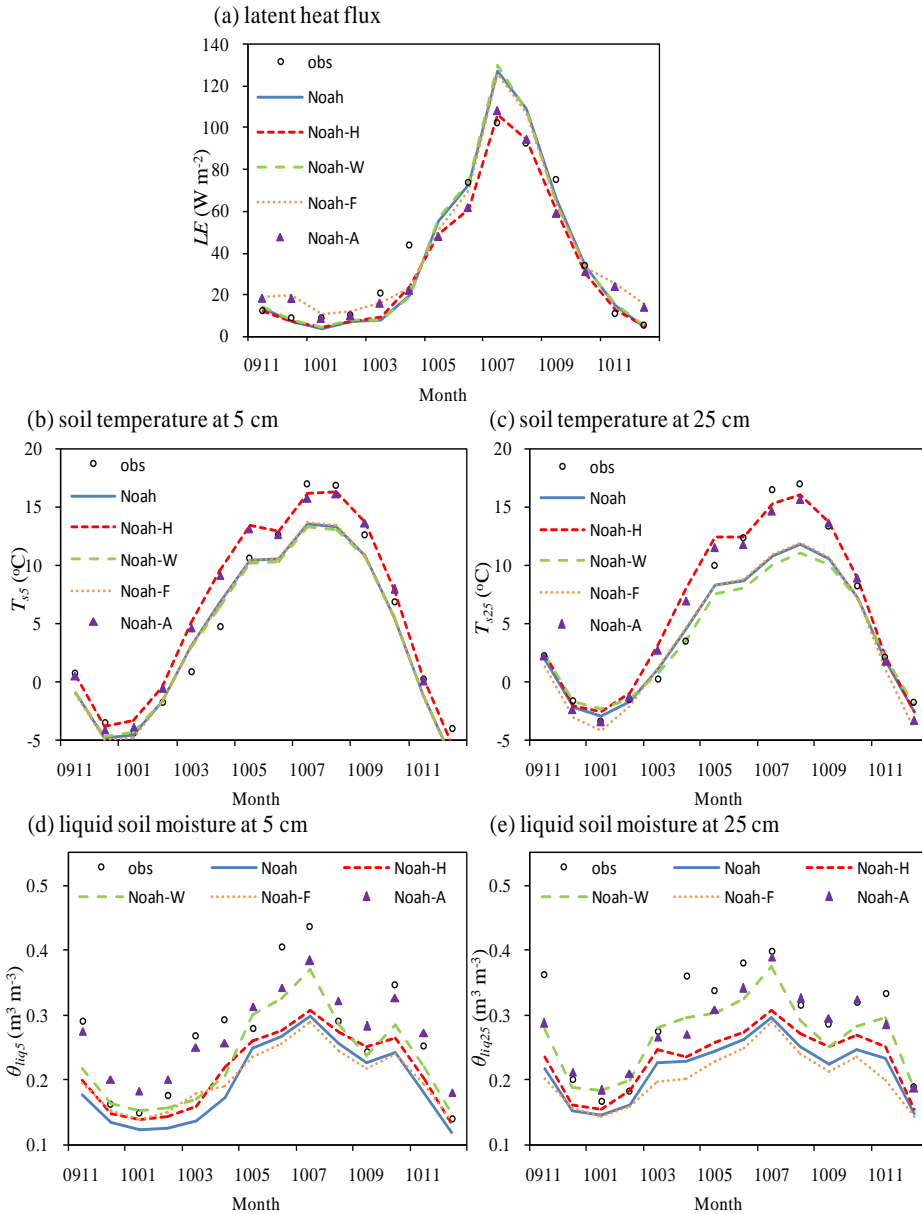


Figure 7.3: Comparisons of measured and simulated monthly averaged (a) latent heat flux, soil temperature at depths of (b) 5 cm and (c) 25 cm, as well as liquid soil moisture at depths of (d) 5 cm and (e) 25 cm produced using five numerical experiments for the period November 2009 - December 2010.

Table 7.1: Root mean square error (RMSE) computed between the measured and simulated latent heat flux (LE), soil temperature (T_s) and liquid soil moisture (θ_{liq}) at depths of 5 cm and 25 cm produced by five numerical experiments for the period from November 2009 to December 2010

RMSE	LE (W m^{-2})	T_{s5} (K)	T_{s25} (K)	θ_{liq5} ($\text{m}^3 \text{m}^{-3}$)	θ_{liq25} ($\text{m}^3 \text{m}^{-3}$)
Noah	11.66	2.05	2.56	0.090	0.084
Noah-H	8.82	1.93	1.63	0.074	0.072
Noah-W	12.52	2.10	2.91	0.055	0.039
Noah-F	11.76	2.06	2.69	0.083	0.099
Noah-A	9.97	1.83	1.44	0.036	0.038

7.5 Catchment-scale assessment

7.5.1 Areal average

Figure 7.4 shows the monthly accumulated areally averaged measured and simulated total runoff depth (R) produced by the five Noah experiments (Section 7.3.3) for the period July 2002 - December 2009, whereby the measurements, Noah, Noah-H and Noah-W are presented in the upper panel, and the measurements, Noah, Noah-F and Noah-A in the lower panel. In addition, the monthly R averaged for the 7.5 year period is shown for both measurements and simulations. Table 7.2 provides the respective error statistics, i.e., R^2 , ME, RMSE and Nash-Sutcliffe efficiency (NSE). Noah with its default model physics is able to capture the observed monthly R dynamics reasonably well, which is also supported by R^2 and NSE values larger than 0.80. Underestimations of the observed R are, however, noted during the summer season from July till October and the cold season from January till March.

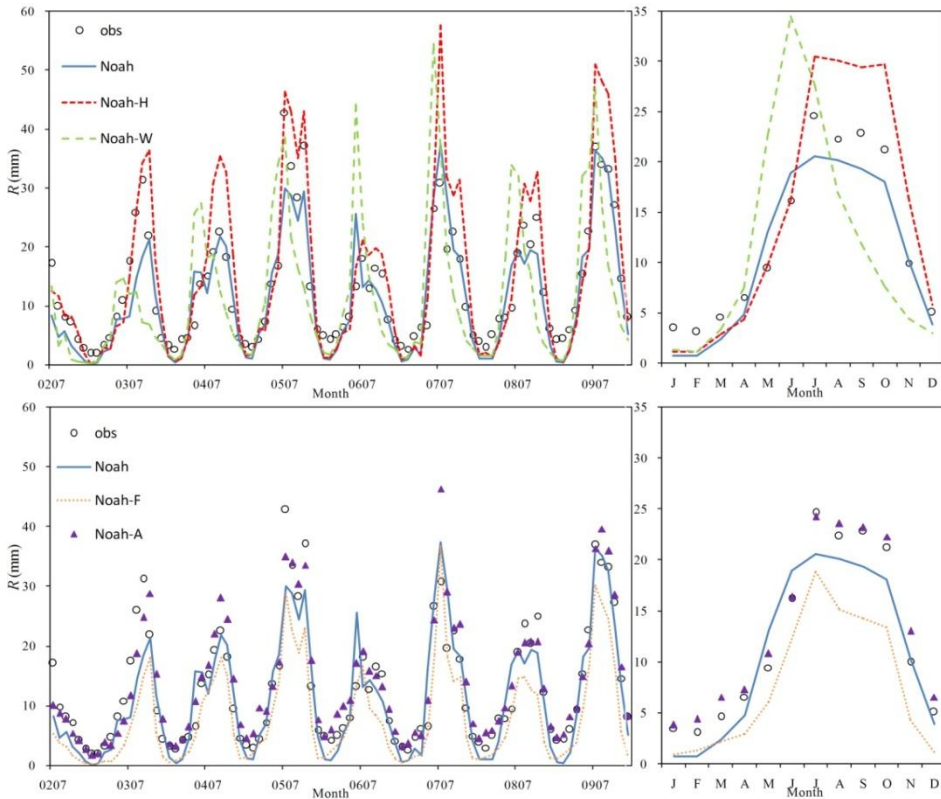


Figure 7.4: Comparisons of measured and simulated (left panel) monthly accumulated and (right) multi-year monthly averaged total runoff (R) produced using five numerical experiments for the period July 2002 - December 2009.

Table 7.2: Coefficient of determination (R^2), mean error (ME), root mean square error (RMSE) and Nash-Sutcliffe efficiency (NSE) computed between the measured and simulated total runoff produced by all the numerical experiments for the period from July 2002 to December 2009

Experiments	R^2	ME (mm)	RMSE (mm)	NSE
Noah	0.825	-1.43	4.44	0.80
Noah-H	0.900	2.59	6.33	0.59
Noah-W	0.381	-0.96	9.88	-0.01
Noah-F	0.868	-4.83	6.11	0.61
Noah-A	0.882	1.08	3.62	0.86
EXPS1	0.894	0.92	3.55	0.87
EXPS2	0.894	0.91	3.54	0.87

Although Noah-H greatly improves the simulation of the turbulent and soil heat transport (Section 7.4), it largely overestimates the R observed in the period from July to November (> 6 mm on the average) and yields the poor error statistics in terms of ME, RMSE and NSE. Noah-H does, however, produce R that agrees well with the measurements made in the transition season (i.e., May and June) as well as better estimate of R^2 . Likewise the improved soil moisture profile simulation achieved with Noah-W (Section 7.4) does not automatically implicate that its R simulations agree well with the measurements. In fact, the plots as well as the error statistics suggest that Noah-W represents the worst performance in simulating R . In particular, the simulated R peaks early significantly overestimating the measurements between May and July (> 10 mm on the average), while significant underestimations of measured R are found for September and October. Also, the performance of Noah-F in simulating the hydrograph is poorer than the default model with year-round underestimations of the monthly measured R .

Only when all augmentations are implemented, viz. Noah-A, an improved performance in simulating R is achieved with respect to the default model. The underestimations of the monthly R across the summer and cold season is largely resolved by including the augmentations for heat, soil water as well as frozen ground processes. Hence, the error statistics improve by about 7, 24, 19 and 8 % for R^2 , ME, RMSE and NSE with respect to the Noah experiment. As such, these results eloquently confirm the findings of Section 7.4 at catchment-scale via runoff on the need for including complete descriptions of surface energy and water budget processes in model physics.

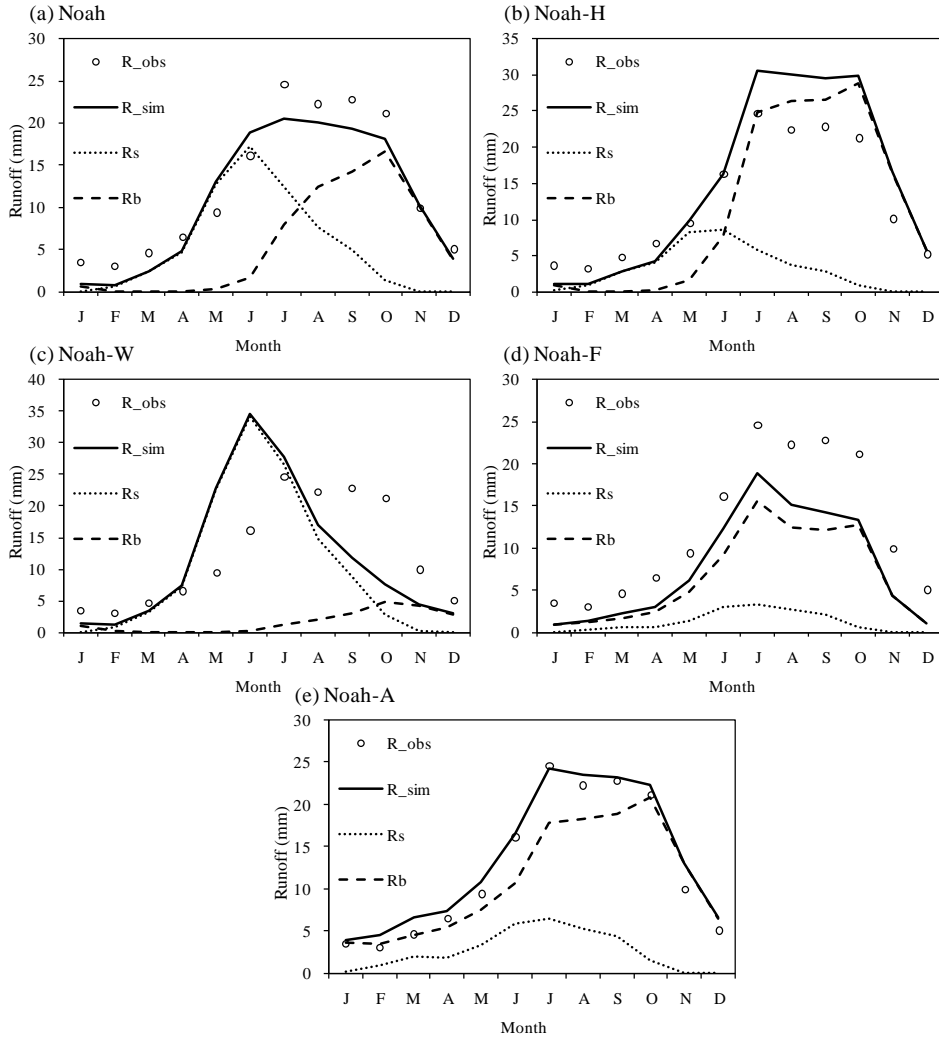


Figure 7.5: Monthly averaged measured runoff (R_{obs}), simulated total runoff (R_{sim}), surface runoff (R_s) and baseflow (R_b) produced using (a) Noah, (b) Noah-H, (c) Noah-W, (d) Noah-F and (e) Noah-A numerical experiments for the period July 2002 - December 2009.

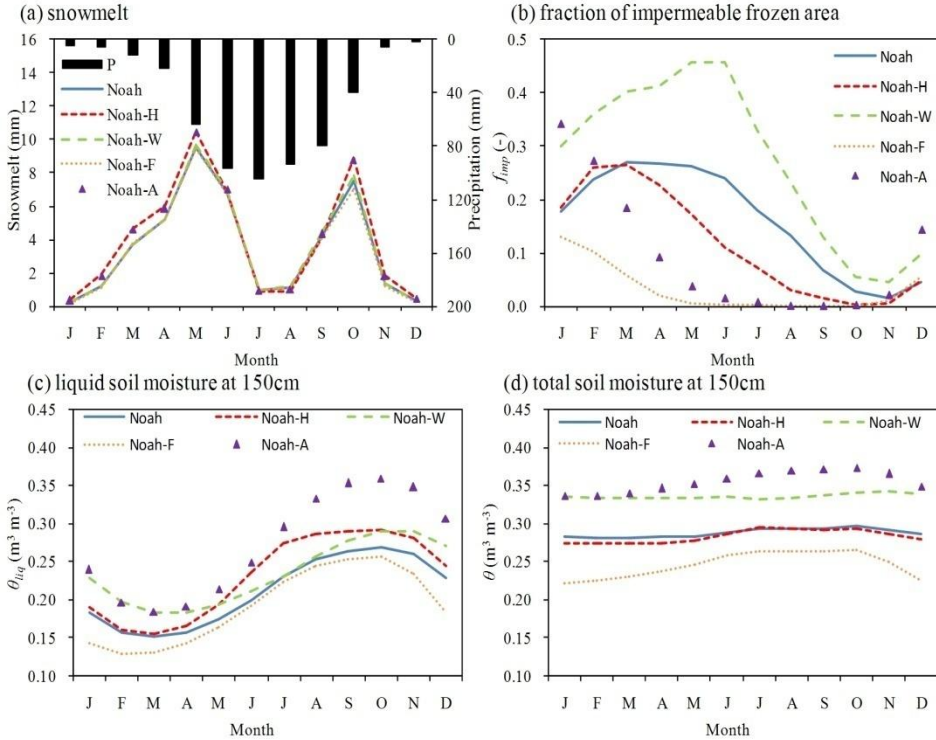


Figure 7.6: Comparisons of the simulated monthly averaged (a) snowmelt, (b) fraction of impermeable frozen area, (c) liquid and (d) total soil moisture at depth of 150 cm produced by five numerical experiments for the period July 2002 - December 2009.

In support of further analysis, Figure 7.5 presents the monthly averaged total runoff (R), surface runoff (R_s) and base flow (R_b) for each experiment. Additionally, Figure 7.6 shows the precipitation (P), snowmelt, fraction of impermeable frozen area (f_{imp}), liquid (θ_{liq150}) and total (θ_{150}) soil moisture at the bottom soil layer (e.g., 150 cm). First of all, it can be noted that all experiments produce comparable snowmelt as seen in Figure 7.6a. Noah with its default model physics produces f_{imp} values varying from 0.18 to 0.27 in the first half year (Figure 7.6b). Precipitation and/or snowmelt simulated for these impermeable frozen areas result in surface runoff. As the ice content, viz. θ_{150} (Figure 7.6d) - θ_{liq150} (Figure 7.6c), is substantial in the first half of the year the drainage or R_b remains low and R_s component dominates the total runoff simulated by Noah (Figure 7.5a). The impermeable frozen area (f_{imp}) disappears gradually during the warm season (June-October) as the ice in the soil profile

thaws. More water can, therefore, infiltrate into the soil column increasing θ_{liq150} and the drainage from the soil bottom, which leads to the simulated total runoff being governed by R_b with peaks in October. At the onset of the cold season, e.g., October-December, the R_b and R decline due to the absence of precipitation in combination with an increase in the ice content in the bottom soil layer. Notably, the larger θ_{150} in comparison to θ_{liq150} indicates that frozen conditions occur at least in portions of the study domain (i.e., permafrost vs. seasonally frozen ground).

Since Noah-H produces generally warmer temperature profiles (Section 7.4), the onset of the thawing of ice within the soil profile is simulated earlier in the year. Therefore, the seasonal f_{imp} decrease and θ_{liq150} increase is already noted starting from March causing comparable a shift in the transition from R_s towards R_b dominated total runoff (Figure 7.5b). This leads to a good match with the measurements between May and June, but to considerable runoff overestimations for the monsoon months, e.g., July, August and September. A wetter soil moisture profile and larger ice content across the soil column is generated by Noah-W, which results in a large f_{imp} (Figure 7.6b) and, thereby, a strongly R_s dominated total runoff (Figure 7.5c). This explains the early R peaks and wrong shape of the hydrograph. Noah-F, in contrast, produces the smallest f_{imp} leading to more infiltration and a strongly R_b dominated total runoff (Figure 7.5d) allowing for a large liquid water movement under frozen ground conditions as is consistent with the findings of Sato et al. (2008).

Figure 7.4 and the error statistics in Table 7.2 demonstrated already that Noah captures the measured hydrograph best when all augmentations are implemented (Noah-A). With the set of model physics included in Noah-A, the ice content is simulated in such manner that f_{imp} can be large in winter (> 0.3) and decreases sharply at the end of the cold season to approach zero in the warm season (June-October). As such, Noah-A enables the infiltration into and release from water into the soil column during summers and the retention of soil water during winters, whereby R_b is the main component year-round and plays thus an important role in the simulation of the hydrograph. This simulated runoff regime is in line with the recommendations done by Slater et al. (2007) for the simulation of the hydrographs of Arctic rivers with LSMs.

7.5.2 Spatial variation

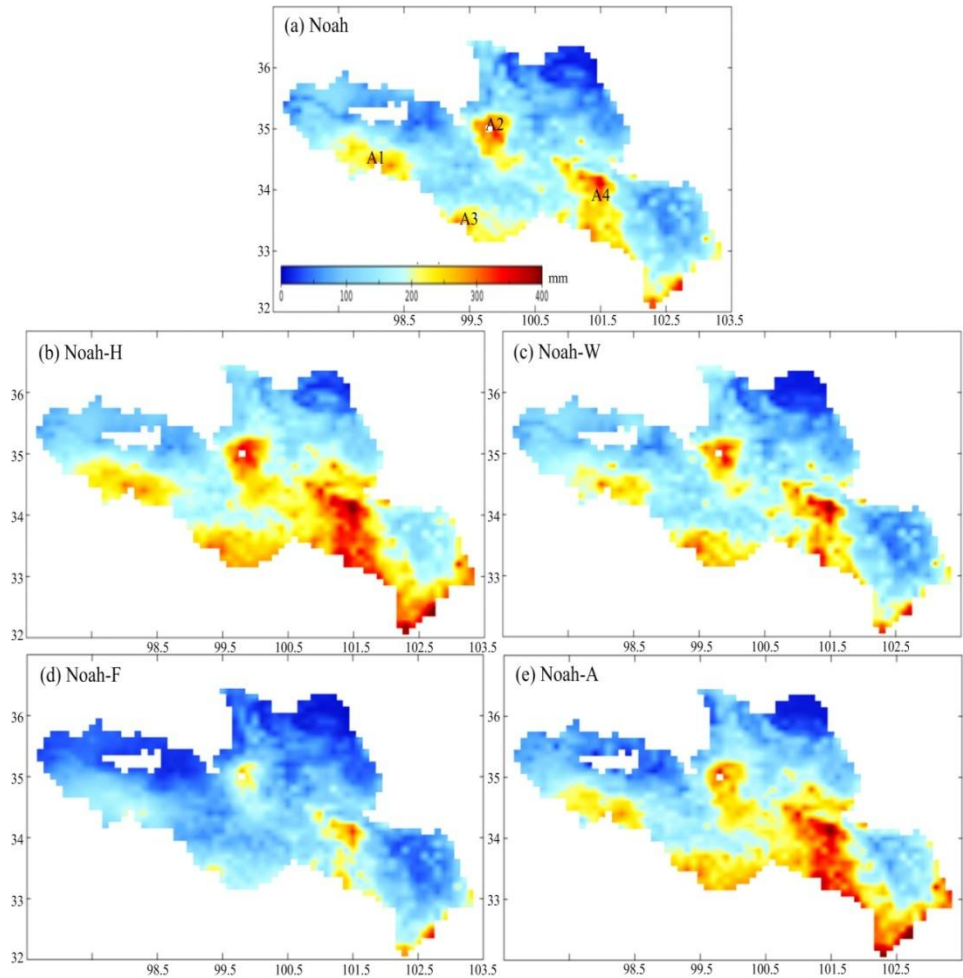


Figure 7.7: Maps of annual mean total runoff across the SRYP produced by (a) Noah, (b) Noah-H, (c) Noah-W, (d) Noah-F and (e) Noah-A numerical experiments for the period July 2002 - December 2010.

Figure 7.7 shows the spatial distribution of annual mean R over the SRYP produced by the five experiments during the period between July 2002 and December 2010. Four distinct regions of runoff production can be deduced from the R distribution produced by the Noah with default model physics (Figure 7.7a), e.g., i) region A1 located at the western high altitude area (see Figure 2.1 of Chapter 2), ii) region A2 located at the central Anyemqen Mountains, iii) region A3 located at the southwestern high altitude area near Jimai discharge

station, and iv) region A4 located near Maqu discharge station in the region with high precipitation (see Figure 7.1b). The other experiments produce a similar spatial R distribution as the default Noah model, which in general follows the spatial P distribution. Hence, the high precipitation regions form the source regions of runoff production, whereby the largest production simulated by each of the five experiments takes place between Jimai and Maqu discharge stations as previously reported in Zheng et al. (2007).

For further analysis Figure 7.8 shows the annual mean R_s as fraction of R produced for the five experiments. In addition, Figure 7.9 presents the annual averaged f_{imp} for the default Noah and Noah-A model. From the comparison of Figure 7.7 and 7.8 can be deduced that the runoff produced by the Noah with default model physics in regions A1 and A2 mainly consist of the R_s component, while R_b dominates the production in regions A3 and A4 due to a relatively small f_{imp} (Figures 7.8a and 7.9a). The overall warmer temperature simulated by Noah-H leads to a smaller f_{imp} (Figure 7.6b) and more water infiltrates into the soil column, which results in, a smaller contribution of R_s across the SRYR (Figure 7.8b). Since Noah-H simulates less evapotranspiration (ET , e.g., Figure 7.3a) and less soil ice, more water is available (Figure 7.6c) for the drainage from the bottom of the soil column (or R_b) explaining for the larger runoff volume seen in the extended source regions A1-A4 (Figure 7.7b). The spatial distribution of Noah-W R production is similar to the default Noah (Figures 7.7a and 7.7c), but is characterized by a larger f_{imp} causing R_s to dominate the R production (Figures 7.8c). Conversely, Noah-F simulates less f_{imp} and, therefore, the R_s contribution is small (Figure 7.8d), but generates more surface liquid soil moisture and ET during the cold dry season (Figures 7.3a and 7.3d) causing less water (Figure 7.6d) to be available for the runoff production via baseflow (Figure 7.7d).

With implementation of all augmentations, Noah-A produces a similar spatial R distribution as Noah-H (Figures 7.7b and 7.7e), but smaller in magnitude. In general, the R_s as fraction of the total runoff is less than 0.4 (Figure 7.8e) and, therefore, the simulated hydrograph is governed by the R_b as concluded above. Figure 7.9 illustrates that the difference in f_{imp} simulated by the Noah-A and Noah models is responsible for the respective magnitudes of R_s and R_b as contributions to the total runoff production and overall performance. These results underline the need for a complete description of both cold and warm season hydro-meteorological processes for accurately simulating the impeding effect of frozen ground and the runoff production.

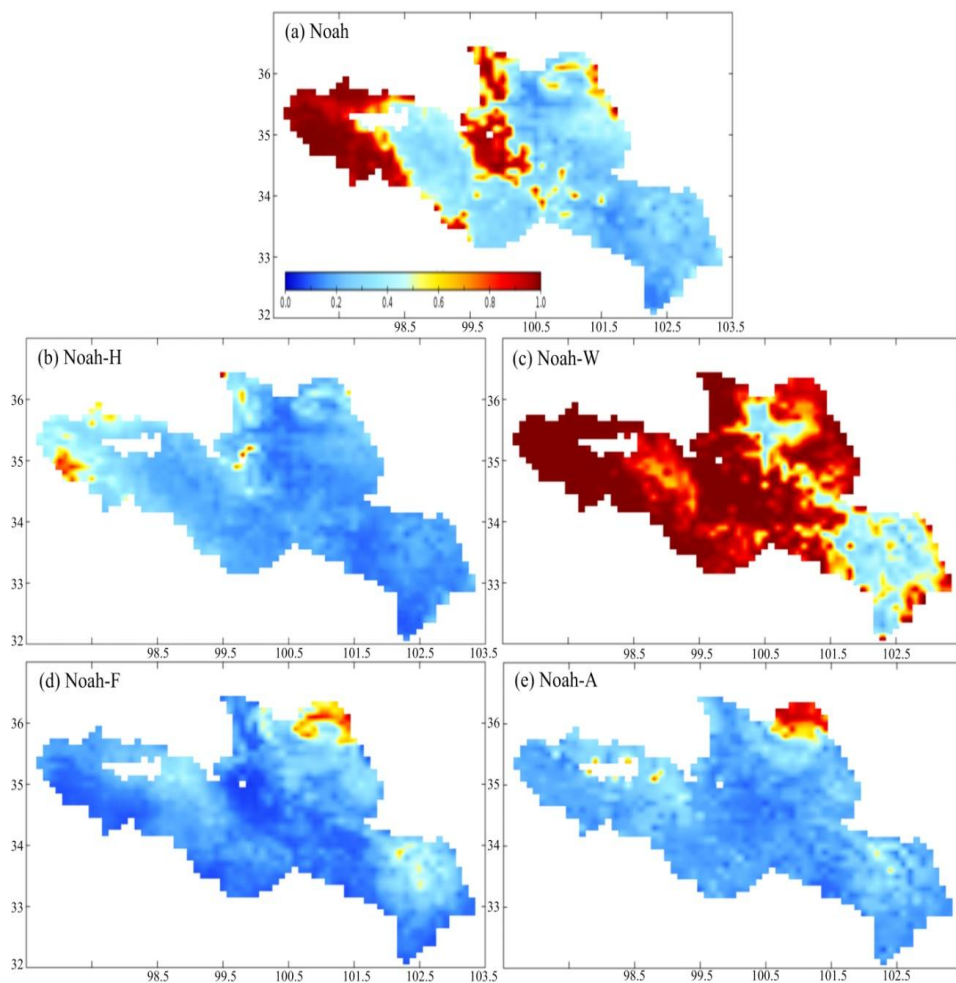


Figure 7.8: Maps of annual mean surface runoff as fraction of the total runoff for the SRYP produced by (a) Noah, (b) Noah-H, (c) Noah-W, (d) Noah-F and (e) Noah-A numerical experiments for the period July 2002 - December 2010.

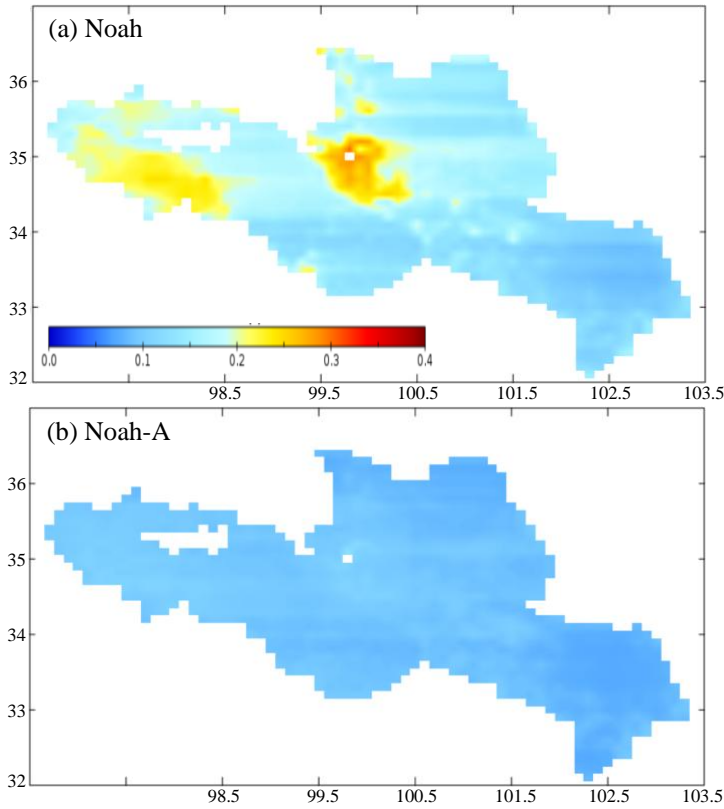


Figure 7.9: Maps of annual averaged fraction of impermeable frozen area for the SRYP produced using (a) Noah and (b) Noah-A numerical experiments for the period July 2002 - December 2010.

7.5.3 Sensitivity analysis

The above results demonstrate that the fractional impermeable frozen area, f_{imp} , plays a crucial role in simulating the runoff production for the SRYP. Noah-A, in which f_{imp} is calculated using the ice content in the top 1 m, performs better than Noah that uses by default the ice content present within the entire 2 m column. Two additional experiments are carried out to investigate the sensitivity of the modeled runoff for the f_{imp} computed with ice contents from different soil depths. One experiment uses the ice content of the two top layers (0.4 m) to calculate f_{imp} (hereafter EXPS1) and the other one utilizes only the upper layer (0.1 m, hereafter EXPS2), while all other settings remains as in Noah-A.

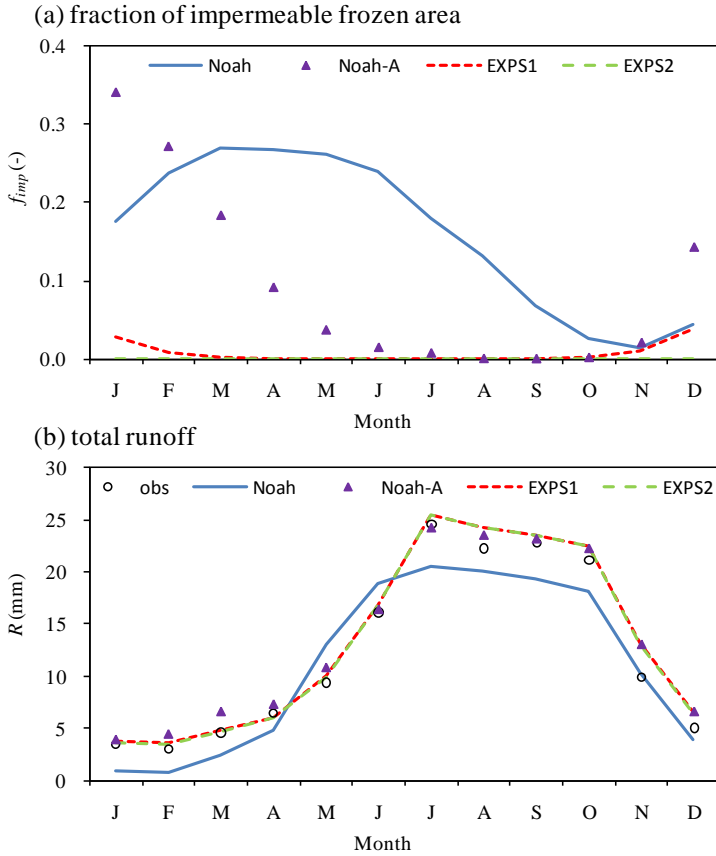


Figure 7.10: Comparisons of the measured and simulated monthly averaged (a) fraction of impermeable frozen area and (b) total runoff by the model runs performed for the sensitivity experiment in Section 7.5.3 for the period July 2002 - December 2009.

Figure 7.10 shows the monthly and areally averaged f_{imp} and total runoff (R) resulting from EXPS1 and EXPS2, whereby the measurements as well as the Noah and Noah-A simulations are added as well for comparison purposes. Further, the error statistics computed between the measured and simulated R are included in Table 7.2. Figure 7.10a illustrates that the usage of a shallower soil depth for the ice content produces less f_{imp} and approaches zero for EXPS2. This implicates that Noah does not invoke the impeding effect of frozen ground on infiltration, which marginally affects the model performance as indicated by Figure 7.10b as well as the error statistics listed in Table 7.2. The explanation for this is that in general the potential R_s source in the SRYR during the cold

season is limited by the water availability (e.g., precipitation and snowmelt). Also, Pitman et al. (1999) recommended that LSMs should not include the effect of frozen ground in the runoff formulation for coarse grid simulations as frozen soils remains permeable due to the development of a soil structure with cracks and macro-pores that facilitates preferential pathways.

7.6 Summary and conclusions

This study investigates impact of various Noah model physics' options, validated at the point scale, for its ability to reproduce the runoff at catchment scale through comparison of the monthly discharge measured in source region of the Yellow River (SRYR) of the period from 2001 to 2010. For application of the Noah model to the SRYR at catchment scale three sets of augmentations are selected that enhance the descriptions of i) turbulent and soil heat transport, ii) soil water flow and iii) frozen ground processes. Accordingly, five numerical experiments are designed; namely, a control run with the default model physics (hereafter Noah), three runs each with one of the selected augmentations (hereafter Noah-H, Noah-W and Noah-F respectively) and a run whereby all augmentations are implemented (hereafter Noah-A). All Noah model runs adopt their main soil and vegetation parameterizations from the Weather Research and Forecasting (WRF) model geographic input dataset, are driven by the ITPCAS atmospheric forcing data set and are initialized using a single-year recurrent spin-up to achieve the equilibrium model states. In addition, the China Soil Database provides the organic matter content for the updated soil thermal and hydraulic parameterizations.

A point-scale assessment is performed through comparisons of the five simulations with in-situ latent heat flux (LE), soil moisture (θ) and soil temperature (T_s) profile measurements for the period from November 2009 to December 2010. The results illustrate that the LE overestimation and T_s underestimation across the profile using the default Noah model are greatly resolved with the augmentations applied for the Noah-H experimental run. The default θ underestimation is significantly improved through including the parameterization of the vertical soil heterogeneity as in Noah-W. However, improvement in LE , T_s as well as θ_{liq} simulation is only achieved by including all selected augmentations (e.g., Noah-A model run), which leads to reductions in the RMSE of about 15, 11, 44, 60, 55 % for LE , T_{s5} , T_{s25} , θ_{liq5} , and θ_{liq25} respectively.

Monthly streamflow data measured at the outlet of the SRYR from July 2002 to December 2009 are utilized to quantify the model's ability to reproduce

the runoff regime at catchment scale. The default Noah model is able to adequately capture the observed total runoff (R) dynamics, but underestimates the magnitude of the monthly streamflow. Although the largest coefficient of determination (R^2) is obtained with Noah-H, large overestimations are generally found for the summer months due to the excessive release of water from the bottom of the soil column (e.g., baseflow, R_b). In contrast, the Noah-W runoff yields the lowest R^2 that can be associated with the wrongly simulated discharge peak caused by the surface runoff (R_s) dominated R due to amplified impeding effect of frozen ground. This effect is strongly reduced using augmentations applied with Noah-F allowing more water to infiltrate and a larger R_b component than Noah-W, which is yet insufficient to adequately reproduce the measurements.

The best agreement between the simulated and measured monthly streamflow data yields the Noah run whereby all selected augmentations are invoked (Noah-A) with improved error statistics of about 24 % and 19 % in comparison to the default performance for ME and RMSE respectively. The combination of the augmentations selected for Noah-H, Noah-W, and Noah-F properly simulate the liquid moisture content across the soil profile and the permeability of frozen ground. In addition, a warmer soil profile and sufficient infiltration into the soil profile is simulated leading to a R_b dominated runoff regime whereby the R_s contribution is still important to achieve a match with the measurements.

Although each of the five experiments produce similar spatial R patterns that generally follow the applied precipitation fields, significant differences are found in the magnitude as well as the partitioning of R into R_s and R_b . For instance, Noah-W provides the largest fractional impermeable frozen ground (f_{imp}) and thus the R is dominated by the R_s component. On the other hand, Noah-A produces a smaller f_{imp} and allows more water to infiltrate during spring, the rainy summer and snowmelt season, which enables a year-round release of water from the soil bottom resulting in a superior estimate of the measured hydrograph. Furthermore, a sensitivity experiment illustrates that within the Noah-A structure and for the selected study area the impeding effect of frozen ground has a marginal impact on model performance. Similar findings were previously reported by Pitman et al. (1999), in which they concluded that across large domains frozen soils remain permeable.

This study demonstrates that thorough understanding of the predominantly vertical heat and water exchange processes at the land-atmosphere interface is needed to correctly simulate the runoff produced in the seasonally frozen and

high altitude SRYR at catchment scale. In addition, the simulation with the augmented Noah model eloquently illustrates for the study period that the runoff production regime of SRYR was year-round dominated by the R_b component, while the default Noah underestimates its importance during the winter and spring seasons. Improved simulation of vertical heat and water exchanges is, therefore, of paramount importance to project the impact of climate variability on regional hydrology and the water resources availability in the Asian water towers.

Chapter 8 Conclusions and recommendations

Understanding the water and heat exchanges across the Tibetan ecosystem is of great importance for management of the Asian water towers that originate from the Tibetan Plateau and projection of water and energy dynamics within various climate scenarios. This thesis contributes to a better quantification of the water and heat exchanges at the land-atmosphere interface for a Tibetan alpine meadow ecosystem. Four research questions have been formulated to achieve the objective (see Chapter 1), and this concluding chapter starts with reflecting on the objective of this thesis and answering the research questions (Section 8.1). Subsequently, directions for further research are recommended (Section 8.2).

8.1 Conclusions

The source region of the Yellow River (SRYR, see Chapter 2) in the northeastern part of the Tibetan Plateau has been selected as the case study for this thesis, because of its great importance to the Yellow River's water resources that supports about 14.9 % of China's population and 17 % of its agricultural area. A comprehensive observational dataset including in-situ micro-meteorological and profile soil moisture/temperature measurements in an alpine meadow ecosystem (i.e., Maqu station), laboratory soil property measurements of samples collected across the SRYR, as well as discharge measurements from the SRYR outlet (i.e., Tangnag station) has been collected.

To understand the processes governing the water and heat exchanges of the alpine meadow ecosystem and predict the measurements, the Noah land surface model (LSM, see Chapter 3) has been utilized as the baseline model for this thesis, because it is widely used by the climate and land surface modeling communities (e.g. the Weather Research and Forecasting (WRF) model community) to quantify the exchange of water and heat at the land-atmosphere interface. Besides, the reliability of the Noah LSM for the Tibetan Plateau was previously confirmed (e.g., Chen et al. 2010; van der Velde et al. 2009; Zeng et al. 2012).

The aforementioned four research questions have been addressed in Chapters 4, 5, 6 and 7 respectively via enhancing Noah's model physics in representing i) turbulent and soil heat transport, ii) soil water flow and iii) frozen ground processes to arrive at a reliable prediction of the measured water and heat fluxes

at point scale and runoff at catchment scale. In the text below, the findings from these chapters are briefly summarized.

Q1: *What is the adequate scheme of the roughness lengths for momentum and heat transfers to predict turbulent heat fluxes for the Tibetan alpine meadow?*

Two momentum roughness length schemes (z_{0m}) and three thermal roughness length schemes (z_{0h}) newly developed for the Noah LSM have been investigated in Chapter 4 to address this question. A linear method and a quadric method were utilized to derive the monthly z_{0m} from prescribed values for the fully vegetated and bare soil based on the monthly green vegetation fraction (*GVF*). Noah's original z_{0h} scheme was enhanced by modifying Zilitinkevich's empirical coefficient (C_{zil}) via correlating it with canopy height or z_{0m} (Chen and Zhang 2009), or calculating it based on the *GVF* (Zheng et al. 2012). Another alternative way was to use the z_{0h} scheme by Yang et al. (2008) specifically developed for the Tibetan Plateau (Chen et al. 2011).

Monthly variations of z_{0m} and diurnal variations of z_{0h} were derived through application of the Monin-Obukhov similarity theory based on the in-situ micro-meteorological measurements. These derived values together with the measured heat fluxes were utilized to assess the performance of the z_{0m} and z_{0h} schemes for three selected periods: a winter (15 December 2009 to 15 January 2010), a spring (8 April to 7 May 2010) and a monsoon period (1 to 30 September 2009). The analyses showed that the z_{0m} dynamics are related to vegetation dynamics and soil water freeze-thaw state, which are reproduced satisfactorily and comparably with the selected z_{0m} schemes. It was also demonstrated that the heat flux simulations are very sensitive to the diurnal variations of z_{0h} , and all the newly developed z_{0h} schemes capture the observed diurnal variability much better than the original one over the sparsely vegetated surfaces during the winter (frozen) period. However, only the z_{0h} schemes developed by Yang et al. (2008) and Chen and Zhang (2009) perform consistently better than the original one over the densely vegetated surfaces during the spring (thawed) and monsoon periods.

Using either of above two z_{0h} schemes, the Noah simulated sensible heat flux, latent heat flux and surface temperature can be improved by about 29, 79, and 75 % respectively. Since the suitability of the z_{0h} scheme proposed by Chen and Zhang (2009) had also been validated for a wide range of land cover and climate regimes using AmeriFlux data, it was recommended for global applications.

Q2: *How does the soil organic matter, thermal roughness length and vegetation canopy affect the turbulent and soil heat transport?*

This question has been addressed in Chapter 5 by performing Noah model runs with four augmentations to i) remove the vegetation muting on the heat conductivity (κ_h) for soil heat transport from the first layer towards the second layer, ii) calculate the exponential decay factor (β_{veg}) imposed on κ_h using the ratio of the leaf area index (*LAI*) over the green vegetation fraction (*GVF*), iii) correlate the Zilitinkevich's empirical coefficient (C_{zil}) for the turbulent heat transport with the momentum roughness length (z_{0m}) based on Chapter 4, and iv) consider the impact of organic matter in the parameterization of thermal heat properties. The modified soil thermal parameterization was then compared against laboratory measured soil heat conductivities, and five numerical experiments were designed to progressively assess the impact of each augmentation on Noah's performance in simulating turbulent and soil heat transport through comparison with turbulent heat flux and soil temperature profile measurements for the majority of the monsoon season (8 June to 30 September 2010).

The results showed that the default Noah LSM constrained by soil moisture profile measurements significantly overestimates the daytime turbulent heat fluxes, underestimates the surface temperature (T_{sfc}), and systematically underestimates the soil temperature profiles. The removal of the muting effect of vegetation on κ_h and the parameterization of β_{veg} greatly enhance the soil temperature profile simulations, whereas turbulent heat flux and surface temperature computations mostly benefit from the modified C_{zil} formulation. The Noah simulated sensible heat flux, latent heat flux, surface temperature and soil temperature at depths of 5, 25 and 70 cm can be improved by about 42, 44, 13, 55, 70, and 64 % with implementation of the four augmentations combined. Although usage of organic matter for calculating κ_h improves the correspondence between the estimates and laboratory measurements of heat conductivities, it was shown to have a relatively small impact on the Noah LSM performance even for large organic matter contents.

Three additional experiments were conducted to investigate the remaining issue associated with the overestimation of nighttime T_{sfc} . It was found that this problem should be treated from a coupled land-atmosphere perspective, and usage of different values for the daytime and nighttime β_{veg} provides a pragmatic solution to such a complex problem without changing the model structure. However, further study is preferred to develop a more formal approach with robust physics.

Q3: *What is the effect of the vertical soil heterogeneity on water and heat exchanges and how can this be included in the model structure of Noah LSM?*

The vertical soil heterogeneity caused by organic matter and root systems in the Tibetan alpine ecosystem has been studied using the Noah LSM in Chapter 6 by i) including the effect of organic matter on the soil hydraulic parameterization via the additivity hypothesis, ii) implementing the saturated hydraulic conductivity (K_s) as an exponentially decaying function with soil depth, iii) modifying the vertical root distribution to represent the Tibetan conditions characterized by an abundance of roots in the topsoil and iv) modifying the diffusivity form of Richards' equation to allow for the simulation of soil water flow across soil layers with different hydraulic properties. The modified soil hydraulic parameterization was compared against laboratory measurements, and three numerical experiments were designed to assess the impact of the augmentations on Noah's performance in simulating soil water flow for the majority of the monsoon season (8 June to 30 September 2010).

Usage of organic matter for calculating the porosity and soil suction improves the agreement between the estimates and laboratory measurements, and the exponential function together with the Kozeny-Carman equation best describes the in situ K_s across the soil profile. Through implementation of the modified hydraulic parameterization alone, the soil moisture underestimation in the upper soil layer under wet conditions is resolved, while the soil moisture profile dynamics are better captured when also the modified root water uptake function (i.e., asymptotic vertical root distribution) is included. As such, the Noah simulated soil moisture at depths of 5, 25 and 70 cm can be improved by about 49, 70 and 56 % with implementation of above augmentations.

The impact of the improved soil moisture simulations on the calculated surface energy and water budgets was further assessed. It was shown that Noah retains more water in the soil column with the augmentations causing a decrease in the other water balance components. On the other hand, the surface heat flux simulation is hardly affected, which was attributed to the fact that the latent heat flux in the selected study area and period is primarily constrained by the available energy rather than the available soil water. The monsoon episode was selected here due to the availability of continuous micro-meteorological measurements without a data gap as well as to avoid the impact of the cold season (e.g. snowpack and frozen soil) on the assessment of Noah's soil water flow and heat transport model physics.

Q4: *How does the model physics of vertical water and heat exchange processes impact the runoff production at catchment scale?*

The improved representation of the vertical water and heat exchange processes within the Noah LSM as presented in Chapters 4, 5 and 6 has been applied in Chapter 7 to further investigate its ability to reproducing runoff at catchment scale, e.g., the SRYR for the period of 2001-2010. Three sets of augmentations were implemented that enhance the Noah model physics associated with i) turbulent and soil heat transport (Noah-H, see Chapter 5), ii) soil water flow (Noah-W, see Chapter 6) and iii) frozen ground processes (Noah-F). Accordingly, five numerical experiments were designed; namely, a control run with the default model physics, three runs each with one of the selected augmentations and a run whereby all augmentations are implemented (Noah-A). All Noah model runs adopt their main soil and vegetation parameterizations from the Weather Research and Forecasting (WRF) model geographic input dataset, were driven by the 0.1° atmospheric forcing data from ITPCAS (Institute of Tibetan Plateau Research, Chinese Academy of Sciences) and were initialized using a single-year recurrent spin-up to achieve the equilibrium model states. In addition, the China Soil Database provides the organic matter content for the updated soil thermal and hydraulic parameterizations. In-situ heat flux, soil temperature (T_s) and moisture (θ) profile measurements were available for point-scale assessment, whereas monthly discharge data were utilized for the catchment-scale evaluation.

The comparison with point measurements showed that the augmentations invoked with Noah-H resolve issues with the heat flux overestimation and T_s underestimation produced by the default Noah model (consistent with Chapter 5), whereas Noah-W mitigates the default θ underestimation (consistent with Chapter 6). Noah-A yields improvements for both simulated surface energy and water budgets by including all selected augmentations, which improved the Noah simulated latent heat flux, T_s and θ at depths of 5 and 25 cm by about 15, 11, 44, 60, and 55 %, respectively.

The default Noah model is able to adequately capture the observed total runoff (R) dynamics at the catchment scale, but underestimates the magnitude of the monthly streamflow. Although the largest coefficient of determination (R^2) is obtained with Noah-H, large overestimations are generally found for the summer months. In contrast, Noah-W runoff yields the lowest R^2 that can be associated with the wrongly simulated discharge peak. The best model performance is also found for Noah-A with the combination of the augmentations leading to a baseflow dominated runoff regime, whereby the

surface runoff contribution remains significant. The error statistics are improved by about 24 % and 19 % in comparison to the default performance for mean error (ME) and root mean square error (RMSE) respectively.

Overall, this study has demonstrated that complete and robust descriptions of both surface water and energy budget processes in model physics are necessary for reliable prediction of water and heat exchanges at the land-atmosphere interface for a Tibetan alpine meadow ecosystem. Furthermore, a thorough understanding of the predominantly vertical water and heat exchange processes is preferred to correctly simulate the runoff at the catchment scale in the seasonally frozen and high altitude SRYR.

8.2 Recommendations for future work

The research presented in this thesis has shown that through comprehensive measurements performed in-situ and in the laboratory, significant improvements can be achieved in the water and heat flux simulations by a state-of-the-art LSM (i.e., Noah) and arrive at a better representation of the predominantly vertical water and heat exchange processes for a Tibetan alpine meadow ecosystem. Besides, the improved understanding of the predominantly vertical processes is also benefited for runoff simulation at the catchment scale, i.e., the SRYR. Additional work is, however, still needed to further investigate other important processes that are not thoroughly addressed in this thesis.

Further research should be carried out on robust parameterizations of cold season processes (i.e., freeze-thaw transitions). Su et al. (2013) have recently reported that current LSMs cannot adequately capture the freeze-thaw cycle due to their inherent difficulty in fully capturing both heat and mass exchanges under freeze-thaw conditions. Besides, a complete annual cycle of micro-meteorological observations is generally missing in the selected site of this thesis (i.e., Maqu station) as well as other sites on the Tibetan Plateau, and snowfall is also not measured, which makes the investigation of cold season processes more complex. More effort on collecting measurements during the cold season and validating the cold season processes becomes imperative as important sinks/sources of water and heat are associated with cold season processes that are expected to be impacted by climatic changes at high altitude regions.

Only monthly discharge measurements are available in this thesis for the catchment scale assessment of runoff production, which provide limited information on intra-monthly or daily runoff dynamics. It is therefore recommended to collect available daily discharge measurements and to include

groundwater flow and river routing in the LSM structures. The improved representation of the closed water cycle will provide further insight into the understanding of the runoff regime of Asian water towers that is of paramount importance to project the impact of climate variability on the regional hydrology and the water resources availability.

The SRYR in the northeastern part of the Tibetan Plateau is selected as the case study in this thesis, and additional work is also needed to extend the findings of this thesis to the whole Tibetan Plateau. The Weather Research and Forecasting (WRF) model geographic input dataset, the ITPCAS atmospheric forcing and the China Soil Database adopted in Chapter 7 can, for instance, be utilized for such an application. The data sets collected as part of the various field campaigns and monitoring networks setup on the Tibetan Plateau (e.g., Y. Ma et al. 2008; Su et al. 2011; Yang et al. 2013) may be used as the ‘ground truth’ to validate the model performance. Other alternative observational datasets could be various satellite products of relevant variables, such as precipitation, soil moisture, surface temperature and snow cover.

A comprehensive observational dataset including in-situ micro-meteorological and profile soil moisture/temperature measurements, laboratory soil property measurements of samples, as well as discharge measurements has been developed in this study, and Noah’s model physics have been thoroughly evaluated and improved by using this dataset. Although further effort is still needed to collect measurements for the cold season and to cover other representative land use/soil types of the Tibetan Plateau, this dataset could be treated as observational benchmark to investigate various LSMs for their ability in simulating water and heat exchanges in the Tibetan alpine meadow. For instance, using this dataset, the performance of the recently developed Noah-MP model (see Chapter 1, Niu et al. 2011) in simulating water and heat fluxes has been improved through enhancing the representation of under-canopy turbulence and root water uptake processes for a Tibetan alpine meadow ecosystem (Zheng et al. 2015).

Appendix

A.1 Estimation of momentum roughness length

Following the method in Yang et al. (2008), the logarithmic wind profile is rewritten as:

$$\ln z_{0m} = \ln z_h - \Psi_m(z_h / L) - ku / u_* \quad (\text{A1})$$

where z_{0m} is the roughness length for momentum transfer (m), z_h is the observation height of wind speed (m), Ψ_m is the stability correction function for momentum transfer (-), L is the Obukhov length (m), k is the von Karman constant (taken as 0.4), u is the mean wind speed (m s^{-1}), u_* is the friction velocity (m s^{-1}).

Using the 5-level profile and single level eddy-covariance (EC) measurements, a dataset of $\ln(z_{0m})$ is generated with multiple combinations of wind speed u and air temperature T_a (6-level), and the optimal values of z_{0m} for each month should correspond to the peak frequency in the histogram of $\ln(z_{0m})$.

Following the method in Sun (1999), eq. (A1) can be rewritten as:

$$u(z_h) = S_u Y_u(z_h) + I_u \quad (\text{A2})$$

$$Y_u(z_h) = \ln(z_h) - \Psi_m(z_h / L) \quad (\text{A3})$$

$$S_u = u_* / k \quad (\text{A4})$$

$$I_u = -\frac{u_*}{k} \ln(z_{0m}) \quad (\text{A5})$$

Similarly, using both the profile and EC observations, $Y_u(z_h)$ can be estimated at the corresponding wind observation levels (6-level). Applying the linear least-square regression method for the 6-level $u(z_h)$ versus $Y_u(z_h)$, the z_{0m} can be estimated from the regression slope S_u and the intercept I_u (eqs. (A4)-(A5)) as:

$$\ln(z_{0m}) = -I_u / S_u \quad (\text{A6})$$

Using the method of Sun (1999), $\ln(z_{0m})$ is calculated for each time interval of observations (30 min), and the peak frequency histogram is used to determine the optimal values of z_{0m} for each month.

A.2 Stability functions

The stability functions of Łobocki (1993) for stable conditions are (Chen et al. 1997):

$$\Psi_m = \zeta / R_{FC} - 2.076 \left[1 - 1 / (\zeta + 1) \right] \quad 0 \leq \zeta < 1 \quad (\text{A7})$$

$$\Psi_h = \zeta R_{ic} / \left(R_{FC}^2 \phi_T(0) \right) - 2.076 \left[1 - \exp(-1.2\zeta) \right] \quad 0 \leq \zeta < 1 \quad (\text{A8})$$

$$\zeta = z_h / L \quad (\text{A9})$$

where Ψ_m and Ψ_h are the stability correction functions for momentum and sensible heat transfer respectively (-), z_h is the observation height (m), L is the Obukhov length (m), R_{ic} is the critical gradient Richardson number (taken as 0.183), R_{FC} is the critical flux Richardson number (taken as 0.191), and $\phi_T(0)$ is the dimensionless velocity gradient for neutral conditions (taken as 0.8).

The stability function of Holtslag and De Bruin (1988) for stable conditions is:

$$-\Psi_m = -\Psi_h = a\zeta + b(\zeta - c/d)\exp(-d\zeta) + bc/d \quad (\text{A10})$$

where $a = 0.7$, $b = 0.75$, $c = 5$ and $d = 0.35$.

A.3 Soil pedotransfer functions

The soil pedotransfer function (PTF) approach has been widely used to predict hydraulic parameters (e.g., porosity, saturated hydraulic conductivity) from more easily measured soil data, such as texture and organic matter content. The PTFs can be subdivided into class and continuous PTFs: the class PTF predicts the average hydraulic characteristics based on distinct soil texture classes, while the continuous PTF uses actually measured soil particle-size distribution data (e.g., percentages sand and clay) to calculate these hydraulic parameters.

The average hydraulic characteristics of silt loam, sandy loam and peat are summarized in table A1, and are derived from the class PTF as given by Cosby et al. (1984) and Letts et al. (2000). The continuous PTF proposed by Cosby et al. (1984) is described as follows:

$$\theta_s = 0.489 - 0.00126 \cdot \text{sand} \quad (\text{A11})$$

$$K_s = 7.0556 \times 10^{-6.884 + 0.0153 \cdot \text{sand}} \quad (\text{A12})$$

$$\psi_s = -0.01 \times 10^{1.88 - 0.0131 \cdot \text{sand}} \quad (\text{A13})$$

$$b = 2.91 + 0.159 \cdot \text{clay} \quad (\text{A14})$$

where θ_s is the porosity ($\text{m}^3 \text{m}^{-3}$), K_s is the saturated hydraulic conductivity (m s^{-1}), ψ_s is the soil water potential at air-entry (m), b is an empirical parameter (-), *sand* is the percentage of sand in the soil particle (%), *clay* is the percentage of clay (%).

Table A1: Average soil hydraulic characteristics predicted by class pedotransfer function (PTF)

Class	$\theta_s (\text{m}^3 \text{m}^{-3})$	$K_s (10^{-6} \text{m s}^{-1})$	$\psi_s (\text{m})$	$b (-)$	Reference
Silt Loam	0.476	2.81	-0.759	5.33	Cosby et al.
Sandy Loam	0.434	5.23	-0.141	4.74	(1984)
Fibric Peat	0.93	280	-0.0103	2.7	Letts et al.
Hemic Peat	0.88	2.0	-0.0102	6.1	(2000)
Sapric Peat	0.83	0.10	-0.0101	12.0	

List of symbols

Greek

Symbol	Name	Units
α	Shape parameter of the gamma distribution of soil ice	-
β	Empirical parameter of the asymptotic root function	-
β_{veg}	Empirical parameter of the exponential decay of canopy	-
Δ	Slope of saturated vapor pressure curve	kPa K ⁻¹
ε	Surface emissivity	-
θ	Total soil water content	m ³ m ⁻³
θ_a	Potential air temperature	K
θ_c	Critical soil water content below which transpiration is reduced due to water stress	m ³ m ⁻³
θ_{ice}	Soil ice content	m ³ m ⁻³
θ_{liq}	Liquid soil water content	m ³ m ⁻³
θ_s	Soil porosity	m ³ m ⁻³
θ_{sfc}	Potential surface temperature	K
$\theta_{s,min}$	Soil porosity of mineral soil	m ³ m ⁻³
$\theta_{s,soc}$	Soil porosity of organic soil	m ³ m ⁻³
θ_w	Soil water content at wilting point	m ³ m ⁻³
θ_{33}	Soil water content at -33 kPa matric potential	m ³ m ⁻³
θ_*	Friction temperature	K
κ_{dry}	Thermal heat conductivity of dry soil	W m ⁻¹ K ⁻¹
κ_h	Thermal heat conductivity	W m ⁻¹ K ⁻¹
κ_o	Thermal heat conductivity of other soil particles	W m ⁻¹ K ⁻¹
κ_{qtz}	Thermal heat conductivity of quartz	W m ⁻¹ K ⁻¹
κ_{sat}	Thermal heat conductivity of saturated soil	W m ⁻¹ K ⁻¹
κ_{soc}	Thermal heat conductivity of organic soil	W m ⁻¹ K ⁻¹
κ_{soil}	Thermal heat conductivity of solid soil particles	W m ⁻¹ K ⁻¹
κ_w	Thermal heat conductivity of water	W m ⁻¹ K ⁻¹
λ	Latent heat of vaporization	J kg ⁻¹

List of symbols

ν	Kinematic molecular viscosity	$\text{m}^2 \text{s}^{-1}$
ρ	Density of air	kg m^{-3}
ρ_b	Bulk density of soil matrix	kg m^{-3}
$\rho_{b,min}$	Bulk density of mineral soil matrix	kg m^{-3}
$\rho_{b,soc}$	Bulk density of organic soil matrix	kg m^{-3}
ρ_{ice}	Density of ice	kg m^{-3}
ρ_s	Particle density of solid soil particles	kg m^{-3}
$\rho_{s,min}$	Particle density of mineral soil particles	kg m^{-3}
$\rho_{s,soc}$	Particle density of organic soil particles	kg m^{-3}
σ	Stefan-Boltzmann constant	$\text{W m}^{-2} \text{K}^4$
ψ	Soil water potential	m
ψ_a	Soil water potential at the interface of two layers	m
Ψ_h	Stability function for sensible heat transfer	-
Ψ_m	Stability function for momentum transfer	-
ψ_s	Saturated water potential of soil matrix	m
$\psi_{s,min}$	Saturated water potential of mineral soil matrix	m
$\psi_{s,soc}$	Saturated water potential of organic soil matrix	m

Roman

Symbol	Name	Units
b	Shape parameter of the pore-size distribution of soil matrix	-
b_{min}	Shape parameter of the pore-size distribution of mineral soil matrix	-
b_{soc}	Shape parameter of the pore-size distribution of organic soil matrix	-
C_{air}	Thermal heat capacity of air	$\text{J m}^{-3} \text{K}^{-1}$
C_e	Empirical constant of the Kozeny-Carman equation	mm h^{-1}
C_h	Surface exchange coefficient for heat transfer	-
C_m	Surface exchange coefficient for momentum transfer	-
C_{min}	Thermal heat capacity of mineral soil particles	$\text{J m}^{-3} \text{K}^{-1}$
c_p	Specific heat of air	$\text{J kg}^{-1} \text{K}^{-1}$
C_s	Thermal heat capacity	$\text{J m}^{-3} \text{K}^{-1}$
C_{soil}	Thermal heat capacity of solid soil particles	$\text{J m}^{-3} \text{K}^{-1}$
C_{soc}	Thermal heat capacity of organic soil particles	$\text{J m}^{-3} \text{K}^{-1}$
C_w	Thermal heat capacity of water	$\text{J m}^{-3} \text{K}^{-1}$
C_{zil}	Zilitinkevich's empirical coefficient	-
$clay$	Percentage of clay in the soil particle	%
D	Soil water diffusivity	$\text{m}^2 \text{s}^{-1}$
D_s	Soil water diffusivity under saturated water condition	$\text{m}^2 \text{s}^{-1}$
E_c	Evaporation of precipitation intercepted by the canopy	m
E_s	Soil evaporation	m
E_t	Transpiration via canopy and roots	m
ET_a	Actual evapotranspiration	m
ET_p	Potential evapotranspiration	m
f	Exponential profile decay factor for hydraulic conductivity and runoff production	m^{-1}
f_{imp}	Impermeable frozen area under frozen ground condition	-
$f_{root,i}$	Root fractions for the i th soil layer	-
$f_{sw,i}$	Soil water stress for the i th soil layer	-

List of symbols

$f_{s,soc}$	Volumetric fraction of organic soil particles used for thermal parameterization	-
$f_{t,soc}$	Volumetric fraction of organic soil matrix used for hydraulic parameterization	-
g	Gravity acceleration	$m\ s^{-2}$
G_0	Ground surface heat flux	$W\ m^{-2}$
$G_{0,bs}$	Surface heat flux under bare soil condition	$W\ m^{-2}$
GVF	Green vegetation fraction	-
H	Sensible heat flux	$W\ m^{-2}$
h_c	Canopy height	m
I_{max}	Infiltration capacity of soil column	$m\ s^{-1}$
k	von Karman constant	-
K	Hydraulic conductivity	$m\ s^{-1}$
K_{dt}	Empirical constant for estimation of infiltration capacity	day^{-1}
K_e	Kersten (1949) number	-
K_s	Saturated hydraulic conductivity	$m\ s^{-1}$
L	Obukhov length	m
L_f	Latent heat of fusion	$J\ kg^{-1}$
L^\downarrow	Downward longwave radiation	$W\ m^{-2}$
L^\uparrow	Upward longwave radiation	$W\ m^{-2}$
LAI	Leaf area index	$m^2\ m^{-2}$
LE	Latent heat flux	$W\ m^{-2}$
LE_p	Potential evapotranspiration	$W\ m^{-2}$
m_{soc}	Organic carbon mass content	$kg\ kg^{-1}$
$NDVI$	Normalized difference vegetation index	-
$nroot$	Total number of root layers	-
P	Total precipitation	m
P_x	Effective precipitation arriving at the ground	m
q	Specific humidity	$kg\ kg^{-1}$
q_s	Saturated specific humidity	$kg\ kg^{-1}$
R	Total runoff	m
R_b	Drainage or base flow	m
$r_{e,i}$	Effective root fraction for the i th soil layer	-

RH	Relative humidity	kg kg^{-1}
R_n	Net radiation	W m^{-2}
R_s	Surface runoff	m
S^\downarrow	Downward shortwave radiation	W m^{-2}
S^\uparrow	Upward shortwave radiation	W m^{-2}
$sand$	Percentage of sand in the soil particle	%
t	Time	s
T_a	Air temperature	K
T_s	Soil column temperature	K
T_{sfc}	Ground surface temperature	K
u	Wind speed	m s^{-1}
u_*	Friction velocity	m s^{-1}
V_t	Total volume of soil matrix	m^3
$V_{t,min}$	Soil volume occupied by mineral matrix	m^3
$V_{t,soc}$	Soil volume occupied by organic matrix	m^3
W	Total water storage	m
W_c	Canopy intercepted water	m
W_{cr}	Critical ice content above which the frozen ground is impermeable	m
W_d	Total soil moisture deficit in the soil column	m
W_{ice}	Soil ice storage	m
W_s	Soil water storage	m
Y	Cumulative root fraction	-
z	Soil depth	m
z_h	Observation height of air temperature and/or wind speed	m
z_{0h}	Roughness length for heat transfer	m
z_{0m}	Roughness length for momentum transfer	m
z_{0v}	Momentum roughness length for fully vegetative area	m
z_{0g}	Momentum roughness length for bare ground	m

List of abbreviations

AGCMs	Atmospheric General Circulation Models
AVHRR	Advanced Very High Resolution Radiometer
CEOP	Coordinated Enhanced Observing Period
CAMP-Tibet	CEOP Asia-Australia Monsoon Project in Tibet
CLM	Community Land Model
CMA	China Meteorological Administration
ECMWF	European Centre for Medium-Range Weather Forecasts
EC system	Eddy-covariance system
FAO	Food and Agriculture Organization of the United Nations
GEWEX	Global Energy and Water cycle Experiment
GAME-Tibet	GEWEX Asian Monsoon Experiment-Tibet
GEWEX-SRB	GEWEX/Surface Radiation Budget
GLDAS	Global Land Data Assimilation Systems
HRLDAS	High Resolution Land Data Assimilation System
ITPCAS	Institute of Tibetan Plateau Research/Chinese Academy of Sciences
LDAS	Land Data Assimilation Systems
LSMs	Land Surface Models
MODIS	Moderate Resolution Imaging Spectroradiometer
MOST	Monin-Obukhov Similarity Theory
NASA	National Aeronautics and Space Administration
NCAR	National Center for Atmospheric Research
NCEP	National Centers for Environmental Prediction
NLDAS	North American Land Data Assimilation System
OSU	Oregon State University
PBL	Planetary Boundary Layer
PTF	Pedotransfer function
SMST	Soil moisture and soil temperature monitoring network
SPOT	Satellite Pour l'Observation de la Terre
SRYP	Source Region of the Yellow River

STATSGO	Soils data for the Conterminous United States Derived from the NRCS State Soil Geographic
SVAT	Soil-vegetation-atmosphere transfer schemes
Tibet-Obs	Tibetan Plateau Observatory
TORP	Tibetan Observation and Research Platform
TRMM	Tropical Rainfall Measuring Mission
VIC	Variable Infiltration Capacity model
WRF	Weather Research and Forecasting model
YRCC	Yellow River Conservancy Commission

Bibliography

- Ahuja, L. R., J. W. Naney, R. E. Green, and D. R. Nielsen, 1984: Macroporosity to Characterize Spatial Variability of Hydraulic Conductivity and Effects of Land Management. *Soil Sci. Soc. Am. J.*, **48**, 699-702.
- Balsamo, G., F. Pappenberger, E. Dutra, P. Viterbo, and B. van den Hurk, 2011: A revised land hydrology in the ECMWF model: a step towards daily water flux prediction in a fully-closed water cycle. *Hydrological Processes*, **25**, 1046-1054.
- Balsamo, G., A. Beljaars, K. Scipal, P. Viterbo, B. van den Hurk, M. Hirschi, and A. K. Betts, 2009: A Revised Hydrology for the ECMWF Model: Verification from Field Site to Terrestrial Water Storage and Impact in the Integrated Forecast System. *Journal of Hydrometeorology*, **10**, 623-643.
- Barlage, M., and Coauthors, 2010: Noah land surface model modifications to improve snowpack prediction in the Colorado Rocky Mountains. *Journal of Geophysical Research: Atmospheres*, **115**, D22101.
- Bastiaanssen, W. G. M., M. Menenti, R. A. Feddes, and A. A. M. Holtslag, 1998: A remote sensing surface energy balance algorithm for land (SEBAL). 1. Formulation. *J Hydrol*, **212–213**, 198-212.
- Beljaars, A. C. M., and A. A. M. Holtslag, 1991: Flux Parameterization over Land Surfaces for Atmospheric Models. *Journal of Applied Meteorology*, **30**, 327-341.
- Beringer, J., A. H. Lynch, F. S. Chapin, M. Mack, and G. B. Bonan, 2001: The Representation of Arctic Soils in the Land Surface Model: The Importance of Mosses. *Journal of Climate*, **14**, 3324-3335.
- Best, M. J., 1998: A Model to Predict Surface Temperatures. *Boundary-Layer Meteorology*, **88**, 279-306.
- Beven, K., 1982: On subsurface stormflow: an analysis of response times. *Hydrological Sciences Journal*, **27**, 505-521.
- Beven, K. J., and H. L. Cloke, 2012: Comment on “Hyperresolution global land surface modeling: Meeting a grand challenge for monitoring Earth's terrestrial water” by Eric F. Wood et al. *Water Resources Research*, **48**, W01801.
- Braun, F. J., and G. Schädler, 2005: Comparison of Soil Hydraulic Parameterizations for Mesoscale Meteorological Models. *Journal of Applied Meteorology*, **44**, 1116-1132.

- Brutsaert, W. H., 1982: *Evaporation into the Atmosphere: Theory, History and Applications*. Springer, 316 pp.
- , 1998: Land-surface water vapor and sensible heat flux: Spatial variability, homogeneity, and measurement scales. *Water Resour Res*, **34**, 2433-2442.
- Cai, X., Z.-L. Yang, C. H. David, G.-Y. Niu, and M. Rodell, 2014: Hydrological evaluation of the Noah-MP land surface model for the Mississippi River Basin. *Journal of Geophysical Research: Atmospheres*, **119**, 2013JD020792.
- Campbell, G. S., 1974: A simple method for determining unsaturated conductivity from moisture retention data. *Soil Science*, **117**, 311-314.
- Carey, S. K., W. L. Quinton, and N. T. Goeller, 2007: Field and laboratory estimates of pore size properties and hydraulic characteristics for subarctic organic soils. *Hydrological Processes*, **21**, 2560-2571.
- Chen, F., and Y. Zhang, 2009: On the coupling strength between the land surface and the atmosphere: From viewpoint of surface exchange coefficients. *Geophysical Research Letters*, **36**, L10404.
- Chen, F., Z. Janjić, and K. Mitchell, 1997: Impact of Atmospheric Surface-layer Parameterizations in the new Land-surface Scheme of the NCEP Mesoscale Eta Model. *Boundary-Layer Meteorology*, **85**, 391-421.
- Chen, F., and Coauthors, 1996: Modeling of land surface evaporation by four schemes and comparison with FIFE observations. *Journal of Geophysical Research: Atmospheres*, **101**, 7251-7268.
- Chen, J., and P. Kumar, 2001: Topographic Influence on the Seasonal and Interannual Variation of Water and Energy Balance of Basins in North America. *Journal of Climate*, **14**, 1989-2014.
- Chen, X., Z. Su, Y. Ma, K. Yang, J. Wen, and Y. Zhang, 2013: An Improvement of Roughness Height Parameterization of the Surface Energy Balance System (SEBS) over the Tibetan Plateau. *Journal of Applied Meteorology and Climatology*, **52**, 607-622.
- Chen, Y., K. Yang, D. Zhou, J. Qin, and X. Guo, 2010: Improving the Noah Land Surface Model in Arid Regions with an Appropriate Parameterization of the Thermal Roughness Length. *Journal of Hydrometeorology*, **11**, 995-1006.
- Chen, Y., K. Yang, W. Tang, J. Qin, and L. Zhao, 2012: Parameterizing soil organic carbon's impacts on soil porosity and thermal parameters for Eastern Tibet grasslands. *Science China Earth Sciences*, **55**, 1001-1011.
- Chen, Y., K. Yang, J. Qin, L. Zhao, W. Tang, and M. Han, 2013: Evaluation of AMSR-E retrievals and GLDAS simulations against observations of a soil

- moisture network on the central Tibetan Plateau. *Journal of Geophysical Research: Atmospheres*, **118**, 4466-4475.
- Chen, Y., K. Yang, J. He, J. Qin, J. Shi, J. Du, and Q. He, 2011: Improving land surface temperature modeling for dry land of China. *Journal of Geophysical Research: Atmospheres*, **116**, D20104.
- Cherkauer, K. A., and D. P. Lettenmaier, 1999: Hydrologic effects of frozen soils in the upper Mississippi River basin. *Journal of Geophysical Research: Atmospheres*, **104**, 19599-19610.
- Cherkauer, K. A., L. C. Bowling, and D. P. Lettenmaier, 2003: Variable infiltration capacity cold land process model updates. *Global and Planetary Change*, **38**, 151-159.
- Clapp, R. B., and G. M. Hornberger, 1978: Empirical equations for some soil hydraulic properties. *Water Resources Research*, **14**, 601-604.
- Clark, D. B., and Coauthors, 2011: The Joint UK Land Environment Simulator (JULES), model description – Part 2: Carbon fluxes and vegetation dynamics. *Geosci. Model Dev.*, **4**, 701-722.
- Clark, M. P., and Coauthors, 2015: A unified approach for process-based hydrologic modeling: 2. Model implementation and case studies. *Water Resources Research*, **51**, 2515-2542.
- Cosby, B. J., G. M. Hornberger, R. B. Clapp, and T. R. Ginn, 1984: A Statistical Exploration of the Relationships of Soil Moisture Characteristics to the Physical Properties of Soils. *Water Resources Research*, **20**, 682-690.
- Cuo, L., Y. Zhang, Y. Gao, Z. Hao, and L. Cairang, 2013: The impacts of climate change and land cover/use transition on the hydrology in the upper Yellow River Basin, China. *Journal of Hydrology*, **502**, 37-52.
- Dai, Y., and Coauthors, 2003: The Common Land Model. *Bulletin of the American Meteorological Society*, **84**, 1013-1023.
- Dankers, R., E. J. Burke, and J. Price, 2011: Simulation of permafrost and seasonal thaw depth in the JULES land surface scheme. *The Cryosphere*, **5**, 773-790.
- de Rosnay, P., M. Bruen, and J. Polcher, 2000: Sensitivity of surface fluxes to the number of layers in the soil model used in GCMs. *Geophysical Research Letters*, **27**, 3329-3332.
- de Vries, D. A., 1963: Thermal properties of soils. *Physics of plant environment*, W. R. van WIJK, Ed., 210-235.
- Decharme, B., 2007: Influence of runoff parameterization on continental hydrology: Comparison between the Noah and the ISBA land surface models. *Journal of Geophysical Research: Atmospheres*, **112**, D19108.

- Decharme, B., A. Boone, C. Delire, and J. Noilhan, 2011: Local evaluation of the Interaction between Soil Biosphere Atmosphere soil multilayer diffusion scheme using four pedotransfer functions. *Journal of Geophysical Research: Atmospheres*, **116**, D20126.
- Decharme, B., H. Douville, A. Boone, F. Habets, and J. Noilhan, 2006: Impact of an Exponential Profile of Saturated Hydraulic Conductivity within the ISBA LSM: Simulations over the Rhône Basin. *Journal of Hydrometeorology*, **7**, 61-80.
- Decker, M., M. A. Brunke, Z. Wang, K. Sakaguchi, X. Zeng, and M. G. Bosilovich, 2011: Evaluation of the Reanalysis Products from GSFC, NCEP, and ECMWF Using Flux Tower Observations. *Journal of Climate*, **25**, 1916-1944.
- Dente, L., Z. Vekerdy, J. Wen, and Z. Su, 2012: Maqu network for validation of satellite-derived soil moisture products. *International Journal of Applied Earth Observation and Geoinformation*, **17**, 55-65.
- Dirmeyer, P. A., X. Gao, M. Zhao, Z. Guo, T. Oki, and N. Hanasaki, 2006: GSWP-2: Multimodel Analysis and Implications for Our Perception of the Land Surface. *Bulletin of the American Meteorological Society*, **87**, 1381-1397.
- Ek, M., and L. Mahrt: OSU 1-D PBL model user's guide. [Available online at <http://ftp.emc.ncep.noaa.gov/mmb/gcp/ldas/nceplsm/OSU1DPBL/OSU1D-PBL-userguide.pdf>.]
- Ek, M. B., and Coauthors, 2003: Implementation of Noah land surface model advances in the National Centers for Environmental Prediction operational mesoscale Eta model. *Journal of Geophysical Research: Atmospheres*, **108**, 8851.
- Famiglietti, J. S., and E. F. Wood, 1994: Multiscale modeling of spatially variable water and energy balance processes. *Water Resources Research*, **30**, 3061-3078.
- Fan, Y., G. Miguez-Macho, C. P. Weaver, R. Walko, and A. Robock, 2007: Incorporating water table dynamics in climate modeling: 1. Water table observations and equilibrium water table simulations. *Journal of Geophysical Research: Atmospheres*, **112**, D10125.
- Farouki, O. T., 1986: *Thermal properties of soils*. Vol. 11, Trans. Tech. Publ., 136 pp.
- Feddes, R. A., P. J. Kowalik, and H. Zaradny, 1978: *Simulation of Field Water Use and Crop Yield*. Wiley.

- Federer, C. A., D. E. Turcotte, and C. T. Smith, 1993: The organic fraction–bulk density relationship and the expression of nutrient content in forest soils. *Canadian Journal of Forest Research*, **23**, 1026-1032.
- Finney, D. L., E. Blyth, and R. Ellis, 2012: Improved modelling of Siberian river flow through the use of an alternative frozen soil hydrology scheme in a land surface model. *The Cryosphere*, **6**, 859-870.
- Foken, T., 2008: THE ENERGY BALANCE CLOSURE PROBLEM: AN OVERVIEW. *Ecol Appl*, **18**, 1351-1367.
- Gale, M. R., and D. F. Grigal, 1987: Vertical root distributions of northern tree species in relation to successional status. *Canadian Journal of Forest Research*, **17**, 829-834.
- Gao, H., X. He, B. Ye, and J. Pu, 2012: Modeling the runoff and glacier mass balance in a small watershed on the Central Tibetan Plateau, China, from 1955 to 2008. *Hydrological Processes*, **26**, 1593-1603.
- Garratt, J. R., 1994: *The Atmospheric Boundary Layer*. Cambridge University Press, 336 pp.
- Gayler, S., and Coauthors, 2014: Incorporating dynamic root growth enhances the performance of Noah-MP at two contrasting winter wheat field sites. *Water Resources Research*, **50**, 1337-1356.
- Godfrey, C. M., and D. J. Stensrud, 2008: Soil Temperature and Moisture Errors in Operational Eta Model Analyses. *Journal of Hydrometeorology*, **9**, 367-387.
- Gouttevin, I., G. Krinner, P. Ciais, J. Polcher, and C. Legout, 2012: Multi-scale validation of a new soil freezing scheme for a land-surface model with physically-based hydrology. *The Cryosphere*, **6**, 407-430.
- Gulden, L. E., and Coauthors, 2007: Improving land-surface model hydrology: Is an explicit aquifer model better than a deeper soil profile? *Geophysical Research Letters*, **34**, L09402.
- Guo, D., and H. Wang, 2013: Simulation of permafrost and seasonally frozen ground conditions on the Tibetan Plateau, 1981–2010. *Journal of Geophysical Research: Atmospheres*, **118**, 5216-5230.
- Gutman, G., and A. Ignatov, 1998: The derivation of the green vegetation fraction from NOAA/AVHRR data for use in numerical weather prediction models. *Int J Remote Sens*, **19**, 1533-1543.
- Hills, R. G., I. Porro, D. B. Hudson, and P. J. Wierenga, 1989: Modeling one-dimensional infiltration into very dry soils: 1. Model development and evaluation. *Water Resources Research*, **25**, 1259-1269.

- Holtslag, A. A. M., and H. A. R. De Bruin, 1988: Applied Modeling of the Nighttime Surface Energy Balance over Land. *Journal of Applied Meteorology*, **27**, 689-704.
- Hong, S., V. Lakshmi, E. E. Small, F. Chen, M. Tewari, and K. W. Manning, 2009: Effects of vegetation and soil moisture on the simulated land surface processes from the coupled WRF/Noah model. *Journal of Geophysical Research: Atmospheres*, **114**, D18118.
- Hu, Y., S. Maskey, and S. Uhlenbrook, 2012: Trends in temperature and rainfall extremes in the Yellow River source region, China. *Climatic Change*, **110**, 403-429.
- Hu, Y., S. Maskey, S. Uhlenbrook, and H. Zhao, 2011: Streamflow trends and climate linkages in the source region of the Yellow River, China. *Hydrological Processes*, **25**, 3399-3411.
- Huffman, G. J., and Coauthors, 2007: The TRMM Multisatellite Precipitation Analysis (TMPA): Quasi-Global, Multiyear, Combined-Sensor Precipitation Estimates at Fine Scales. *Journal of Hydrometeorology*, **8**, 38-55.
- Immerzeel, W. W., L. P. H. van Beek, and M. F. P. Bierkens, 2010: Climate Change Will Affect the Asian Water Towers. *Science*, **328**, 1382-1385.
- Jackson, R. B., J. Canadell, J. R. Ehleringer, H. A. Mooney, O. E. Sala, and E. D. Schulze, 1996: A global analysis of root distributions for terrestrial biomes. *Oecologia*, **108**, 389-411.
- Jiang, X., G.-Y. Niu, and Z.-L. Yang, 2009: Impacts of vegetation and groundwater dynamics on warm season precipitation over the Central United States. *J Geophys Res*, **114**, D06109.
- Jiménez, C., and Coauthors, 2014: Freshwater resources. *Climate Change 2014: Impacts, Adaptation, and Vulnerability. Part A: Global and Sectoral Aspects. Contribution of Working Group II to the Fifth Assessment Report of the Intergovernmental Panel of Climate Change*, C. B. Field, and Coauthors, Eds., Cambridge University Press, 229-269.
- Jiménez, C., and Coauthors, 2011: Global intercomparison of 12 land surface heat flux estimates. *Journal of Geophysical Research: Atmospheres*, **116**, D02102.
- Jin, H., R. He, G. Cheng, Q. Wu, S. Wang, L. Lü, and X. Chang, 2009: Changes in frozen ground in the Source Area of the Yellow River on the Qinghai-Tibet Plateau, China, and their eco-environmental impacts. *Environmental Research Letters*, **4**, 045206.

- Johansen, O., 1975: Thermal conductivity of soils. PhD, University of Trondheim, 236 pp.
- Kersten, M. S., 1949: Thermal properties of soils. Bulletin 28, 227 pp.
- Kohsiek, W., C. Liebenthal, T. Foken, R. Vogt, S. P. Oncley, C. Bernhofer, and H. A. R. Debruin, 2007: The Energy Balance Experiment EBEX-2000. Part III: Behaviour and quality of the radiation measurements. *Boundary-Layer Meteorol*, **123**, 55-75.
- Koike, T., 2004: The Coordinated Enhanced Observing Period-an initial step for integrated global water cycle observation. *WMO Bulletin*, **53**, 115-121.
- Koike, T., T. Yasunari, J. Wang, and T. Yao, 1999: GAME-Tibet IOP Summary Report. *Proceedings of the 1st International Workshop on GAME-Tibet*, 1-2.
- Koren, V., J. Schaake, K. Mitchell, Q. Y. Duan, F. Chen, and J. M. Baker, 1999: A parameterization of snowpack and frozen ground intended for NCEP weather and climate models. *Journal of Geophysical Research: Atmospheres*, **104**, 19569-19585.
- Koster, R. D., and Coauthors, 2010: Contribution of land surface initialization to subseasonal forecast skill: First results from a multi-model experiment. *Geophysical Research Letters*, **37**, n/a-n/a.
- Koster, R. D., and Coauthors, 2004: Regions of Strong Coupling Between Soil Moisture and Precipitation. *Science*, **305**, 1138-1140.
- Koster, R. D., and Coauthors, 2006: GLACE: The Global Land–Atmosphere Coupling Experiment. Part I: Overview. *Journal of Hydrometeorology*, **7**, 590-610.
- Lawrence, D. M., and A. G. Slater, 2008: Incorporating organic soil into a global climate model. *Climate Dynamics*, **30**, 145-160.
- Leng, G., M. Huang, Q. Tang, H. Gao, and L. R. Leung, 2013: Modeling the Effects of Groundwater-Fed Irrigation on Terrestrial Hydrology over the Conterminous United States. *Journal of Hydrometeorology*, **15**, 957-972.
- Letts, M. G., N. T. Roulet, N. T. Comer, M. R. Skarupa, and D. L. Versegny, 2000: Parametrization of peatland hydraulic properties for the Canadian land surface scheme. *Atmosphere-Ocean*, **38**, 141-160.
- Li, H., and Coauthors, 2011: Evaluating runoff simulations from the Community Land Model 4.0 using observations from flux towers and a mountainous watershed. *Journal of Geophysical Research: Atmospheres*, **116**, D24120.

- Li, K. Y., R. De Jong, and J. B. Boisvert, 2001: An exponential root-water-uptake model with water stress compensation. *Journal of Hydrology*, **252**, 189-204.
- Li, Q., S. Sun, and Y. Xue, 2010: Analyses and development of a hierarchy of frozen soil models for cold region study. *Journal of Geophysical Research: Atmospheres*, **115**, D03107.
- Liang, X., E. F. Wood, and D. P. Lettenmaier, 1996: Surface soil moisture parameterization of the VIC-2L model: Evaluation and modification. *Global and Planetary Change*, **13**, 195-206.
- , 1999: Modeling ground heat flux in land surface parameterization schemes. *Journal of Geophysical Research: Atmospheres*, **104**, 9581-9600.
- Lim, Y.-J., J. Hong, and T.-Y. Lee, 2012: Spin-up behavior of soil moisture content over East Asia in a land surface model. *Meteorol Atmos Phys*, **118**, 151-161.
- Livneh, B., P. J. Restrepo, and D. P. Lettenmaier, 2011: Development of a Unified Land Model for Prediction of Surface Hydrology and Land–Atmosphere Interactions. *Journal of Hydrometeorology*, **12**, 1299-1320.
- Livneh, B., Y. Xia, K. E. Mitchell, M. B. Ek, and D. P. Lettenmaier, 2010: Noah LSM Snow Model Diagnostics and Enhancements. *Journal of Hydrometeorology*, **11**, 721-738.
- Lobocki, L., 1993: A Procedure for the Derivation of Surface-Layer Bulk Relationships from Simplified Second-Order Closure Models. *Journal of Applied Meteorology*, **32**, 126-138.
- Luo, L., and Coauthors, 2003: Effects of Frozen Soil on Soil Temperature, Spring Infiltration, and Runoff: Results from the PILPS 2(d) Experiment at Valdai, Russia. *Journal of Hydrometeorology*, **4**, 334-351.
- Lutz, A. F., W. W. Immerzeel, A. B. Shrestha, and M. F. P. Bierkens, 2014: Consistent increase in High Asia's runoff due to increasing glacier melt and precipitation. *Nature Clim. Change*, **4**, 587-592.
- Mölder, M., and A. Lindroth, 1999: Thermal roughness length of a boreal forest. *Agricultural and Forest Meteorology*, **98–99**, 659-670.
- Ma, Y., M. Menenti, R. Feddes, and J. Wang, 2008: Analysis of the land surface heterogeneity and its impact on atmospheric variables and the aerodynamic and thermodynamic roughness lengths. *J Geophys Res*, **113**, D08113.
- Ma, Y., O. Tsukamoto, J. Wang, H. Ishikawa, and I. Tamagawa, 2002: Analysis of aerodynamic and thermodynamic parameters on the grassy marshland surface of Tibetan Plateau. *Prog Nat Sci*, **12**, 36-40.

- Ma, Y., S. Kang, L. Zhu, B. Xu, L. Tian, and T. Yao, 2008: ROOF OF THE WORLD: Tibetan Observation and Research Platform. *Bulletin of the American Meteorological Society*, **89**, 1487-1492.
- Ma, Y., and Coauthors, 2009: Recent advances on the study of atmosphere-land interaction observations on the Tibetan Plateau. *Hydrol. Earth Syst. Sci.*, **13**, 1103-1111.
- Mahanama, S. P. P., R. D. Koster, R. H. Reichle, and M. J. Suarez, 2008: Impact of Subsurface Temperature Variability on Surface Air Temperature Variability: An AGCM Study. *Journal of Hydrometeorology*, **9**, 804-815.
- Mahrt, L., and M. Ek, 1984: The Influence of Atmospheric Stability on Potential Evaporation. *Journal of Climate and Applied Meteorology*, **23**, 222-234.
- Mahrt, L., and H. Pan, 1984: A two-layer model of soil hydrology. *Boundary-Layer Meteorology*, **29**, 1-20.
- Manabe, S., 1969: Climate and the Ocean Circulation. *Monthly Weather Review*, **97**, 739-774.
- Martano, P., 2000: Estimation of Surface Roughness Length and Displacement Height from Single-Level Sonic Anemometer Data. *J Appl Meteorol*, **39**, 708-715.
- Massman, W. J., and X. Lee, 2002: Eddy covariance flux corrections and uncertainties in long-term studies of carbon and energy exchanges. *Agr Forest Meteorol*, **113**, 121-144.
- Maxwell, R. M., and N. L. Miller, 2005: Development of a Coupled Land Surface and Groundwater Model. *Journal of Hydrometeorology*, **6**, 233-247.
- Mitchell, K. E., and Coauthors, 2004: The multi-institution North American Land Data Assimilation System (NLDAS): Utilizing multiple GCIP products and partners in a continental distributed hydrological modeling system. *Journal of Geophysical Research: Atmospheres*, **109**, D07S90.
- Nemes, A., W. J. Rawls, and Y. A. Pachepsky, 2005: Influence of Organic Matter on the Estimation of Saturated Hydraulic Conductivity. *Soil Sci. Soc. Am. J.*, **69**, 1330-1337.
- Niu, G.-Y., and Z.-L. Yang, 2006: Effects of Frozen Soil on Snowmelt Runoff and Soil Water Storage at a Continental Scale. *Journal of Hydrometeorology*, **7**, 937-952.
- Niu, G.-Y., and Coauthors, 2011: The community Noah land surface model with multiparameterization options (Noah-MP): 1. Model description and

- evaluation with local-scale measurements. *Journal of Geophysical Research: Atmospheres*, **116**, D12109.
- Oleson, K., and Coauthors, 2013: *Technical description of version 4.5 of the Community Land Model (CLM)*. NCAR Technical Note NCAR/TN-503+STR.
- Pan, H. L., and L. Mahrt, 1987: Interaction between soil hydrology and boundary-layer development. *Boundary-Layer Meteorology*, **38**, 185-202.
- Paulson, C. A., 1970: The Mathematical Representation of Wind Speed and Temperature Profiles in the Unstable Atmospheric Surface Layer. *Journal of Applied Meteorology*, **9**, 857-861.
- Peters-Lidard, C. D., M. S. Zion, and E. F. Wood, 1997: A soil-vegetation-atmosphere transfer scheme for modeling spatially variable water and energy balance processes. *Journal of Geophysical Research: Atmospheres*, **102**, 4303-4324.
- Peters-Lidard, C. D., E. Blackburn, X. Liang, and E. F. Wood, 1998: The Effect of Soil Thermal Conductivity Parameterization on Surface Energy Fluxes and Temperatures. *Journal of the Atmospheric Sciences*, **55**, 1209-1224.
- Philipona, R., and Coauthors, 2001: Atmospheric longwave irradiance uncertainty: Pyrgeometers compared to an absolute sky-scanning radiometer, atmospheric emitted radiance interferometer, and radiative transfer model calculations. *Journal of Geophysical Research: Atmospheres*, **106**, 28129-28141.
- Piao, S., and Coauthors, 2012: Impacts of climate and CO₂ changes on the vegetation growth and carbon balance of Qinghai–Tibetan grasslands over the past five decades. *Global and Planetary Change*, **98–99**, 73-80.
- Pitman, A. J., A. G. Slater, C. E. Desborough, and M. Zhao, 1999: Uncertainty in the simulation of runoff due to the parameterization of frozen soil moisture using the Global Soil Wetness Project methodology. *Journal of Geophysical Research: Atmospheres*, **104**, 16879-16888.
- Rinke, A., P. Kuhry, and K. Dethloff, 2008: Importance of a soil organic layer for Arctic climate: A sensitivity study with an Arctic RCM. *Geophysical Research Letters*, **35**, L13709.
- Rodell, M., and Coauthors, 2004: The Global Land Data Assimilation System. *Bulletin of the American Meteorological Society*, **85**, 381-394.
- Rosero, E., Z.-L. Yang, T. Wagener, L. E. Gulden, S. Yatheendradas, and G.-Y. Niu, 2010: Quantifying parameter sensitivity, interaction, and transferability in hydrologically enhanced versions of the Noah land

- surface model over transition zones during the warm season. *Journal of Geophysical Research: Atmospheres*, **115**, D03106.
- Salama, M. S., R. Van der Velde, L. Zhong, Y. Ma, M. Ofwono, and Z. Su, 2012: Decadal variations of land surface temperature anomalies observed over the Tibetan Plateau by the Special Sensor Microwave Imager (SSM/I) from 1987 to 2008. *Climatic Change*, **114**, 769-781.
- Sato, T., and F. Kimura, 2007: How Does the Tibetan Plateau Affect the Transition of Indian Monsoon Rainfall? *Monthly Weather Review*, **135**, 2006-2015.
- Sato, Y., X. Ma, J. Xu, M. Matsuoka, H. Zheng, C. Liu, and Y. Fukushima, 2008: Analysis of long-term water balance in the source area of the Yellow River basin. *Hydrological Processes*, **22**, 1618-1629.
- Saxton, K. E., and W. J. Rawls, 2006: Soil Water Characteristic Estimates by Texture and Organic Matter for Hydrologic Solutions. *Soil Sci. Soc. Am. J.*, **70**, 1569-1578.
- Schaake, J. C., V. I. Koren, Q.-Y. Duan, K. Mitchell, and F. Chen, 1996: Simple water balance model for estimating runoff at different spatial and temporal scales. *Journal of Geophysical Research: Atmospheres*, **101**, 7461-7475.
- Schaudt, K. J., 1998: A New Method for Estimating Roughness Parameters and Evaluating the Quality of Observations. *J Appl Meteorol*, **37**, 470-476.
- Sellers, P. J., Y. Mintz, Y. C. Sud, and A. Dalcher, 1986: A Simple Biosphere Model (SIB) for Use within General Circulation Models. *Journal of the Atmospheric Sciences*, **43**, 505-531.
- Sellers, P. J., and Coauthors, 1997: Modeling the Exchanges of Energy, Water, and Carbon Between Continents and the Atmosphere. *Science*, **275**, 502-509.
- Seneviratne, S. I., D. Luthi, M. Litschi, and C. Schar, 2006: Land-atmosphere coupling and climate change in Europe. *Nature*, **443**, 205-209.
- Shangguan, W., Y. Dai, B. Liu, A. Ye, and H. Yuan, 2012: A soil particle-size distribution dataset for regional land and climate modelling in China. *Geoderma*, **171-172**, 85-91.
- Shangguan, W., Y. Dai, Q. Duan, B. Liu, and H. Yuan, 2014: A global soil data set for earth system modeling. *Journal of Advances in Modeling Earth Systems*, **6**, 249-263.
- Shangguan, W., and Coauthors, 2013: A China data set of soil properties for land surface modeling. *Journal of Advances in Modeling Earth Systems*, **5**, 212-224.

- Shao, Y., and P. Irannejad, 1999: On the Choice of Soil Hydraulic Models in Land-Surface Schemes. *Boundary-Layer Meteorology*, **90**, 83-115.
- Shrestha, R., and P. Houser, 2010: A heterogeneous land surface model initialization study. *Journal of Geophysical Research: Atmospheres*, **115**, D19111.
- Slater, A. G., T. J. Bohn, J. L. McCreight, M. C. Serreze, and D. P. Lettenmaier, 2007: A multimodel simulation of pan-Arctic hydrology. *Journal of Geophysical Research: Biogeosciences*, **112**, G04S45.
- Stieglitz, M., D. Rind, J. Famiglietti, and C. Rosenzweig, 1997: An Efficient Approach to Modeling the Topographic Control of Surface Hydrology for Regional and Global Climate Modeling. *Journal of Climate*, **10**, 118-137.
- Su, Z., 2002: The surface energy balance system (SEBS) for estimation of turbulent heat fluxes. *Hydrol Earth Syst Sc*, **6**, 85-99.
- Su, Z., T. Schmugge, W. P. Kustas, and W. J. Massman, 2001: An Evaluation of Two Models for Estimation of the Roughness Height for Heat Transfer between the Land Surface and the Atmosphere. *J Appl Meteorol*, **40**, 1933-1951.
- Su, Z., P. de Rosnay, J. Wen, L. Wang, and Y. Zeng, 2013: Evaluation of ECMWF's soil moisture analyses using observations on the Tibetan Plateau. *Journal of Geophysical Research: Atmospheres*, **118**, 5304-5318.
- Su, Z., and Coauthors, 2011: The Tibetan Plateau observatory of plateau scale soil moisture and soil temperature (Tibet-Obs) for quantifying uncertainties in coarse resolution satellite and model products. *Hydrol. Earth Syst. Sci.*, **15**, 2303-2316.
- Sun, J., 1999: Diurnal Variations of Thermal Roughness Height over a Grassland. *Bound-Layer Meteor*, **92**, 407-427.
- Sun, J., and L. Mahrt, 1995: Determination of Surface Fluxes from the Surface Radiative Temperature. *Journal of the Atmospheric Sciences*, **52**, 1096-1106.
- Tanaka, K., I. Tamagawa, H. Ishikawa, Y. Ma, and Z. Hu, 2003: Surface energy budget and closure of the eastern Tibetan Plateau during the GAME-Tibet IOP 1998. *J Hydrol*, **283**, 169-183.
- Taylor, K. E., 2001: Summarizing multiple aspects of model performance in a single diagram. *Journal of Geophysical Research: Atmospheres*, **106**, 7183-7192.
- Twine, T. E., and Coauthors, 2000: Correcting eddy-covariance flux underestimates over a grassland. *Agr Forest Meteorol*, **103**, 279-300.

- van der Velde, R., Z. Su, M. Ek, M. Rodell, and Y. Ma, 2009: Influence of thermodynamic soil and vegetation parameterizations on the simulation of soil temperature states and surface fluxes by the Noah LSM over a Tibetan plateau site. *Hydrol. Earth Syst. Sci.*, **13**, 759-777.
- van der Velde, R., M. S. Salama, T. Pellarin, M. Ofwono, Y. Ma, and Z. Su, 2014: Long term soil moisture mapping over the Tibetan plateau using Special Sensor Microwave/Imager. *Hydrol. Earth Syst. Sci.*, **18**, 1323-1337.
- Verhoef, A., H. A. R. DeBruin, and B. J. J. M. v. d. Hurk, 1997: Some practical notes on the parameter kB-1 for sparse canopies. *J Appl Meteorol*, **36**, 560-572.
- Viterbo, P., A. Beljaars, J.-F. Mahfouf, and J. Teixeira, 1999: The representation of soil moisture freezing and its impact on the stable boundary layer. *Quarterly Journal of the Royal Meteorological Society*, **125**, 2401-2426.
- Vrugt, J. A., M. T. van Wijk, J. W. Hopmans, and J. Šimunek, 2001: One-, two-, and three-dimensional root water uptake functions for transient modeling. *Water Resources Research*, **37**, 2457-2470.
- Wang, G., H. Hu, and T. Li, 2009: The influence of freeze–thaw cycles of active soil layer on surface runoff in a permafrost watershed. *Journal of Hydrology*, **375**, 438-449.
- Wang, G., G. Liu, and C. Li, 2012: Effects of changes in alpine grassland vegetation cover on hillslope hydrological processes in a permafrost watershed. *Journal of Hydrology*, **444–445**, 22-33.
- Wang, S., and Y. Ma, 2011: Characteristics of Land–Atmosphere Interaction Parameters over the Tibetan Plateau. *J Hydrometeorol*, **12**, 702-708.
- Wang, Z., X. Zeng, and M. Decker, 2010: Improving snow processes in the Noah land model. *Journal of Geophysical Research: Atmospheres*, **115**, D20108.
- Wiernga, J., 1993: Representative roughness parameters for homogeneous terrain. *Bound-Layer Meteorol*, **63**, 323-363.
- Wilson, K., and Coauthors, 2002: Energy balance closure at FLUXNET sites. *Agr Forest Meteorol*, **113**, 223-243.
- Wood, E. F., and Coauthors, 2011: Hyperresolution global land surface modeling: Meeting a grand challenge for monitoring Earth's terrestrial water. *Water Resources Research*, **47**, W05301.
- Wu, G., and Y. Zhang, 1998: Tibetan Plateau Forcing and the Timing of the Monsoon Onset over South Asia and the South China Sea. *Monthly Weather Review*, **126**, 913-927.

- Wu, G., Y. Liu, B. He, Q. Bao, A. Duan, and F.-F. Jin, 2012: Thermal Controls on the Asian Summer Monsoon. *Sci. Rep.*, **2**.
- Wu, Q., and T. Zhang, 2010: Changes in active layer thickness over the Qinghai-Tibetan Plateau from 1995 to 2007. *Journal of Geophysical Research: Atmospheres*, **115**, D09107.
- Wu, T., L. Zhao, R. Li, Q. Wang, C. Xie, and Q. Pang, 2013: Recent ground surface warming and its effects on permafrost on the central Qinghai-Tibet Plateau. *International Journal of Climatology*, **33**, 920-930.
- Xia, Y., and Coauthors, 2014: Evaluation of multi-model simulated soil moisture in NLDAS-2. *Journal of Hydrology*, **512**, 107-125.
- Xia, Y., and Coauthors, 2012a: Validation of Noah-Simulated Soil Temperature in the North American Land Data Assimilation System Phase 2. *Journal of Applied Meteorology and Climatology*, **52**, 455-471.
- Xia, Y., and Coauthors, 2012b: Continental-scale water and energy flux analysis and validation for North American Land Data Assimilation System project phase 2 (NLDAS-2): 2. Validation of model-simulated streamflow. *Journal of Geophysical Research: Atmospheres*, **117**, D03110.
- Xia, Y., and Coauthors, 2012c: Continental-scale water and energy flux analysis and validation for the North American Land Data Assimilation System project phase 2 (NLDAS-2): 1. Intercomparison and application of model products. *Journal of Geophysical Research: Atmospheres*, **117**, D03109.
- Xu, X., and Coauthors, 2008: A New Integrated Observational System Over the Tibetan Plateau. *Bull Amer Meteor Soc*, **89**, 1492-1496.
- Xue, B.-L., and Coauthors, 2013: Modeling the land surface water and energy cycles of a mesoscale watershed in the central Tibetan Plateau during summer with a distributed hydrological model. *Journal of Geophysical Research: Atmospheres*, **118**, 8857-8868.
- Yang, D., and Coauthors, 2004: Analysis of water resources variability in the Yellow River of China during the last half century using historical data. *Water Resources Research*, **40**, W06502.
- Yang, K., T. Koike, and D. Yang, 2003: Surface Flux Parameterization in the Tibetan Plateau. *Bound-Layer Meteor*, **106**, 245-262.
- Yang, K., Y. Y. Chen, and J. Qin, 2009: Some practical notes on the land surface modeling in the Tibetan Plateau. *Hydrol. Earth Syst. Sci.*, **13**, 687-701.
- Yang, K., T. Koike, H. Ishikawa, and Y. Ma, 2004: Analysis of the Surface Energy Budget at a Site of GAME/Tibet using a Single-Source Model. *Journal of the Meteorological Society of Japan. Ser. II*, **82**, 131-153.

- Yang, K., T. Koike, B. Ye, and L. Bastidas, 2005: Inverse analysis of the role of soil vertical heterogeneity in controlling surface soil state and energy partition. *Journal of Geophysical Research: Atmospheres*, **110**, D08101.
- Yang, K., J. He, W. Tang, J. Qin, and C. C. K. Cheng, 2010: On downward shortwave and longwave radiations over high altitude regions: Observation and modeling in the Tibetan Plateau. *Agricultural and Forest Meteorology*, **150**, 38-46.
- Yang, K., H. Wu, J. Qin, C. Lin, W. Tang, and Y. Chen, 2014: Recent climate changes over the Tibetan Plateau and their impacts on energy and water cycle: A review. *Global and Planetary Change*, **112**, 79-91.
- Yang, K., and Coauthors, 2008: Turbulent Flux Transfer over Bare-Soil Surfaces: Characteristics and Parameterization. *Journal of Applied Meteorology and Climatology*, **47**, 276-290.
- Yang, K., and Coauthors, 2013: A Multiscale Soil Moisture and Freeze–Thaw Monitoring Network on the Third Pole. *Bulletin of the American Meteorological Society*, **94**, 1907-1916.
- Yang, Y., J. Fang, C. Ji, and W. Han, 2009a: Above- and belowground biomass allocation in Tibetan grasslands. *Journal of Vegetation Science*, **20**, 177-184.
- Yang, Y., and Coauthors, 2009b: Changes in topsoil carbon stock in the Tibetan grasslands between the 1980s and 2004. *Global Change Biology*, **15**, 2723-2729.
- Yao, T., and Coauthors, 2012: Different glacier status with atmospheric circulations in Tibetan Plateau and surroundings. *Nature Clim. Change*, **2**, 663-667.
- Zeiliguer, A. M., Y. A. Pachepsky, and W. J. Rawls, 2000: Estimating Water Retention of Sandy Soils Using the Additivity Hypothesis. *Soil Science*, **165**, 373-383.
- Zeng, X., 2001: Global Vegetation Root Distribution for Land Modeling. *Journal of Hydrometeorology*, **2**, 525-530.
- Zeng, X., Z. Wang, and A. Wang, 2012: Surface Skin Temperature and the Interplay between Sensible and Ground Heat Fluxes over Arid Regions. *Journal of Hydrometeorology*, **13**, 1359-1370.
- Zhang, L., F. Su, D. Yang, Z. Hao, and K. Tong, 2013: Discharge regime and simulation for the upstream of major rivers over Tibetan Plateau. *Journal of Geophysical Research: Atmospheres*, **118**, 8500-8518.
- Zhang, Y., S. K. Carey, and W. L. Quinton, 2008: Evaluation of the algorithms and parameterizations for ground thawing and freezing simulation in

- permafrost regions. *Journal of Geophysical Research: Atmospheres*, **113**, D17116.
- Zhang, Y., S. K. Carey, W. L. Quinton, J. R. Janowicz, J. W. Pomeroy, and G. N. Flerchinger, 2010: Comparison of algorithms and parameterisations for infiltration into organic-covered permafrost soils. *Hydrol. Earth Syst. Sci.*, **14**, 729-750.
- Zhang, Y., and Coauthors, 2013: Coupling of a simultaneous heat and water model with a distributed hydrological model and evaluation of the combined model in a cold region watershed. *Hydrological Processes*, **27**, 3762-3776.
- Zheng, D., R. van der Velde, Z. Su, M. J. Booij, A. Y. Hoekstra, and J. Wen, 2014: Assessment of Roughness Length Schemes Implemented within the Noah Land Surface Model for High-Altitude Regions. *Journal of Hydrometeorology*, **15**, 921-937.
- Zheng, D., R. van der Velde, Z. Su, J. Wen, M. J. Booij, A. Y. Hoekstra, and X. Wang, 2015: Under-canopy turbulence and root water uptake of a Tibetan meadow ecosystem modeled by Noah-MP. *Water Resource Research*, **51**, doi:10.1002/2015WR017115.
- Zheng, H., L. Zhang, C. Liu, Q. Shao, and Y. Fukushima, 2007: Changes in stream flow regime in headwater catchments of the Yellow River basin since the 1950s. *Hydrological Processes*, **21**, 886-893.
- Zheng, W., and Coauthors, 2012: Improvement of daytime land surface skin temperature over arid regions in the NCEP GFS model and its impact on satellite data assimilation. *Journal of Geophysical Research: Atmospheres*, **117**, D06117.
- Zhou, D., and R. Huang, 2012: Response of water budget to recent climatic changes in the source region of the Yellow River. *Chin. Sci. Bull.*, **57**, 2155-2162.
- Zhou, X., P. Zhao, J. Chen, L. Chen, and W. Li, 2009: Impacts of thermodynamic processes over the Tibetan Plateau on the Northern Hemispheric climate. *Sci. China Ser. D-Earth Sci.*, **52**, 1679-1693.
- Zilitinkevich, S. S., 1995: Non-local turbulent transport: Pollution dispersion aspects of coherent structure of convective flows. *Air Pollution Theory and Simulation*, H. Power, N. Moussiopoulos, and C. A. Brebbia, Eds., Computational Mechanics Publications, 53-60.

UNIVERSITY OF TWENTE.

Understanding the water and heat exchanges across the Tibetan ecosystem is of great importance for management of the Asian water towers that originate from the Tibetan Plateau and projection of water and energy dynamics within various climate scenarios. The study presented in this book contributes to a better quantification of the water and heat exchanges at the land-atmosphere interface for a Tibetan alpine meadow ecosystem.

The source region of the Yellow River (SRYR) in the northeastern part of the Tibetan Plateau is selected as the case study due to its great importance to the Yellow River's water resources. A comprehensive observational dataset including in-situ micro-meteorological and profile soil moisture/temperature measurements, laboratory soil property measurements of

samples, as well as discharge measurements is developed. The Noah land surface model is utilized to understand the processes governing the water and heat exchanges and predict the measurements.

This book is structured across four research topics to arrive at a reliable prediction of the measured water and heat fluxes at point scale and runoff at catchment scale via enhancing Noah's model physics in representing i) thermal roughness length and turbulent heat transfer, ii) soil heat transport, iii) soil water flow and iv) frozen ground processes. This study highlights the need for a complete description of the predominantly vertical water and heat exchange processes to correctly simulate the water and heat fluxes in the seasonally frozen and high altitude SRYR on the Tibetan Plateau.

ISBN: 978-90-365-3988-3
DOI-number: 10.3990/1.9789036539883
URL: <http://dx.doi.org/10.3990/1.9789036539883>



9 789036 539883 >